4. SITE 950[1]

Shipboard Scientific Party[2]

HOLE 950A

Date occupied: 5 August 1994

Date departed: 10 August 1994

Time on hole: 5 days, 3 hr, 30 min

Position: 31°9.011′N, 25°36.004′W

Bottom felt (drill-pipe measurement from rig floor, m): 5448.6

Distance between rig floor and sea level (m): 10.80

Water depth (drill-pipe measurement from sea level, m): 5437.8

Total depth (from rig floor, m): 5829.90

Penetration (m): 381.30

Number of cores (including cores having no recovery): 41

Total length of cored section (m): 381.30

Total core recovered (m): 339.14

Core recovery (%): 88.9

Oldest sediment cored:
Depth (mbsf): 381.30
Nature: volcanic sandstone
Earliest age: middle Eocene

Principal results: Site 950 is located in the western Madeira Abyssal Plain at 31°9.01′N, 25°36.00′W, at a water depth of 5437.8 m in the Cruiser Fracture Zone Valley. Seismic profiles for the area show two major units: an upper unit showing relatively high amplitude parallel reflectors that onlap onto basement highs, and a lower unit that partly onlaps and partly drapes the basement highs. The upper unit can be subdivided into three subunits by relatively strong reflectors at 180 ms and 240 ms. Reflectors within the lower two subunits are weaker than in the upper subunit. This seismic pattern is typical for the whole abyssal plain (Searle, 1987) and is interpreted as pelagic drape over basement, with the deeper draped sequences being later infilled by rapidly accumulated turbidites. The primary objective of this site was to determine the nature of the turbidite fill and distinguish discrete sources for the various compositional groups of sediment flows. When combined with information from the other two sites, and the extensive seismic coverage on the abyssal plain, this data will facilitate estimations of the volumes of sediment eroded and redeposited within the Canary Basin. Secondary objectives include estimation of the volumes and timing of volcaniclastic sediment flows from the Canaries, and monitoring the history of the CCD in one of the deepest areas drilled in the North Atlantic.

A single hole was drilled at Site 950 and a total of 17 APC cores (0–154.4 mbsf) and 24 extended core barrel (XCB) cores (154.4–381.3 mbsf) were retrieved with average recovery rates of 100.5% and 81.1%, respectively. The hole was logged with the seismic stratigraphy, lithoporosity, geochemical, and Formation MicroScanner tools.

The sedimentary sequence at Site 950 comprises four lithologic units.

Unit I (0–305.6 mbsf): consists of Pleistocene to middle Miocene (0–13.6 Ma), thick clayey nannofossil mixed sediment and nannofossil clay turbidites, interbedded with pelagic nannofossil oozes, mixed sediments and clays. Below 150 mbsf the pelagic interbeds are all clays. There are three primary types of turbidites: volcaniclastic from the volcanic islands within the basin, organic-rich from the northwestern African margin, and calcareous from seamounts to the west of the plain. All three types are found throughout Unit I. The volcaniclastic and organic-rich turbidites are fine grained and only occasionally have silty bases, indicating their distal nature. Such flows are unlikely to erode the underlying sediments. Some of the calcareous turbidites have bases consisting of foraminiferal sand, but even these show few signs of having eroded the underlying beds. A remarkable feature is the regular but infrequent deposition of the turbidites, with a few centimeters to decimeters of pelagic sediment between successive flows. Only rarely do two turbidites lie adjacent to each other.

Unit II (305.6–333 mbsf): consists of massive calcarenite of middle Miocene age (approximately 13.6–15 Ma). Core recovery in this interval was poor, but the logging data clearly shows three calcarenite units with turbidites between them. The calcarenite consists of coarse shallow-water carbonate clasts with shallow water benthic foraminifers, including *Amphistegina,* and some mafic and felsic glass shards. The composition of this unit strongly suggests it was derived from local sources such as the Cruiser/Hyères/Great Meteor seamount complex to the west.

Unit III (333–370 mbsf): consists of dominantly red pelagic clays with thin interbeds of clayey nannofossil mixed sediment and zeolitized volcanic ash bands. Nannofossils from within the turbidites suggest this unit ranges in age from middle Miocene to middle Eocene (15–47 Ma). It is underlain by lithologic Unit IV.

Unit IV (370–381 mbsf): consists of two depositional units of dark volcaniclastic siltstone and sandstone separated by clay. The volcanic ash bands and volcaniclastic flows are all interpreted to have been derived from the Cruiser/Hyères/Great Meteor seamount complex.

Paleomagnetic stratigraphy gave usable datum levels from the Brunhes (Cln) to within the Gauss (C2An) based on measurements in the pelagic interbeds between turbidites. Planktonic foraminifers also provided useful biostratigraphic data from the pelagic interbeds in the upper part of the hole (0–140 mbsf), below which they were only preserved in the bases of calcareous turbidites. Nannofossils, however, were found consistently in pelagic interbeds from 0–200 mbsf (0–5.8 Ma) and intermittently to 273 mbsf (11.5 Ma). Below this, stratigraphy is based on first occurrence (FO) data from turbidites and also deduced from extrapolation of the accumulation rates of the pelagic units.

The major change in the accumulation rate of the pelagic interbeds from 1.5 m/m.y. to 5.6 m/m.y. occurs at 2.6 Ma, coinciding with the change from clays to alternating clays, marls, and oozes. This is also coincident with the onset of major Northern Hemisphere glaciation and associated deepening of the CCD that placed this site above the CCD. The overall sediment accumulation rate for lithologic Unit I, which is dominated by the deposition of turbidites, averages 42 m/m.y. from 0 to 3 Ma, 28 m/m.y. from 3 to 6.5 Ma, and 21 m/m.y. between 11 and 13.6 Ma. The interval from 6.5–11 Ma appears to have a lower accumulation rate of 9 m/

[1]Schmincke, H.-U., Weaver, P.P.E., Firth, J.V., et al., 1995. *Proc. ODP, Init. Repts.,* 157: College Station, TX (Ocean Drilling Program).
[2]Shipboard Scientific Party is given in the list preceding the Table of Contents.

m.y. The lower part of the hole, dominated by red clay deposition (lithologic Unit III), has a very low accumulation rate of 1 m/m.y.

Carbonate, organic carbon, and sulfur data from both pelagic sediments and turbidites display significant stratigraphic variation that facilitates the subdivision of the sequence. Organic-rich turbidites containing up to 2% C_{org} occur throughout the sequence but contain less carbonate and higher sulfur in the lowest beds, reflecting both environmental changes in their source area and a longer diagenetic history. Carbon/nitrogen ratios indicate that marine organic matter dominates in most beds.

An excellent suite of pore-water geochemical results were obtained from Site 950. Sulfate and ammonia data demonstrate that sulfate reduction is occurring principally in the deeper parts of the sequence below 130 mbsf. No evidence of methanogenesis is recorded in the sequence. Calcium and magnesium results suggest that precipitation of carbonate is occurring above and within the sulfate-reducing zone. Silica, potassium, and other pore-water data demonstrate that biogenic silica is being dissolved in the upper parts of the sequence, while diagenesis in the deeper section is related to clay mineral and zeolite formation.

A total of four Schlumberger tool strings were run at Hole 950A: the seismic stratigraphy, lithoporosity, geochemical, and Formation MicroScanner tool combinations. The coverage of the hole with all tool strings was good and the data quality appear high with some excellent correlation to physical property measurements of core. The thick sequence of interbedded turbidites are well defined by the geochemical logs, which respond to the varying clay and carbonate composition. The transition lower in the hole to a more clay-rich carbonate-poor sequence is well characterized by the chemical logs and correlates to biostratigraphic data that indicates decrease in the rate of sediment deposition. Beneath this unit, in an area of poor recovery, the physical and chemical logs clearly delineate the presence of three calcarenite units, the thickest of which is 10.5 m, of which only 1.1 m in total was recovered in the cores. MST velocities measured in the laboratory closely followed the same trends as those estimated by logging, but they were approximately 100 m/s lower.

A combination of the downhole sonic log data with the MST-velocities measured on the APC-cores (0–150 m) provided a complete velocity profile down to 340 mbsf. Based on this, a two-way traveltime–depth relation was established that will enable a precise correlation between seismic profiles and lithological/stratigraphical observations in the cores. The base of seismic Unit A correlates with the surface of the red clay sequence at about 330 mbsf. The internal subunits in Unit A probably mainly reflect large scale changes in turbidite thickness and lithology. In Unit B the upper parallel reflectors seem to represent the red clay and the chaotic interval below seems to image the turbidites encountered in the cores below 370 mbsf.

The excellent core recovery and downhole logs from this site will facilitate later correlations to the other two sites on the plain and to the wide seismic coverage across the whole plain. Although the biostratigraphy was poor in the deeper parts of the hole owing to preservation problems, enough datum levels were established to interpret the sequence. Preliminary results show that major turbidite deposition from the northwestern African margin and Canary Islands began about 15 Ma with an increase in the volume of sediment eroded at about 3 Ma. The Cruiser/Hyères/Great Meteor seamount chain appears to have been volcanically active from at least 47 Ma to 15 Ma.

BACKGROUND AND OBJECTIVES

Site 950 is the first of three sites drilled in the Madeira Abyssal Plain to determine the history of sediment transport within the Canary Basin. Seismic profiles show the abyssal plain to consist of about 350 m of acoustically laminated sediments overlying a drape of about 200 m of expected hemipelagic clay (Searle, 1987; also see "Introduction," this volume). The acoustically laminated sediments are believed to consist predominantly of turbidites and have a total volume of about 20,000 km^3. This amount of sediment has been transported from the northwestern African continental margin, Canary Islands, Madeira, and other now-extinct volcanoes in the basin.

Piston-core data has shown that the larger turbidites form layers over the whole basin while smaller flows are limited to the northeastern, southwestern, or southern part of the plain. Hence the location of one drill site in each of these areas so that localized flows can be distinguished from larger basin-wide flows. High resolution stratigraphy has shown that 12 of the 18 isotope stage boundaries in the last 730,000 yr are represented by one turbidite only, while two of the stage boundaries encompass turbidites from two different sources (Weaver et al., 1992). There are also a small number of turbidites within individual isotope stages. Thus Weaver and Kuijpers (1983) postulated a correlation between sediment instability and sea-level change. These three sites will show how far back in time this apparent correlation continues and whether there are long-term changes in the stability of continental margins.

A determination of the ages of each mass flow, and hence their frequency from each source, together with an estimate of the volume of each flow, will provide an extremely detailed history of mass sediment wasting within this basin. The volumes will be determined by correlating individual flows between the three sites and extrapolating their thicknesses to the margins of the plain using the seismic profiles as a guide.

An examination of the composition and ages of volcaniclastic flows may shed light on the intervals in volcanic island evolution, particularly when they are unstable and most susceptible to mass wasting. The frequency of flows from the northwestern African margin will determine the history of stability of this margin, and the high resolution stratigraphy we plan to produce will shed light on correlations between continental margin stability and sea-level change over longer periods of time than previous piston core studies. In the deeper parts of the sequence a series of volcaniclastic turbidites are expected from the Cruiser-Meteor Seamount complex and will indicate when these seamounts were active volcanoes.

Site 950 has been chosen in an area where all the seismic reflector units are well developed. The site also lies in a fracture zone valley which, throughout its history, has had a connection through to the continental rise to the east (Fig. 1). Thus, we believe turbidity current flow has never been obstructed, which would allow the base of each seismic unit to be dated at its oldest point (particularly important where units may onlap onto basement highs). This site, therefore, provides the best opportunity to ascertain the relationship of turbidite input to sea-level change and Canary Island development. Site 950 is located 25 km west-southwest of the site of a 34-m-long giant piston core, MD10, which contains a complete turbidite sequence through the last 690 k.y. (isotope Stages 1 to 17) including turbidites *a* to *u* (Weaver et al., 1992).

At Site 950 we drilled beyond the turbidite unit into the underlying pelagic drape, so as to characterize this lower seismic unit and determine whether it contains volcanic ash layers related to earlier volcanic activity in the area or even thin turbidites related to early mass wasting events.

UNDERWAY GEOPHYSICS

On the approach to Site 950 a seismic profile about 17 km long was acquired from 31°05′N, 25°44′W, to 31°10′N, 25°34′W. The profile was shot with an 80 in.^{3} water gun and the data were recorded by a single channel streamer and displayed on line-scan printers. The data were stored digitally on 8 mm tape and were processed with the SIOSEIS software. The processing sequence was bandpass filter (60–120 Hz), automatic gain control (500 ms window), trace mix (weights 121), mute, and display. The processed profile is shown in Figure 2.

The profile shows the relatively steep flank of a topographic high at the edge of the basin. The sediments in the basin are penetrated and

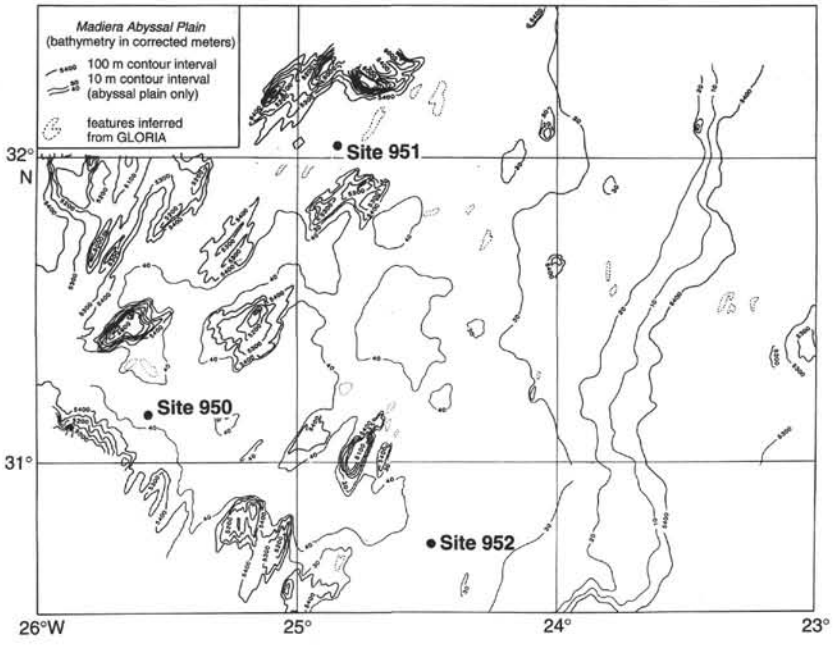

Figure 1. Bathymetric map of the Madeira Abyssal Plain based on numerous precision depth recorder (PDR) records and interpretation of GLORIA sidescan sonar.

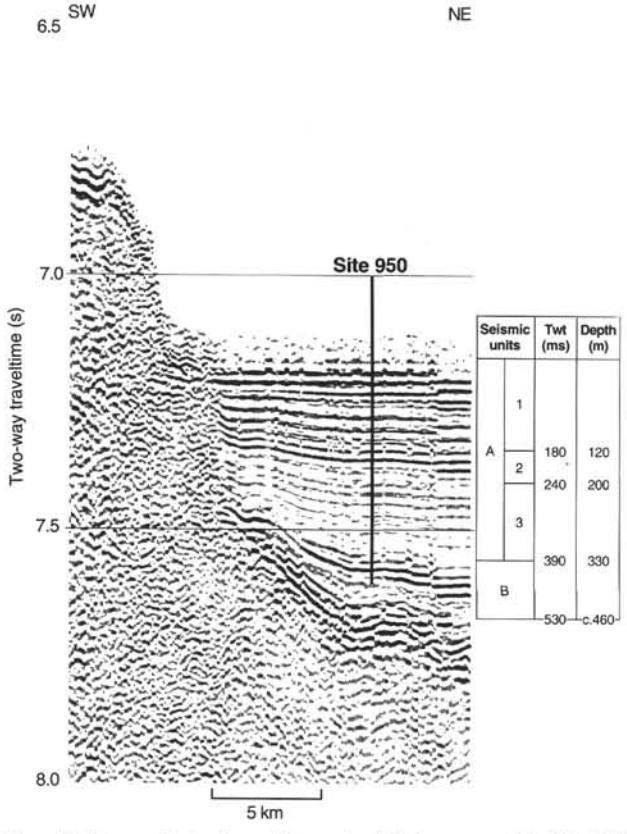

Figure 2. Processed seismic profile acquired during approach to Site 950.

the acoustic basement is seen as an irregular high-amplitude reflector at 500–600 ms two-way traveltime (twt) below the seafloor.

The sediment fill can be divided into two major units based on the reflection patterns. The upper unit, A, is characterized by abundant reflectors of relatively high amplitude. The vertical (twt) spacing of the reflectors is a remarkably uniform 20–30 ms throughout the unit. The reflectors onlap the basement high and show some drag along the flank. About 1 km off the flank the reflectors are almost horizontal except for some drape over topographic features in the substratum. The lower unit, B, is identified by a series of high-amplitude reflectors that onlap the basement high and drape the relief of the acoustic basement. Some of the reflectors are parallel and some show basinward divergence. In the divergent intervals reflectors lose their continuity.

Unit A can be subdivided into three subunits: A1, A2, and A3. The internal reflectors in Subunit A1 are relatively strong, compared to the reflectors in Subunits A2 and A3. The Subunit A1/A2 and A2/A3 boundaries are defined by relatively strong reflectors at 180 ms and 240 ms at Site 950. Ignoring the strong seafloor reflector, there appears to be a gradual downward increase in reflector amplitude in Subunit A1. This tendency vanishes toward the onlap surface.

An excellent sonic log was obtained in Hole 950A. By combining the log data with the MST velocities measured on the APC cores (0–150 m) a complete velocity profile was obtained down to 340 mbsf (Fig. 3).

Based on this log, a twt–depth relation was established as shown in Figure 4. This relation will enable a precise correlation between seismic profiles and lithological/stratigraphical observations in the cores.

In the underway (UW) seismic profile, the Unit A/B boundary correlates with the log Unit IV/V boundary—the surface of the red clay sequence at ~330 mbsf (see "Downhole Measurements," this chapter). The internal subunits in Unit A probably mainly reflect large-scale changes in turbidite thickness and lithology. In Unit B the upper parallel reflectors seem to represent the red clay, and the chaotic interval below seems to image the turbidites encountered in the cores below 366 mbsf.

OPERATIONS

Port Call in Bridgetown, Barbados

ODP Leg 157 began with the first mooring line at Bridgetown Harbor, Barbados, at 1000, local time, 24 July 1994. The port call entailed the loading of hardware that had been offloaded and stored in Barbados prior to Leg 156. Also retrieved from storage in Barbados

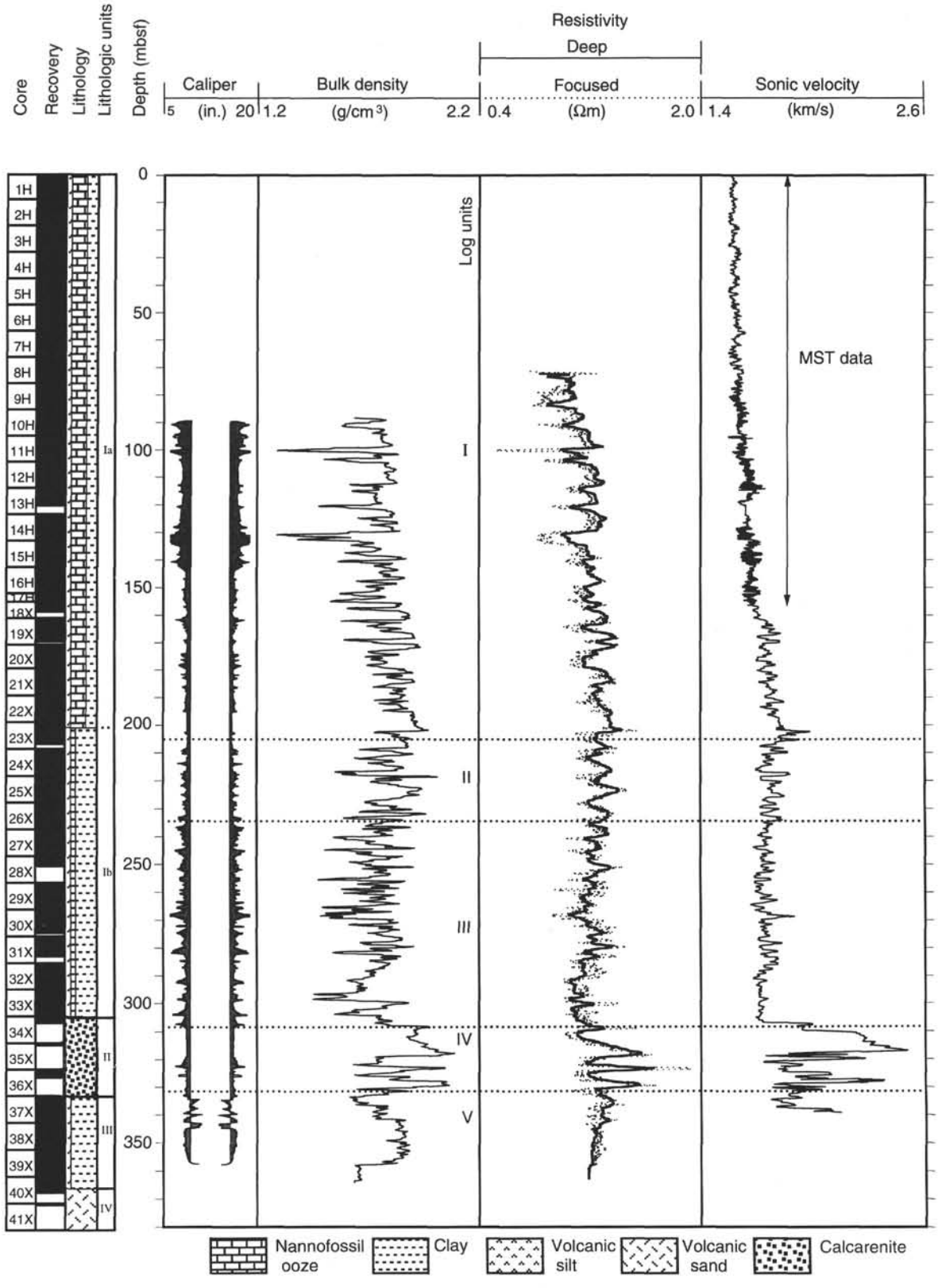

Figure 3. Hole 950A physical logs summary. Caliper data from the HLDT, shown with bulk density data from the HLDT, deep phasor induction and spherically focused resistivity from the phasor DIT, and sonic velocity data from the long-spaced SDT. The central white area in the caliper log represents the XCB bit size (10 5/8 in.); shading represents the "washed out" portion of the hole from the bit size to actual measured diameter. The sonic velocity data have been processed to remove cycle skips and have been spliced with core MST velocity measurements above 150 mbsf. The bulk density and velocity data are unsmoothed.

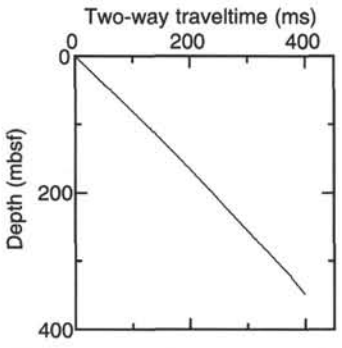

Figure 4. Relationship between depth and two-way traveltime, measured from the seafloor reflector.

were two hard-rock guide bases (HRB) and various running tools. Additional hardware from College Station, including one reentry cone (Russian manufacture), two new nonmagnetic drill collars, and two tapered drill collars to replace the 7 ¼ in. drill collar in the BHA, were taken aboard during the port call, as were sepiolite, barite, and cement.

The standard freight shipments were exchanged and crew changes were made. Fresh water tanks were filled and approximately 1322 metric tons of marine gasoil were loaded. The replacement of the forward core winch bearing could not be completed during the port call because a grease seal was not included in the shipment of replacement parts. Because the forward winch contained only 5550 m, it was not going to be used during operations at the Madeira Abyssal Plain (MAP) sites. Arrangements were to be made to transport the grease seal to the ship when the vessel reached the VICAP area during the last half of the leg. The core winch was not re-assembled.

A diver survey of the stern tubes and skeg thrusters was made to see if any hydrophone cable fouled in the propellers as a result of a hydrophone being cut during vertical seismic profile (VSP) downhole measurement operations on Leg 156. The survey did not show any foreign material in or damage to the skeg or main propellers.

At 1800, 27 July, the last line was away and the *JOIDES Resolution* departed for MAP-1.

Bridgetown to Site 950 Transit

At 1813, 27 July, a flash-over occurred in propulsion motor P15A on the starboard shaft almost immediately after putting the motor in service, resulting in an immediate shut-down of the starboard shaft. An inspection indicated that a brush holder ring had burned and the starboard shaft was operated with only four motors on line. During routine maintenance in port, a very low insulation resistance was discovered in the armature circuit of P13B, which necessitated the disabling of this motor.

At 1824, 27 July, the breaker for starboard propulsion motor P13A tripped off-line. On resetting the breaker, the electrician noticed a malfunction in the Thyrig bay assigned to this motor and immediately shut down the power to this unit. The vessel proceeded with only three motors on-line driving the starboard shaft. The P13A motor was back on line at 0543, 28 July, after the electrician replaced two blown fuses.

The electricians installed a temporary jumper cable from the P13B motor to the Thyrig bay and had this motor in operation by 1600, 30 July. At the same time, the ocean swells calmed, allowing the average speed of the *JOIDES Resolution* to increase from 9.3 to 9.7 kt, continuing to build during the voyage to the MAP area. On 2 August, the port shaft had to be shut down for 30 min while a high-pressure oil leak was repaired on the port gearbox.

The vessel's speed continued to increase and by the time the air guns were deployed at MAP-1, the average speed for the transit had improved to 10.2 kt. The clock was advanced 3 hr during the transit.

Site 950 (MAP-1)

At 1645, 5 August, the *JOIDES Resolution* slowed to 6 kt after a nine day transit from Barbados, and the seismic gear was deployed as the vessel approached the Site 950 (MAP-1) survey area from the southwest. After a 2 hr survey, the gear was retrieved and the vessel returned to the site. A beacon was deployed at 2000, 5 August.

A standard short drill collar APC/XCB bottom hole assembly (BHA) comprising a nonmagnetic drill collar (NMDC) and a drag-type 10-1/8 in. polycrystalline diamond compact (PDC) drill bit was assembled to begin the pipe trip. The BHA was complete with a new tapered drill collar in place of the 7-1/4 in. drill collar and assorted subs. The initial running in the hole was lengthened because of the standard practice of measuring and passing a drift through the drill string on the initial pipe trip of an ODP leg.

The water depth was determined to be 5437.8 meters below sea level (mbsl), drill-pipe measurement (DPM), with Core 157-950A-1H, and the core recovered 8.9 m of clayey nannofossil mixed sediment (Table 1). APC coring advanced to 154.4 mbsf (Core 17H). The kelly hose ruptured while pressuring up to fire the last APC core, Core 17H, and the core penetrated only 3 m in the hard, sticky clays. After replacing the kelly hose, coring resumed with the XCB system and advanced to 381.3 mbsf (Cores 18X through 41X) where contact with volcanic sandstone reduced the rate of penetration (ROP) to a very slow 4 m/hr. This was considered XCB refusal and the end of the hole. The hole was then prepared for logging by a flush of sepiolite mud and a wiper trip.

The seismic-stratigraphic combo, which logged down and up the hole from 363.4 mbsf, initiated the logging. The second tool, the lithoporosity combo, logged up from 359 mbsf. The third tool, a geochemical combo, logged the hole from 324 mbsf. Finally, the FMS logged up from 314 mbsf. Coverage of the open hole section was very good with the first two strings encountering only a minimal amount of hole fill (~16 m). The geochemical and FMS strings lost the bottom 50 m of the hole. The hole deviation maximum of 3° occurred at 276 mbsf.

After rigging down the logging tools and pulling pipe, the *JOIDES Resolution* was under way to prospective Site MAP-4 by 2330, 10 August.

LITHOSTRATIGRAPHY

The sedimentary sequence recovered at Site 950 comprises 381 m of clayey nannofossil mixed sediment and nannofossil clay turbidites interbedded with pelagic nannofossil oozes, mixed sediments, and clays (Figs. 5 and 6). The age of the sedimentary sequence ranges from the late Pleistocene to no older than early Eocene. The upper part of the sequence (from 0 to 333 mbsf) is dominated by thick turbidite muds separated by thin pelagic ooze, mixed sediment, or clay interbeds. Below 333 mbsf, the sequence consists mainly of pelagic red clay that contains minor thin nannofossil clay turbidites and zeolitic ash bands. The sedimentary sequence at Site 950 is divided into four lithologic units based primarily on changes in sediment composition and sedimentary regime (Fig. 5). The uppermost unit (I) was further subdivided based on variations in clay content.

Unit I

Interval: Sections 157-950A-1H-1 through 34X-2
Depth: 0–305.6 mbsf

Table 1. Coring summary, Hole 950A.

Core	Date (August 1994)	Time (UTC)	Sub-bottom (m) Top	Sub-bottom (m) Bottom	Cored (m)	Recovered (m)	Recovery (%)	Section	Length (m)	Depth (mbsf) Top	Depth (mbsf) Bottom	Samples
157-950A-												
1H	6	1200	0.0	8.9	8.9	8.93	100.0					
								1	1.50	0.00	1.50	
								2	1.50	1.50	3.00	
								3	1.50	3.00	4.50	
								4	1.50	4.50	6.00	IW 145–150
								5	1.50	6.00	7.50	HS 0–5
								6	1.25	7.50	8.75	
								CC	0.18	8.75	8.93	
2H	6	1350	8.9	18.4	9.5	9.57	101.0					
								1	1.50	8.90	10.40	
								2	1.50	10.40	11.90	
								3	1.50	11.90	13.40	
								4	1.50	13.40	14.90	IW 145–150
								5	1.50	14.90	16.40	HS 0–5
								6	1.50	16.40	17.90	
								7	0.37	17.90	18.27	
								CC	0.20	18.27	18.47	
3H	6	1500	18.4	27.9	9.5	9.58	101.0					
								1	1.50	18.40	19.90	
								2	0.30	19.90	20.20	Fell out hole in liner; unoriented, disturbed
								3	1.50	20.20	21.70	
								4	1.50	21.70	23.20	
								5	1.50	23.20	24.70	
								6	1.50	24.70	26.20	IW 145–150
								7	1.50	26.20	27.70	HS 0–5
								CC	0.28	27.70	27.98	
4H	6	1620	27.9	37.4	9.5	9.75	102.0					
								1	1.50	27.90	29.40	
								2	1.50	29.40	30.90	
								3	1.50	30.90	32.40	
								4	1.50	32.40	33.90	
								5	1.50	33.90	35.40	IW 145–150
								6	1.50	35.40	36.90	HS 0–5
								7	0.50	36.90	37.40	
								CC	0.25	37.40	37.65	
5H	6	1745	37.4	46.9	9.5	9.74	102.0					
								1	1.50	37.40	38.90	
								2	1.50	38.90	40.40	
								3	1.50	40.40	41.90	
								4	1.50	41.90	43.40	
								5	1.50	43.40	44.90	IW 145–150
								6	1.50	44.90	46.40	HS 0–5
								7	0.62	46.40	47.02	
								CC	0.12	47.02	47.14	
6H	6	1900	46.9	56.4	9.5	9.78	103.0					
								1	1.20	46.90	48.10	
								2	1.50	48.10	49.60	
								3	1.50	49.60	51.10	
								4	1.50	51.10	52.60	IW 145–150
								5	1.50	52.60	54.10	HS 0–5
								6	1.50	54.10	55.60	
								CC	1.08	55.60	56.68	
7H	6	2015	56.4	65.9	9.5	9.95	105.0					
								1	1.50	56.40	57.90	
								2	1.50	57.90	59.40	
								3	1.50	59.40	60.90	IW 145–150
								4	1.50	60.90	62.40	HS 0–5
								5	1.50	62.40	63.90	
								6	1.50	63.90	65.40	
								7	0.73	65.40	66.13	
								CC	0.22	66.13	66.35	
8H	6	2150	65.9	75.4	9.5	9.72	102.0					
								1	1.50	65.90	67.40	
								2	1.50	67.40	68.90	
								3	1.50	68.90	70.40	
								4	1.50	70.40	71.90	
								5	1.50	71.90	73.40	IW 145–150
								6	1.50	73.40	74.90	HS 0–5
								7	0.62	74.90	75.52	
								CC	0.10	75.52	75.62	
9H	6	2305	75.4	84.9	9.5	9.68	102.0					
								1	1.50	75.40	76.90	
								2	1.50	76.90	78.40	
								3	1.50	78.40	79.90	
								4	1.50	79.90	81.40	IW 1450150
								5	1.50	81.40	82.90	HS 0–5
								6	1.50	82.90	84.40	
								7	0.53	84.40	84.93	
								CC	0.15	84.93	85.08	
10H	7	0030	84.9	94.4	9.5	9.23	97.1					
								1	1.50	84.90	86.40	
								2	1.50	86.40	87.90	
								3	0.10	87.90	88.00	Split liner
								4	1.50	88.00	89.50	IW 145–150
								5	1.50	89.50	91.00	HS 0–5
								6	1.50	91.00	92.50	
								7	1.38	92.50	93.88	

Table 1 (continued).

Core	Date (August 1994)	Time (UTC)	Sub-bottom (m) Top	Sub-bottom (m) Bottom	Cored (m)	Recovered (m)	Recovery (%)	Section	Length (m)	Depth (mbsf) Top	Depth (mbsf) Bottom	Samples
								CC	0.25	93.88	94.13	
11H	7	0150	94.4	103.9	9.5	9.66	101.0					
								1	1.50	94.40	95.90	
								2	1.50	95.90	97.40	
								3	1.50	97.40	98.90	
								4	1.50	98.90	100.40	
								5	1.50	100.40	101.90	HS 0–5
								6	1.50	101.90	103.40	
								7	0.55	103.40	103.95	
								CC	0.11	103.95	104.06	
12H	7	0305	103.9	113.4	9.5	9.80	103.0	1	1.50	103.90	105.40	
								2	1.50	105.40	106.90	
								3	1.50	106.90	108.40	
								4	1.50	108.40	109.90	IW 145–150
								5	1.50	109.90	111.40	HS 0–5
								6	1.50	111.40	112.90	
								7	0.55	112.90	113.45	
								CC	0.25	113.45	113.70	
13H	7	0420	113.4	122.9	9.5	6.81	71.7					
								1	1.50	113.40	114.90	
								2	1.50	114.90	116.40	
								3	1.50	116.40	117.90	
								4	1.50	117.90	119.40	HS 0–5
								5	0.43	119.40	119.83	
								CC	0.38	119.83	120.21	
14H	7	0540	122.9	132.4	9.5	9.16	96.4					
								1	1.50	122.90	124.40	
								2	1.50	124.40	125.90	
								3	1.50	125.90	127.40	
								4	1.50	127.40	128.90	IW 145–150
								5	1.50	128.90	130.40	
								6	1.50	130.40	131.90	
								7	0.16	131.90	132.06	Paleo sample 14–16
								CC	0.00	132.06	132.06	
15H	7	0650	132.4	141.9	9.5	9.00	94.7					
								1	1.50	132.40	133.90	
								2	1.50	133.90	135.40	
								3	1.50	135.40	136.90	
								4	1.50	136.90	138.40	
								5	1.50	138.40	139.90	HS 0–5
								6	1.28	139.90	141.18	
								CC	0.22	141.18	141.40	
16H	7	0800	141.9	151.4	9.5	9.85	103.0					
								1	1.50	141.90	143.40	
								2	1.50	143.40	144.90	
								3	1.50	144.90	146.40	
								4	1.50	146.40	147.90	IW 145–150
								5	1.50	147.90	149.40	HS 0–5
								6	1.40	149.40	150.80	
								7	0.74	150.80	151.54	
								CC	0.21	151.54	151.75	
17H	7	1110	151.4	154.4	3.0	4.95	165.0	1	0.75	151.40	152.15	
								2	0.75	152.15	152.90	0–21 lost in barrel
								3	1.47	152.90	154.37	147–150 lost in barrel
								4	0.62	154.37	154.99	62–143 lost in barrel
								CC	0.31	154.99	155.30	
18X	7	1305	154.4	160.3	5.9	4.01	67.9					
								1	1.50	154.40	155.90	
								2	1.50	155.90	157.40	IW 145–150
								3	0.47	157.40	157.87	HS 0–5
								CC	0.54	157.87	158.41	
19X	7	1440	160.3	169.9	9.6	8.92	92.9					
								1	1.50	160.30	161.80	
								2	1.50	161.80	163.30	
								3	1.50	163.30	164.80	
								4	1.50	164.80	166.30	
								5	1.50	166.30	167.80	HS 0–5
								6	0.83	167.80	168.63	
								CC	0.59	168.63	169.22	
20X	7	1605	169.9	178.5	8.6	9.90	115.0					
								1	1.50	169.90	171.40	
								2	1.50	171.40	172.90	
								3	1.50	172.90	174.40	
								4	1.50	174.40	175.90	IW 140–150
								5	1.50	175.90	177.40	HS 0–5
								6	1.50	177.40	178.90	
								7	0.40	178.90	179.30	
								CC	0.50	179.30	179.80	
21X	7	1725	178.5	188.2	9.7	9.85	101.0					
								1	1.50	178.50	180.00	
								2	1.50	180.00	181.50	
								3	1.50	181.50	183.00	
								4	1.50	183.00	184.50	
								5	1.50	184.50	186.00	HS 0–5
								6	1.50	186.00	187.50	
								7	0.51	187.50	188.01	

Table 1 (continued).

Core	Date (August 1994)	Time (UTC)	Sub-bottom (m) Top	Sub-bottom (m) Bottom	Cored (m)	Recovered (m)	Recovery (%)	Section	Length (m)	Depth (mbsf) Top	Depth (mbsf) Bottom	Samples
								CC	0.34	188.01	188.35	
22X	7	1850	188.2	197.8	9.6	9.92	103.0					
								1	1.50	188.20	189.70	
								2	1.50	189.70	191.20	
								3	1.50	191.20	192.70	IW 145–150
								4	1.50	192.70	194.20	
								5	1.50	194.20	195.70	HS 0–5
								6	1.50	195.70	197.20	
								7	0.52	197.20	197.72	
								CC	0.40	197.72	198.12	
23X	7	2020	197.8	207.5	9.7	8.35	86.1					
								1	1.50	197.80	199.30	
								2	1.50	199.30	200.80	
								3	1.50	200.80	202.30	
								4	1.50	202.30	203.80	HS 0–5
								5	1.50	203.80	205.30	
								6	0.53	205.30	205.83	
								CC	0.32	205.83	206.15	
24X	7	2155	207.5	217.2	9.7	9.78	101.0					
								1	1.50	207.50	209.00	
								2	1.50	209.00	210.50	
								3	1.50	210.50	212.00	
								4	1.50	212.00	213.50	
								5	1.50	213.50	215.00	HS 0–5
								6	1.50	215.00	216.50	
								7	0.36	216.50	216.86	
								CC	0.42	216.86	217.28	
25X	7	2325	217.2	226.8	9.6	9.41	98.0					
								1	1.50	217.20	218.70	
								2	1.50	218.70	220.20	
								3	1.50	220.20	221.70	IW 145–150
								4	1.50	221.70	223.20	HS 0–5
								5	1.50	223.20	224.70	
								6	1.50	224.70	226.20	
								CC	0.41	226.20	226.61	
26X	8	0045	226.8	236.5	9.7	9.61	99.1					
								1	1.50	226.80	228.30	
								2	1.50	228.30	229.80	
								3	1.50	229.80	231.30	
								4	1.50	231.30	232.80	
								5	1.50	232.80	234.30	HS 0–5
								6	1.50	234.30	235.80	
								CC	0.61	235.80	236.41	
27X	8	0210	236.5	246.1	9.6	9.88	103.0					
								1	1.50	236.50	238.00	
								2	1.50	238.00	239.50	
								3	1.50	239.50	241.00	
								4	1.50	241.00	242.50	
								5	1.50	242.50	244.00	IW 145–150
								6	1.50	244.00	245.50	HS 0–5
								7	0.46	245.50	245.96	
								CC	0.42	245.96	246.38	
28X	8	0345	246.1	255.7	9.6	4.14	43.1					
								1	1.50	246.10	247.60	
								2	1.50	247.60	249.10	HS 0–5
								3	0.54	249.10	249.64	
								CC	0.60	249.64	250.24	
29X	8	0515	255.7	265.4	9.7	9.57	98.6					
								1	1.50	255.70	257.20	
								2	1.50	257.20	258.70	
								3	1.50	258.70	260.20	
								4	1.50	260.20	261.70	
								5	1.50	261.70	263.20	
								6	1.50	263.20	264.70	HS 0–5
								7	0.15	264.70	264.85	
								CC	0.42	264.85	265.27	
30X	8	0700	265.4	275.1	9.7	9.01	92.9					
								1	1.50	265.40	266.90	
								2	1.50	266.90	268.40	
								3	1.50	268.40	269.90	
								4	1.50	269.90	271.40	IW 140–150
								5	1.50	271.40	272.90	HS 0–5
								6	1.17	272.90	274.07	
								CC	0.34	274.07	274.41	
31X	8	0840	275.1	284.8	9.7	7.72	79.6					
								1	1.50	275.10	276.60	
								2	1.50	276.60	278.10	
								3	1.50	278.10	279.60	
								4	1.50	279.60	281.10	
								5	1.29	281.10	282.39	HS 0–5
								CC	0.43	282.39	282.82	
32X	8	1030	284.8	294.4	9.6	9.73	101.0					
								1	1.50	284.80	286.30	
								2	1.50	286.30	287.80	
								3	1.50	287.80	289.30	
								4	1.50	289.30	290.80	
								5	1.50	290.80	292.30	
								6	1.50	292.30	293.80	HS 0–5

Table 1 (continued).

Core	Date (August 1994)	Time (UTC)	Sub-bottom (m) Top	Sub-bottom (m) Bottom	Cored (m)	Recovered (m)	Recovery (%)	Section	Length (m)	Depth (mbsf) Top	Depth (mbsf) Bottom	Samples
								7	0.41	293.80	294.21	
								CC	0.32	294.21	294.53	
33X	8	1235	294.4	304.1	9.7	9.88	102.0					
								1	1.50	294.40	295.90	
								2	1.50	295.90	297.40	
								3	1.50	297.40	298.90	
								4	1.50	298.90	300.40	
								5	1.50	300.40	301.90	IW 140–150
								6	1.50	301.90	303.40	HS 0–5
								7	0.48	303.40	303.88	
								CC	0.40	303.88	304.28	
34X	8	1400	304.1	313.7	9.6	2.86	29.8					
								1	1.50	304.10	305.60	
								2	1.00	305.60	306.60	HS 0–5
								CC	0.36	306.60	306.96	
35X	8	1530	313.7	323.3	9.6	1.21	12.6					
								1	0.83	313.70	314.53	HS 78–83
								CC	0.38	314.53		HS 78–83
36X	8	1710	323.3	333.0	9.7	3.38	34.8					
								1	1.50	323.30	324.80	IW 140–150
								2	1.50	324.80	326.30	HS 0–5
								CC	0.38	326.30	326.68	
37X	8	1830	333.0	342.6	9.6	9.88	103.0					
								1	1.50	333.00	334.50	
								2	1.50	334.50	336.00	
								3	1.50	336.00	337.50	
								4	1.50	337.50	339.00	
								5	1.50	339.00	340.50	
								6	1.50	340.50	342.00	HS 0–5
								7	0.43	342.00	342.43	
								CC	0.45	342.43	342.88	
38X	8	1955	342.6	352.3	9.7	9.88	102.0					
								1	1.50	342.60	344.10	
								2	1.50	344.10	345.60	
								3	1.50	345.60	347.10	
								4	1.50	347.10	348.60	
								5	1.50	348.60	350.10	HS 0–5
								6	1.50	350.10	351.60	
								7	0.45	351.60	352.05	
								CC	0.43	352.05	352.48	
39X	8	2135	352.3	362.0	9.7	9.90	102.0					
								1	1.50	352.30	353.80	
								2	1.50	353.80	355.30	
								3	1.50	355.30	356.80	
								4	1.50	356.80	358.30	
								5	1.50	358.30	359.80	
								6	1.50	359.80	361.30	
								7	0.47	361.30	361.77	
								CC	0.43	361.77	362.20	
40X	8	0030	362.0	371.6	9.6	6.19	64.5					
								1	1.50	362.00	363.50	
								2	1.50	363.50	365.00	
								3	1.50	365.00	366.50	
								4	1.24	366.50	367.74	HS 0–5
								CC	0.45	367.74	368.19	
41X	8	0500	371.6	381.3	9.7	1.00	10.3					
								1	0.56	371.60	372.16	
								CC	0.44	372.16	372.60	
Coring totals					381.3	339.1	88.90					

Notes: Hole 950A located at 31°9.011′N, 25° 36.004′W. Water depth from sea surface = 5437.8 m.

Unit I is at least 305.6 m thick and comprises a sequence of medium to very thick beds of green or gray clayey nannofossil mixed sediments, medium to very thick beds of clayey nannofossil ooze (commonly underlain by foraminiferal sands), and very thin to thin interbeds of clay, clayey nannofossil mixed sediment, and clayey nannofossil ooze. Extensive research in this area (Weaver and Kuijpers, 1983; Weaver and Rothwell, 1987; Weaver and Thomson, 1987, and references therein; Weaver et al., 1989; Weaver et al., 1992; Rothwell et al., 1992) has demonstrated that the medium to very thick beds of green and gray clayey nannofossil mixed sediments and medium to very thick beds of clayey nannofossil ooze are distal turbidite muds derived from the northwest African margin, Madeira, and the Canary volcanic islands, and from seamounts to the west, respectively. The thin interbeds of clay, clayey nannofossil mixed sediment, and clayey nannofossil ooze that commonly separate the turbiditic muds represent pelagic intervals (Weaver and Kuijpers, 1983).

Unit I therefore consists of a sequence of thick turbidite muds interbedded with thin pelagic intervals that may be either nannofossil ooze, mixed sediment, or clay. Calcium carbonate data (Fig. 7) throughout this unit shows a marked decrease in $CaCO_3$ content in the pelagic intervals below 100 mbsf. Therefore, Unit I is subdivided into two Subunits, Ia and Ib, based on the increasing clay content in the pelagic intervals. The boundary between Subunits Ia and Ib is placed at 150 mbsf, below which the pelagic intervals are clays, and above which they are clayey nannofossil mixed sediments, clayey nannofossil oozes, and nannofossil oozes in the sediment classification of Mazzullo et al. (1988). The subdivision of Unit I into Subunits Ia and Ib at 150 mbsf also correlates with greater variability in the $CaCO_3$ content of the turbidites below 150 mbsf.

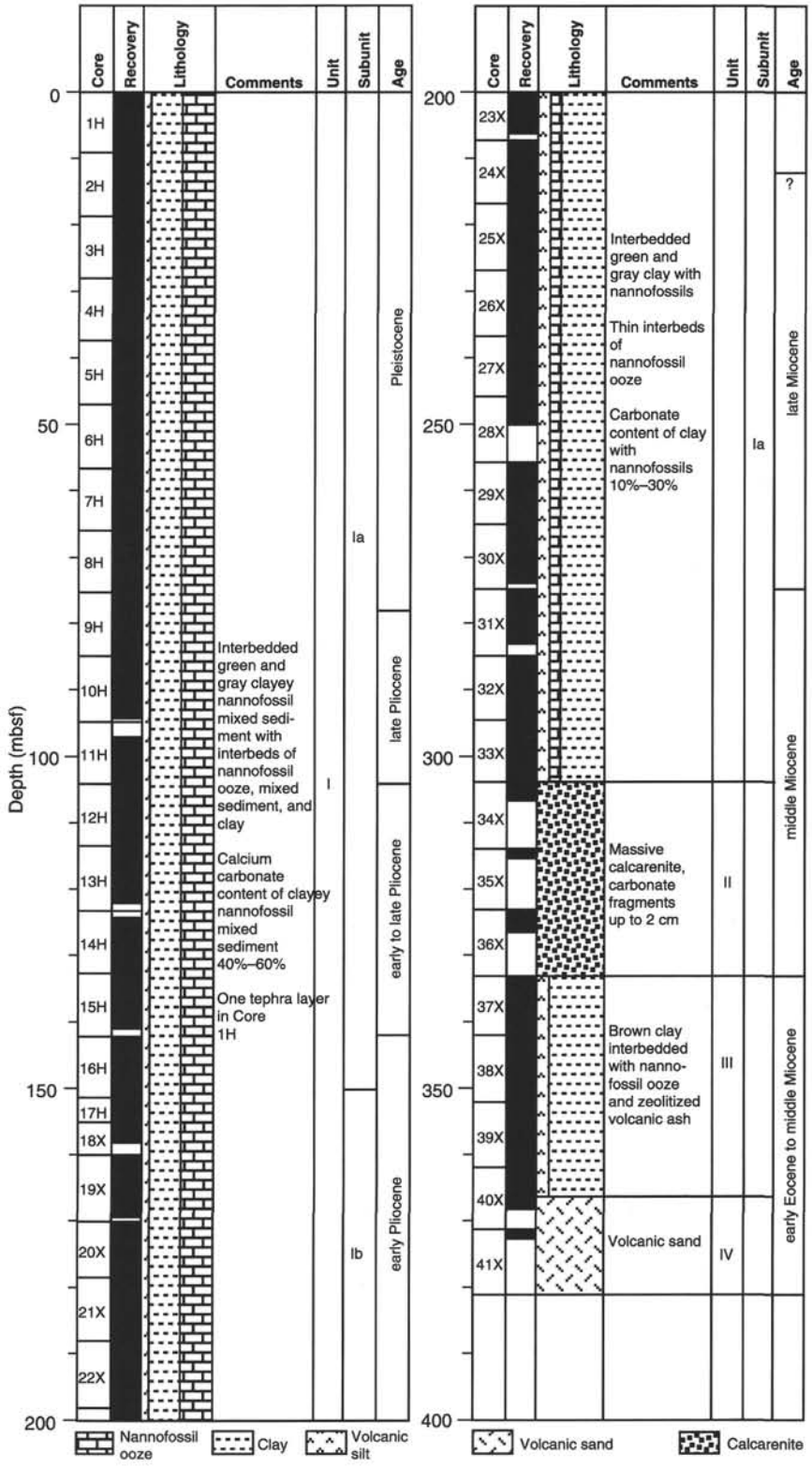

Figure 5. Lithologic summary for Hole 950A, showing the main lithologic units identified with age as well as a generalized graphic lithology.

Clayey Nannofossil Mixed Sediments (gray and green turbidites)

Medium to very thick bedded turbidite muds are dominant throughout Unit I. These beds are visually striking in their distinctive color, typically great thickness (commonly several meters), and largely structureless appearance. The turbidite muds are very distal in character and fall into the Te division of Bouma (1962). Some show thin parallel weakly laminated or graded silty bases, but the greater part of each unit consists of structureless mud, the upper part of which may be moderately to weakly bioturbated. Bioturbation rarely extends for more than 40 cm below the upper boundary of the depositional unit. Mud units less than 0.5 m thick may be bioturbated

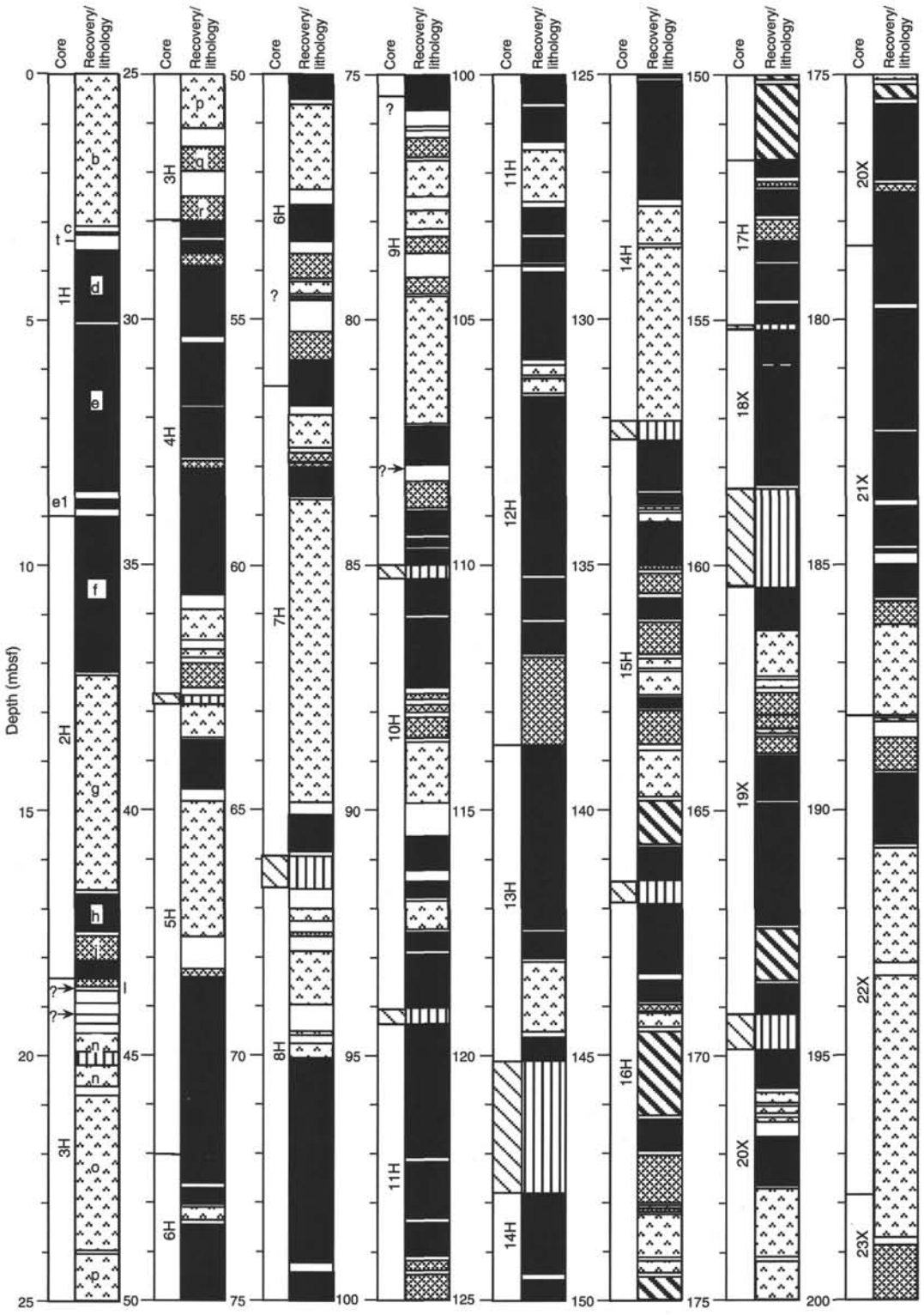

Figure 6. Genetic log of the sedimentary succession cored at Hole 950A showing the occurrence of individual turbidites, their compositional type, and the position of pelagic interbeds within the sequence.

throughout. Nearly all of the turbidite muds show sharp, straight, or sometimes scoured basal contacts and burrowed upper contacts.

Petrographically the turbidite muds are clayey nannofossil mixed sediments in the classification of Mazzullo et al. (1988), although in Subunit Ib (i.e., below 150 mbsf), they become nannofossil clays or clay in composition. Examination of smear slides from the structureless turbidite mud intervals show that they are composed primarily of clay minerals and coccolith plates with lesser amounts of silt-size material (mainly quartz, dolomite, feldspar, pyrite, accessory minerals, foraminiferal test fragments and debris, and in certain turbidites, si-

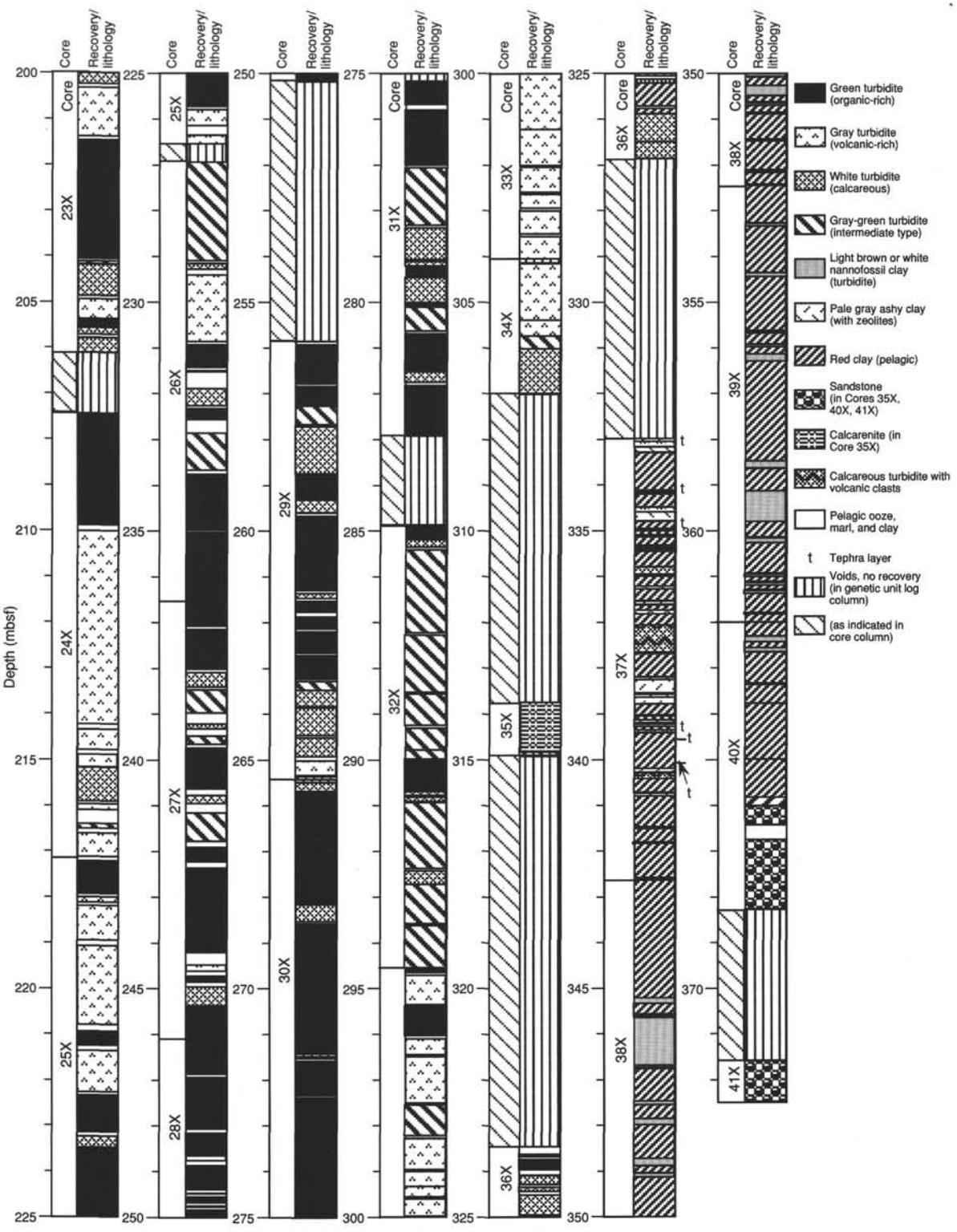

Figure 6 (continued).

liceous microfossils and volcanic glass). Minor amounts of silt-size material are found throughout the turbidite mud intervals suggesting that they are ungraded and thus fall into the E3 division of Piper (1978). Silt-size material becomes more common coarser grained toward the bases of individual units and may form distinct graded or weakly laminated silty bases. These contain, in addition to grains described above, complete benthic and planktonic foraminifers.

Distinctly colored turbidite muds recognized within Unit I are composed of visually striking light green to dark olive green muds and gray muds. In the upper part of the sediment sequence elsewhere in the Madeira Abyssal Plain, de Lange et al. (1987) have shown green turbidite muds to be organic-rich and gray turbidites to be volcanic rich.

Organic-rich Turbidites

Organic-rich turbidites range from 0.1 to 4.2 m thick and form the dominant sediment type within Unit I. They commonly have a char-

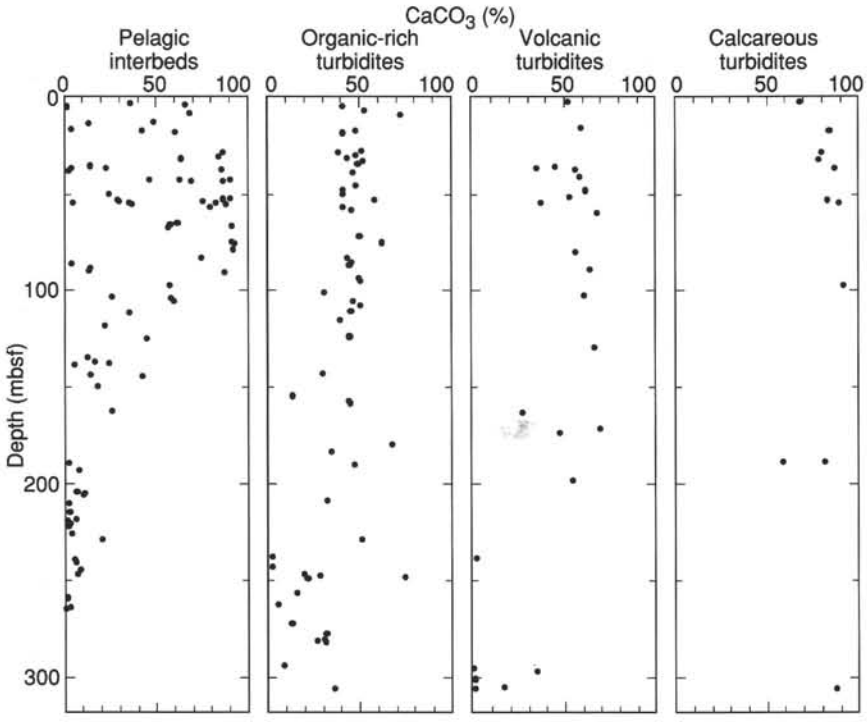

Figure 7. Downcore plot of calcium carbonate content through Unit I at Hole 950A.

acteristic two-tone coloration, with a pale green upper part and darker green lower part (Fig. 8). The intensity of the green coloration reflects the organic carbon content, with darker green units having higher organic carbon contents (see "Organic Geochemistry," this chapter). The boundary between the light green upper part and the darker green lower part of individual units marks the position of an oxidation front; and the paler green upper part represents an interval where organic carbon has been removed by oxidation (Colley and Thomson, 1985; Thomson et al., 1987). In the upper part of Unit I, the oxidation front shows a distinct color gradation, typically having a thin interval of intermediate green between the light green upper part and darker green lower part (Fig. 9). However, turbidites from deeper in the sediment column in Unit I show a very abrupt transition from the oxic to the reduced part, with no intermediate green bands or other structure to the oxidation fronts (Fig. 10). The upper pale green parts of these turbidites are typically bioturbated, while the lower darker green reduced parts are typically homogeneous, although in some cases, bioturbation does penetrate the oxidation front (Fig. 11). Organic-rich turbidites from between 0–100 mbsf commonly contain small, but significant, quantities (1%–3%) of siliceous microfossils (mainly broken diatom frustules, sponge spicules, and rare radiolarians; Fig. 12). However, siliceous microfossils are very rare or absent from organic-rich turbidites from below 100 mbsf. Sometimes organic-rich turbidites show weakly laminated or graded silty bases, which commonly contain significant amounts of framboidal pyrite (Fig. 13). Clusters and specks of framboidal pyrite are commonly found suspended within homogeneous Bouma Te division turbidite muds (Fig. 14). These may represent the remains of fecal pellets that originally contained foraminifers and other microfossils.

Volcanic-rich Turbidites

The volcanic-rich turbidites range from 0.1 to 6 m thick and form an important sediment type in Unit I (Fig. 6). Like the organic-rich turbidites, the volcanic-rich turbidites typically show burrowed upper contacts and a bioturbated upper part, although for the most part they are structureless. Occasionally they have thin, coarser grained, laminated or graded, but poorly sorted, silty bases. These contain anhedral feldspar, pyroxenes, and volcanically derived accessory minerals. Some bases contain felsic volcanic glass shards. Volcanic-rich turbidites are typically various shades of gray or grayish-brown (turbidites are common below Core 24X). They generally do not show the distinctive two-tone coloration of the organic-rich turbidites, but some show slightly paler upper parts. These may represent turbidites of intermediate composition.

Turbidite Beds of Clayey Nannofossil Ooze

Medium to very thick bedded structureless white nannofossil oozes, commonly underlain by massive foraminiferal sands of variable thickness are the third most common sediment type in lithologic Unit I. These calcareous oozes lack foraminifers except near their bases, which suggests that they have been removed by gravitative sorting. These oozes are interpreted as biogenic turbidites, derived from instability on the flanks of nearby seamounts west of the plain. They have $CaCO_3$ values of 60%–90% (Fig. 7), and the beds range from 0.1 to 2 m thick; although they occur sporadically throughout the sequence, they never achieve the great thicknesses shown by the other two turbidite groups. Some have at their bases foraminiferal sands that are may be up to 40 cm thick (e.g., Sample 157-950A-23X-2, 60–101 cm).

Pelagic Interbeds of Clay, Clayey Nannofossil Mixed Sediment, and Nannofossil Ooze

Medium-bedded to very thin interbeds of white, whitish-gray, gray, and brown nannofossil ooze, clayey nannofossil ooze, clayey nannofossil mixed sediment, and clay occur throughout the sequence and frequently separate the medium to very thick bedded turbidite muds. They are interpreted as representing pelagic accumulation. These sediments are slightly to heavily bioturbated throughout, or they may appear featureless. Many intervals show small dark gray flecks and blebs, or purplish chemical laminae, or diffuse patchy mottling, probably because of remobilized manganese and copper. Although the upper boundaries of these units may be sharp (if the overlying unit is turbiditic), lower boundaries are commonly grada-

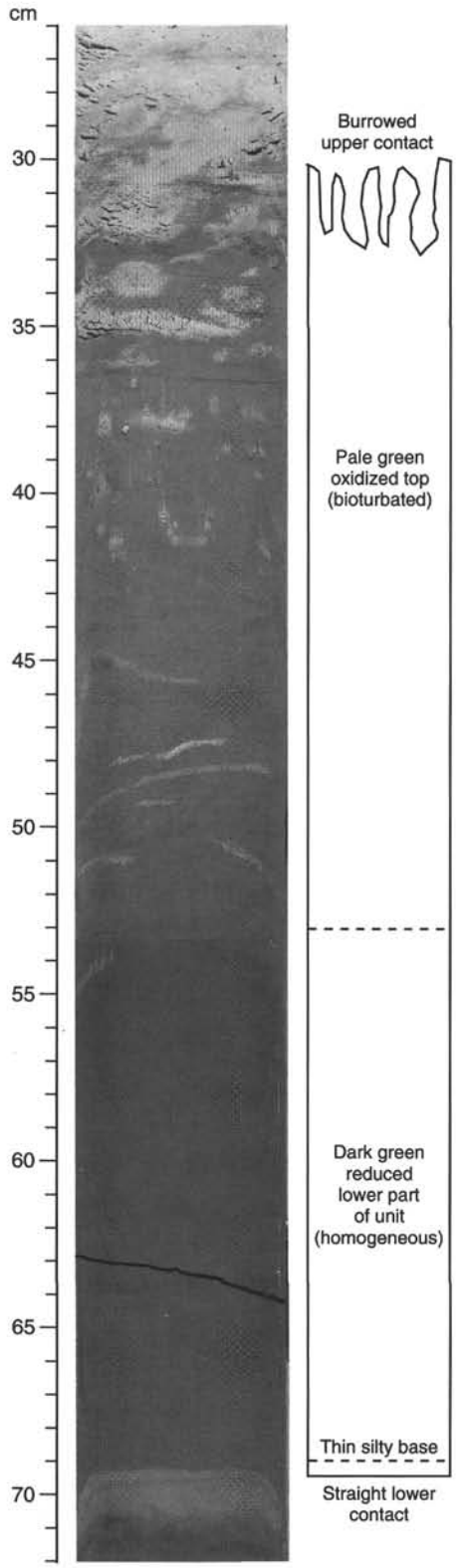

Figure 8. Organic-rich turbidite, showing the typical structure of this class of turbidite. Note the burrowed upper boundary, the pale green bioturbated upper part, the oxidation front, the homogeneous, darker green lower part, and the sharp basal contact. Interval 157-950A-10H-6, 26–72 cm.

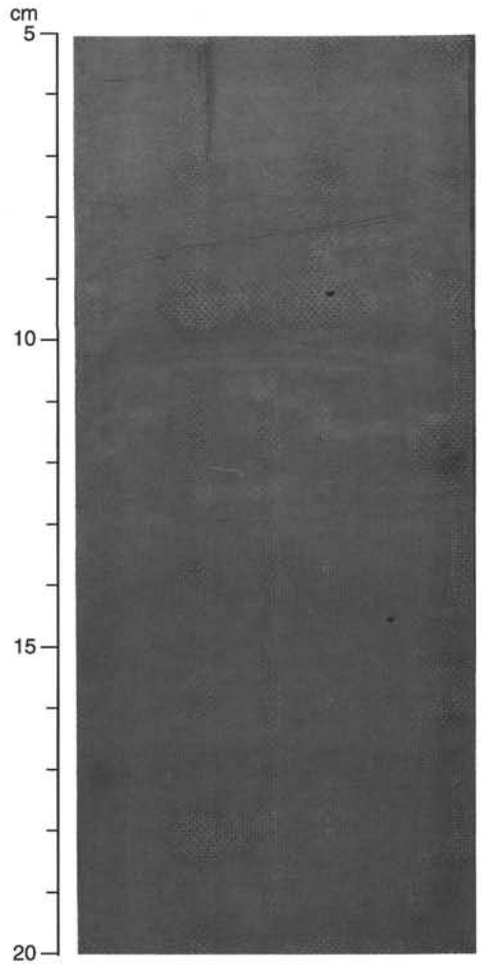

Figure 9. Detail of the complex structure and gradational nature of the oxidation front in an organic-rich turbidite. Interval 157-950A-10H-7, 5–20 cm. Compare to Figure 10.

tional with underlying units. Above 100 mbsf, the calcium carbonate content of these beds is variable (Fig. 7) and the sediments vary in composition from clays to nannofossil oozes. The composition of the pelagic sediments in the upper part of Unit I reflects changes in the depth of the calcite compensation depth (Gardner, 1975; Crowley, 1983; Weaver and Kuijpers, 1983).

Between 100–150 mbsf, the calcium carbonate content of the pelagic interbeds decreases sharply, although individual beds still show some variability (Fig. 7). Below 150 mbsf, pelagic interbeds are consistently clays and generally contain less than 10% calcium carbonate. This increase in clay content of the pelagic interbeds was taken to distinguish Subunit Ia, whose upper boundary was fixed at 150 mbsf.

Tephra

Although volcanic glass shards are present in some turbidite bases, only one ash-fall layer was identified within Unit I: a thin (0.5 cm thick) brown layer within a medium-bedded interval of clayey nannofossil mixed sediment at core interval 157-950A-1H-3, 40.5–41 cm (Fig. 15).

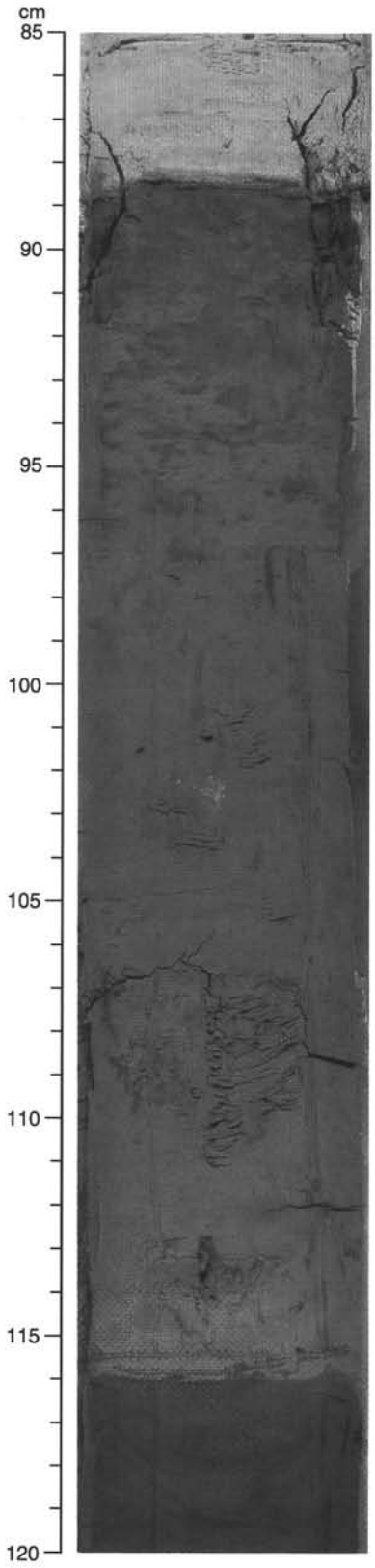

Figure 10. Bioturbated oxidized top of an organic-rich turbidite from Subunit 1b. Note the abrupt color transition at 116 cm caused by an oxidation front. Interval 157-950A-24X-6, 85–120 cm.

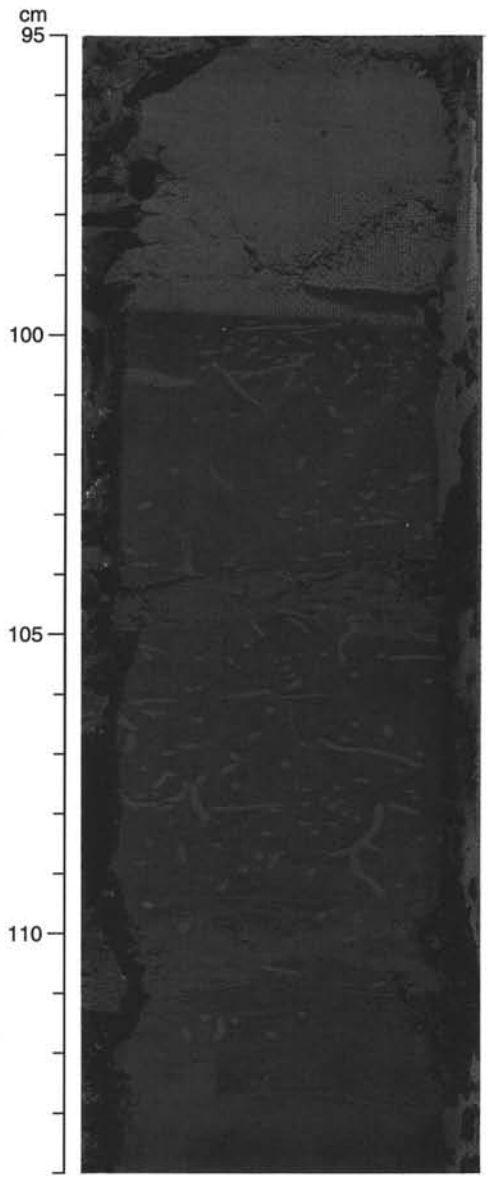

Figure 11. Penetration of burrows beyond the oxidation front into the reduced lower part of an organic-rich turbidite. Interval 157-950A-32X-2, 95–114 cm.

Unit II

Interval: Sections 157-950A-34X-2 to the top of 37X-1
Depth: 305.6–333 mbsf

Unit II is an interval of very poor core recovery within which some sections of calcarenite have been recovered. The downhole logs clearly show three coarse-grained units in this interval, and we have used this data to establish the base of the unit at the base of the non-recovered interval (top of Core 37X). The thickest unit recovered consists of a 1.1-m-thick interval of massive calcarenite. This distinctive bed consists of semiconsolidated to unconsolidated structureless muddy calcareous silty sand containing sand-size carbonate grains mixed with volcaniclastic debris (Figs. 16 and 17). The bed also contains granule- to pebble-size clasts of greenish gray clay up to 3 cm in diameter. Examination of the carbonate-free sand-size fraction shows that the volcaniclastic fraction consists dominantly of fine-

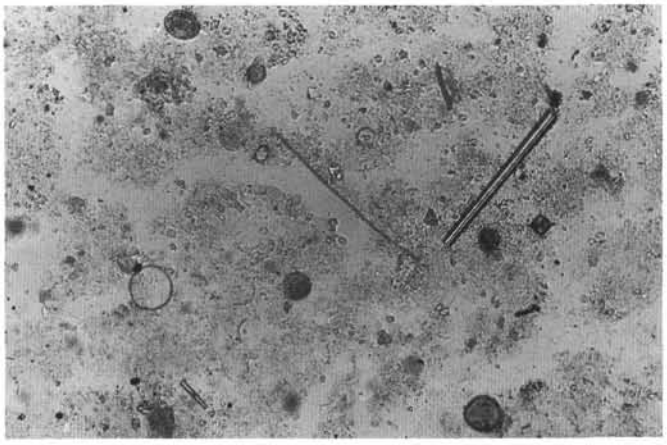

Figure 12. Photomicrograph of smear slide from an organic-rich turbidite mud showing common siliceous microfossils. These are very rare or absent from organic-rich turbidites from below 100 mbsf. Field of view is 1.5 mm wide. Sample 157-950A-2H-3, 27 cm.

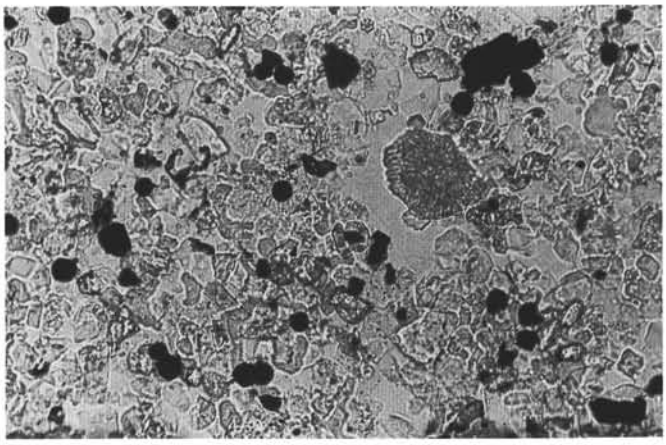

Figure 13. Photomicrograph of smear slide from an organic-rich turbidite mud showing common framboidal pyrite. These probably formed within microfossil tests, which have since dissolved. Field of view is 0.6 mm wide. Sample 157-950A-29X-1, 94 cm.

grained fragments of zeolitic vitric tuff (60%), basaltic rock fragments (mostly tachylite, 15%–20%), individual glass shards (2%), and crystals of alkali feldspar, minor plagioclase, alkali amphibole, clinopyroxene, hornblende, and aegirine. Felsic rock fragments, such as trachytes, phonolites, or rhyolites are rare. Some rounded fragments of felsic tuff occur as rounded pebbles. Many are completely zeolitized while others contain glass shards.

The relative proportion of mafic and felsic shards is difficult to determine because of the alteration to clay and zeolites. However, some clear vesicular glass shards appear relatively unaltered and suggest that evolved compositions are represented. Other glass shards exhibit various degrees of palagonization and are most likely of more mafic composition. Individual crystals are generally subhedral and range up to a millimeter in size. Plagioclase is more abundant than alkali feldspar while clinopyroxene is the third most abundant mineral phase. Pale brown to greenish alkali amphibole (edenite or richterite) occurs rarely along with hornblende. Biotite is present in minor amounts.

This neritic sediment is strongly reminiscent of calcareous beach sand. The apparent freshness of some volcanic material suggests that

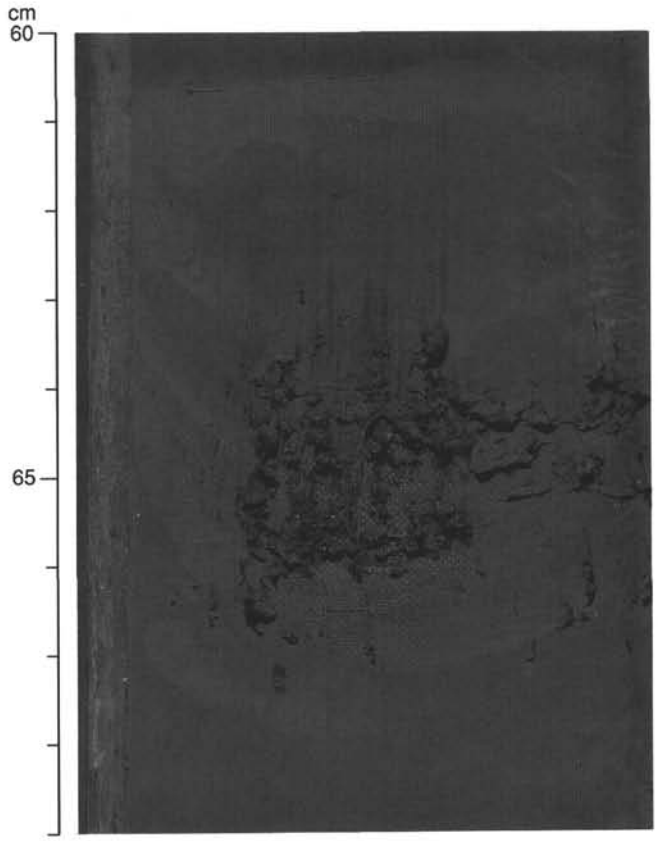

Figure 14. Cluster of framboidal pyrite suspended within Te division turbidite mud. This is an unusually large concentration and may reflect a cluster of fecal pellets that originally contained foraminifers and/or other microfossils that have since dissolved. Sample 157-950A-24X-1, 60–69 cm.

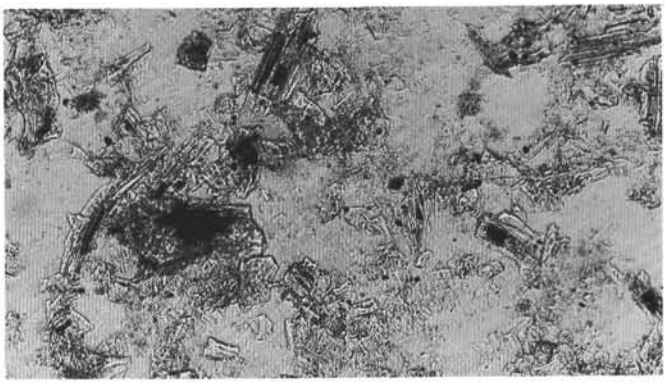

Figure 15. Photomicrograph of smear slide from tephra layer within a pelagic clayey nannofossil mixed sediment. Field of view is 1.5 mm wide. Sample 157-950A-1H-3, 40 cm.

the time between its eruption and incorporation into the sand was relatively short.

Unit III

Interval: Sections 157-950A-37X-1 through 40X-3
Depth: 333–370 mbsf

Unit III consists of a sequence of firm, medium to very thickly bedded, light orange-brown to dark reddish-brown, commonly mot-

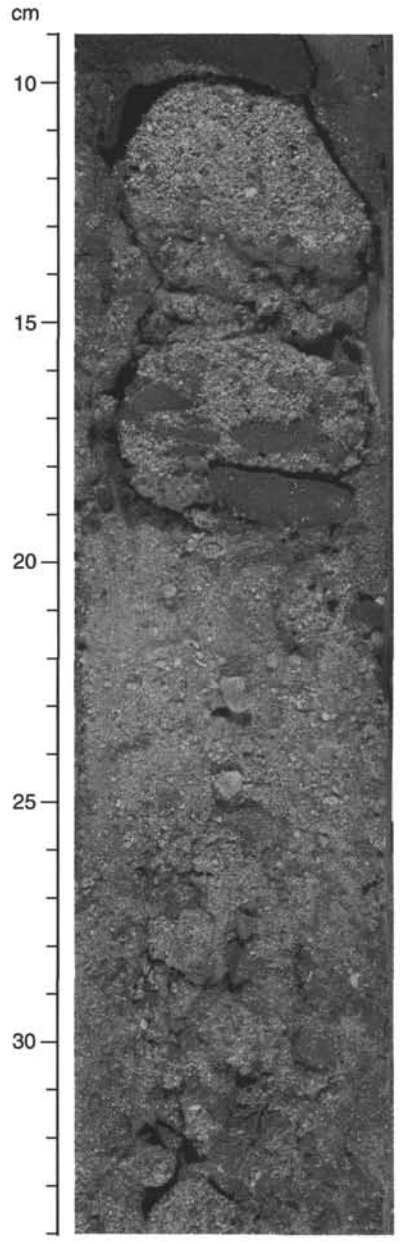

Figure 16. Part of the interval of massive calcarenite that forms Unit II. This distinctive bed consists of semiconsolidated to unconsolidated structureless muddy calcareous silty sand containing sand-sized carbonate grains mixed with igneous crystals, volcanic glass shards, and basic igneous rock fragments. This neritic sediment is strongly reminiscent of calcareous beach sand. Interval 157-950A-35X-1, 9–34 cm.

tled, clay (red clay) containing medium to thin interbeds of pale brown clay, clayey nannofossil mixed sediment, and clayey nannofossil chalk, and thin partly zeolitic and completely zeolitized volcanic ash layers.

Red Clay

The dominant lithology in Unit III is very firm, medium to very thickly bedded, light orange-brown to dark reddish-brown clay. This clay is mottled, with large oval to circular patches (up to 5 cm across) that are probably of diagenetic origin. Over some intervals, slight to moderate bioturbation is visible, while in other intervals bioturbation cannot be seen. The calcium carbonate content of the clay is negligible (Fig. 18). The red clay is interpreted as representing slow pelagic accumulation.

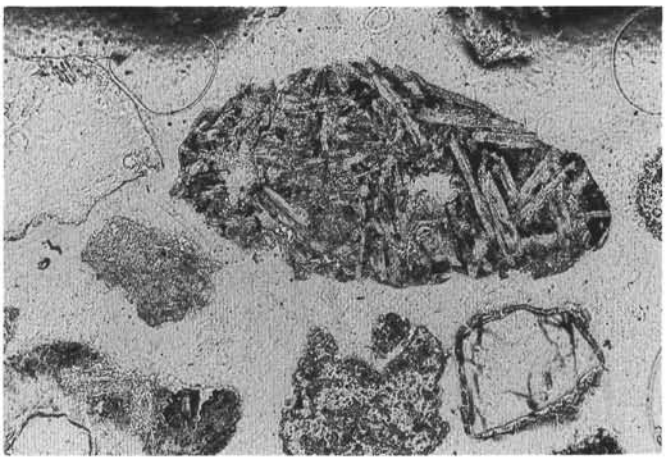

Figure 17. Photomicrograph of a grain mount showing a rounded plagioclase-phyric basalt grain from the massive calcarenite that forms Unit II. Field of view is 150 µm. The groundmass of the basalt contains dendrites of opaque oxide and feldspar(?) together with altered glass. These features are indicative of rapid cooling such as occurs during submarine eruption of basaltic lava. Shown in the lower right is an alkali feldspar crystal mantled by an alteration rind of fine-grained clay. A zeolitized fragment of tuff is shown at bottom center. The presence of these fragments indicates a source area that produced both felsic and basaltic magmas. Field of view is 2.4 mm wide.

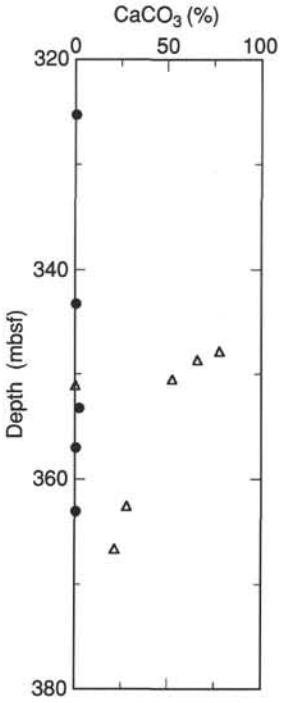

Figure 18. Downcore calcium carbonate plot through Unit III. Filled circles = red clay (interpreted as pelagic); open triangles = thin pale brown nannofossil clay interbeds (interpreted as turbidites).

Pale Brown Nannofossil Clay, Clayey Nannofossil Mixed Sediment, and Clayey Nannofossil Chalk Interbeds

Within the red clay are numerous discrete medium- to thinly-bedded interbeds of pale brown nannofossil clay, clayey nannofossil

mixed sediments, and clayey nannofossil chalk. These typically range from 5 to 20 cm in thickness and characteristically show burrowed upper contacts and straight lower contacts. The upper part of these units typically shows moderate bioturbation and commonly the lower part consists of parallel- and cross-laminated siltstone (Figs. 19 and 20). These units are interpreted as turbidites on their textural characteristics and bed organization. Their calcium carbonate content varies widely from almost zero to 80% $CaCO_3$ (Fig. 18).

Zeolitic Ash Layers

Thin discrete zeolitic and completely zeolitized ash bands occur throughout Unit III, particularly in Core 37X and the lower part of Core 39X (Fig. 21). Zeolites sometimes occur as thin almost monominergic bands within the sediments. Their crystal form varies from euhedral prismatic crystals and radiating clusters and rosettes (Fig. 22) to sub- to anhedral platy crystals and small ragged shreds (Fig. 23). In many of the zeolitic ash bands, the zeolites are mixed with brown clay.

Unit IV

Interval: Sections 157-950A-40X-3 through 41X-CC
Depth: 370–381 mbsf

Unit IV consists of 4.15 m of dark olive green volcaniclastic siltstone and fine-grained sandstone and dark olive green homogeneous clay and represents the deepest sediments cored at Site 950. The volcaniclastic silt- and fine-grained sandstone form two distinct depositional units separated by 37 cm of dark olive green homogeneous clay. The upper parts of both silt and sandstone units consists of pale greenish-gray, moderately bioturbated nannofossil clay with burrowed upper contacts. These grade downcore into silty clay mixed sediment and then planar laminated volcaniclastic silts, tabular, and trough cross-laminated sandy siltstone, and then to graded laminated very fine to fine-grained sandstones in the upper unit. The basal contact of the upper unit is sharp and straight. In the lower unit, the pale greenish-gray nannofossil clay grades downcore into a parallel- and cross-laminated volcanic siltstone (Fig. 24), which grades down into massive, very dark greenish gray, fine-grained volcaniclastic sandstone. From their internal structure and bed characteristics, both silt and sandstone can be identified as proximal volcaniclastic turbidites.

The units are composed of 100–600 µm grains that consist of basaltic rock fragments, mostly tachylite but with some more crystalline varieties (10%–15%), vesicular glass shards of mafic and felsic composition (20%), zeolitic vitric tuff (15%) and felsic rock fragments, 10% biogenic material (foraminifers and shell fragments), and 30%–40% pore space. Individual crystals are usually fresh and up to 2 mm in size. In general, alkali feldspar dominates over plagioclase, with clinopyroxene forming the next most abundant phase. Most glass shards are completely altered to clay and zeolites, mainly phillipsite.

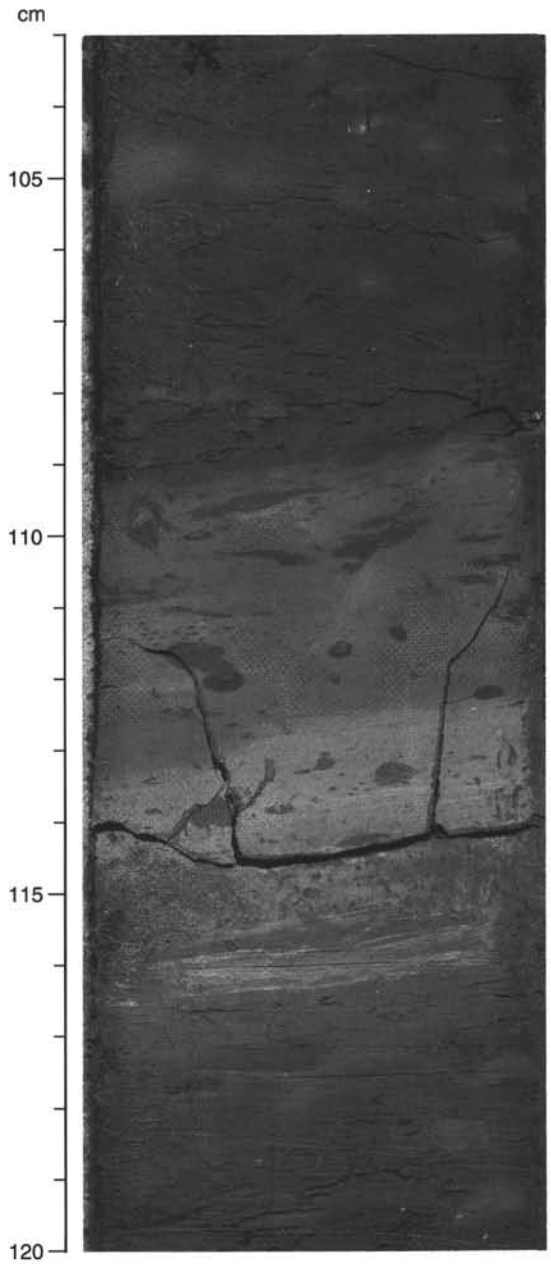

Figure 19. Thin nannofossil clay turbidite within the pelagic red clay of Unit III. Note the bioturbated upper part of the turbidite and the laminated silty base. Note also the diagenetic mottling of the enclosing red clay. Interval 157-950A-38X-3, 103–120 cm.

Depositional History

Unit IV, the deepest sediments cored at Site 950, represents two proximal volcaniclastic turbidites derived from a nearby volcanic island or seamount. The particles contained in these units indicate that they formed from both explosive and effusive volcanism. However, the polymict nature of the units suggests that they are epiclastic, being derived from the erosion of pre-existing volcanic and volcaniclastic rocks. The vesicular nature of the altered vitric tuffs and the occurrence of oxidized scoria fragments suggests that some of the source volcanism was subaerial, while the presence of tachylitic grains is indicative of shallow water marine eruptions.

The coarse-grained nature of the volcaniclastic material suggests its source is likely to have been one or more of the large seamounts west of Site 950 (Meteor-Cruiser Seamount chain). By this time the islands had already produced a significant volume of felsic magma, as indicated by the presence of vitric tuff fragments in the deposit. Shipboard biostratigraphic dating indicates a maximum age of early Eocene for these turbidites, which is in broad agreement with the age of basalts dredged from Great Meteor Seamount (Wendt et al., 1976). These volcaniclastic turbidites probably reached their present position by emplacement through the Cruiser Fracture Zone Valley, which enters the Madeira Abyssal Plain west of the drill site. The Great Meteor Seamount lies about 300 km southwest of Site 950 and the Cruiser Seamount about 250 km northwest of it. The seamounts are flat-topped, and currently the central and southern seamounts are

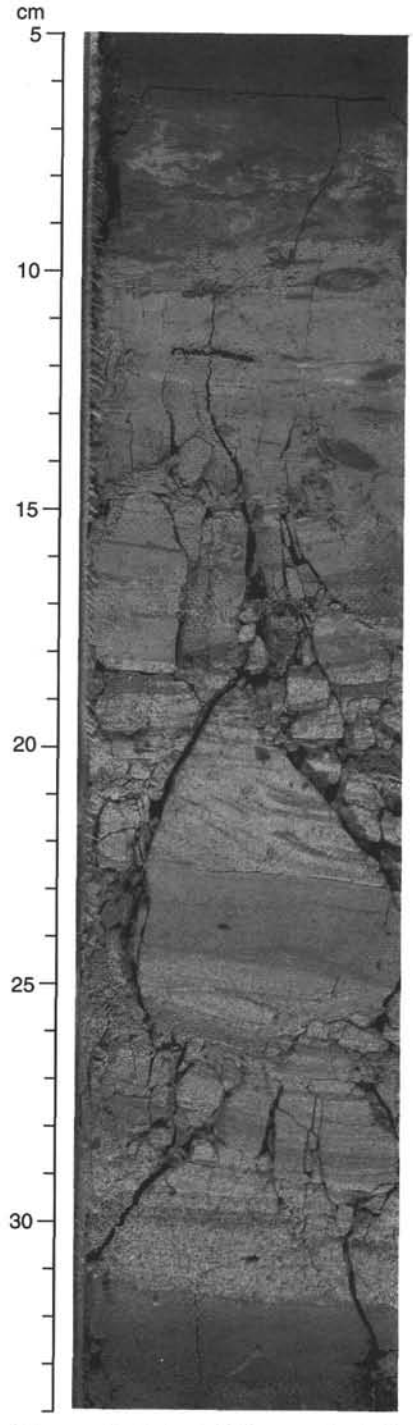

Figure 20. Two thin nannofossil clay turbidites emplaced directly on top of one another within the pelagic red clay of Unit III. Note the coarse-grained silty bases of both turbidites and the cross-lamination within the base of the upper turbidite. Interval 157-950A-37X-5, 5–34 cm.

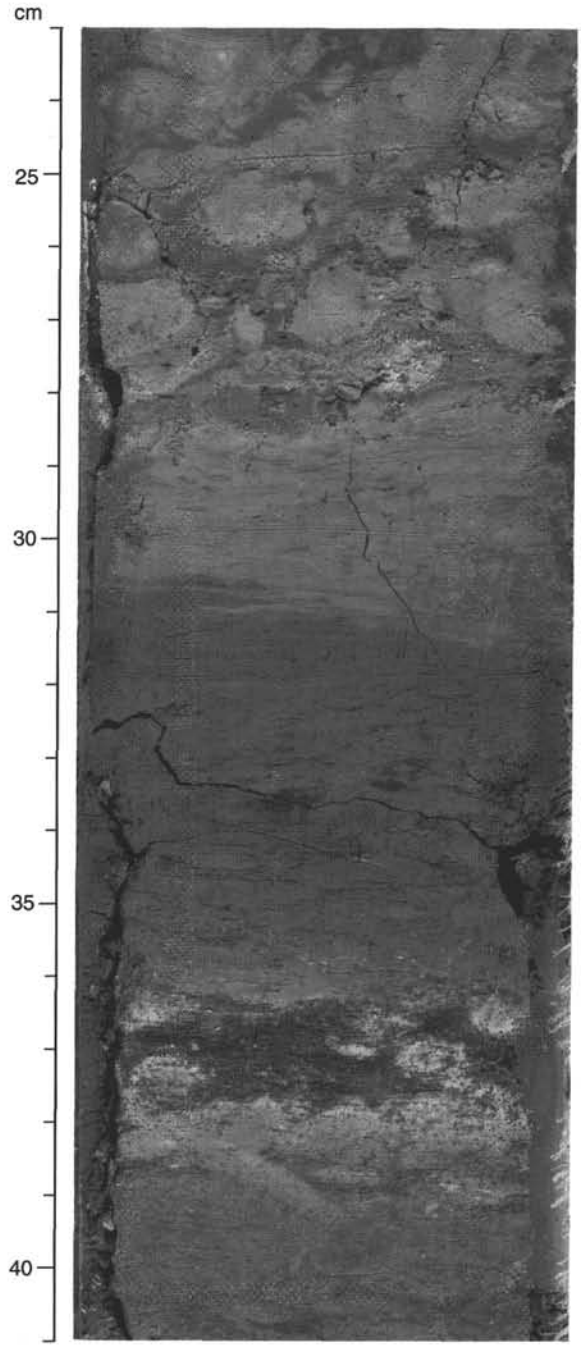

Figure 21. Zeolitic ash bands within the pelagic red clay of lithologic Unit III. The upper band at 28 cm is almost monomineralic containing large, well-formed prismatic phillipsite crystals, rosettes, and radiating clusters (see Fig. 22). The darker band at 37.5 cm contains small subhedral and shredded zeolite crystals mixed with brown clay. Interval 157-950A-37X-6, 23–41 cm.

at a depth of <300 m, indicating that they were once subaerial but were eroded and subsequently sank.

Deposition during Unit III at Site 950 was essentially pelagic with the deposition of red clay below the CCD. Numerous zeolitic ash-fall layers within this sequence testify to the relative proximity of active explosive volcanism. The source of these tephra layers is likely to be to the west from felsic explosive volcanism occurring on a subaerial island or islands of the Great Meteor-Cruiser volcanic chain. Sporadic influx of nannofossil clay turbidites at this time are further possible indications of instability on local high ground, perhaps related to seismic activity. These turbidites also contain some volcaniclastic silt and sand. In addition, the clay fraction may consist largely of smectite, indicated by the expansion of cores after recovery. This suggests a large component of volcanic precursor such as basaltic glass. Sedimentation rate estimations (see "Sediment Accumulation Rates," this

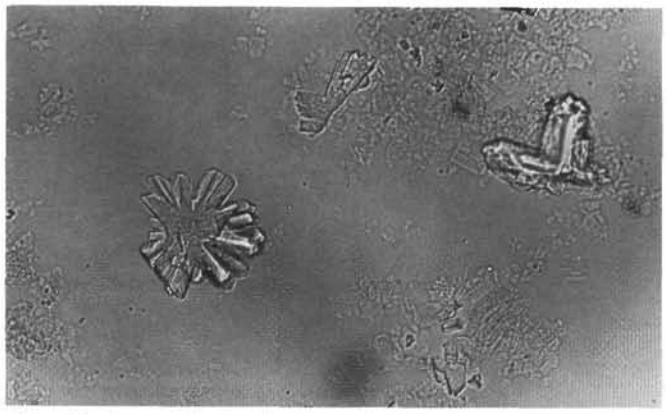

Figure 22. Smear slide showing euhedral phillipsite radiating clusters and rosettes from a zeolitized ash band in Unit III. Field of view is 0.6 mm wide. Sample 157-950A-37X-6, 27 cm.

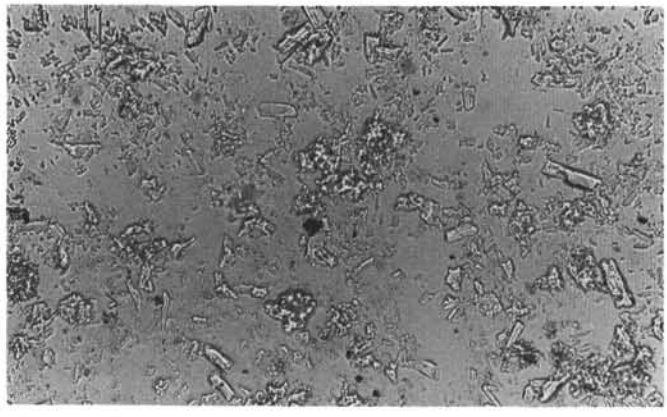

Figure 23. Smear slide showing sub- to anhedral platy crystals and small ragged shreds of zeolite from a zeolitized ash band in lithologic Unit III. Field of view is 0.6 mm wide. Sample 157-950A-37X-3, 67 cm.

chapter) suggest that this episode of red clay deposition lasted for 15 m.y.

Deposition of calcareous sands containing fresh and altered volcaniclastics (Unit II) around 13–15 Ma (see "Sediment Accumulation Rates" chapter), suggests emplacement of sediments derived from a shallow-water near-shore environment, probably the upper flank of the Cruiser/Hyères/Great Meteor seamount complex, which may have been emergent at that time.The calcareous sands of Unit II may represent debris flow deposits. After this unit was emplaced, the amount of coarse volcaniclastic material reaching the site diminished rapidly.

During the middle Miocene, a remarkable change in sedimentation pattern occurred with the sudden influx of fine-grained distal volcanic-rich, organic-rich, and calcareous turbidites, deposition of which has continued unabated to the present. The calcareous turbidites appear to have been derived from instability on the flanks of seamounts to the west, while the organic-rich turbidites have their origin beneath upwelling cells on the northwest African continental margin. The volcaniclastic turbidites are also highly distal in character and are probably derived from the oceanic islands of the Canaries and Madeira. Emplacement of turbidites from the different sources appears to have been random over time. However, organic-rich turbidites make up the great proportion of the allochthonous sediments, with volcanic-rich turbidites as the second most common sediment type.

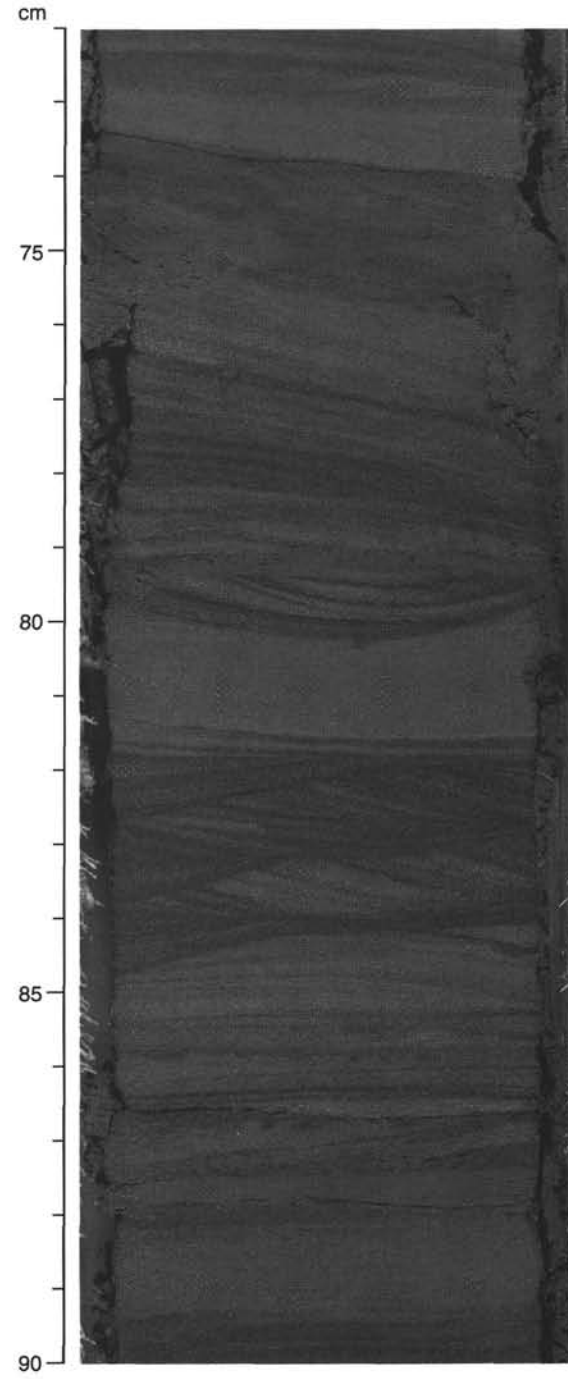

Figure 24. Parallel- and cross-laminated volcaniclastic coarse-grained siltstone in Unit VI, representing part of a proximal volcaniclastic turbidite. Sample 157-950A-40X-4, 72–90 cm.

BIOSTRATIGRAPHY

Introduction

The quality of calcareous microfossil biostratigraphy at Site 950 depends on carbonate preservation. In lithologic Unit I, the carbonate content of hemipelagic sediments is high from the surface to 85 mbsf but declines to trace amounts below 150 mbsf where carbonate content is above trace levels only in calcareous turbidites. The top of this

interval near 85 mbsf corresponds to the onset of Northern Hemisphere glaciation and late Pliocene deepening of the CCD. Sampling is affected by the pattern of carbonate preservation. All foraminifer samples below about 140 mbsf come from turbidites, and many nannofossil samples below about 240 mbsf come from turbidites. The unconsolidated calcarenite of lithologic Unit II is barren of planktonic foraminifers and nannofossils. The brown clays and zeolitic volcanic ashes in lithologic Unit III are barren and recovery of both nannofossils and foraminifers comes from selected turbidites. A few nannofossils were recovered from the volcanic turbidites of lithologic Unit IV, but the unit is barren of foraminifers. In general, the best biostratigraphic resolution is in the upper and middle portions of lithologic Unit I with poor resolution in lithologic Unit III.

The nannofossils and foraminiferal zones agree within the resolution of the sampling. Figure 25 shows the foraminifer and nannofossil zonal interpretation for Site 950. Only one problem interval appears in the middle to lower Miocene. Foraminiferal Zone M13/M12 and M11 co-occur with the older nannofossil Zones CN7 and CN5, suggesting that the nannofossils may be reworked in this part of the section. Additional shore-based work may resolve this problem.

The determination of the depth of the Pleistocene/Pliocene and the Pliocene/Miocene boundaries in Hole 950A was accomplished by integrating the foraminiferal and nannofossil information. The Pliocene/Pleistocene boundary between 79.10 and 76.17 mbsf in Hole 950A is based on the last occurrence of the Pliocene nannofossil *Discoaster brouweri* in Sample 157-950A-9H-3, 70 cm (79.10 mbsf), and the first occurrence of the Pleistocene foraminifer *Globorotalia truncatulinoides* in Sample 157-950A-9H-1, 77–79 cm (76.17 mbsf). The Pliocene/Miocene boundary is not as precisely determined, but it appears to be between 200.26 and 216.58 mbsf. Sample 157-950A-23X-2, 96–98 cm (200.26 mbsf), contains *Globorotalia margaritae,* sinistral *Neogloboquadrina acostaensis,* and *Globigerina nepenthes* without *Globorotalia juanai,* while Sample 157-950A-24X-7, 8 cm (216.58 mbsf), has the Miocene nannofossil *Discoaster quinqueramus.* A sample at 215.81 mbsf is not assignable to either the early Pliocene or the late Miocene because it contains few and poorly preserved foraminifers, and *Globorotalia juanai* could be excluded from the assemblage because of dissolution or small sample size.

Calcareous Nannofossils

Shipboard analysis of core-catcher samples for nannofossils proved ineffectual for Site 950. The high abundance of turbidites meant that the core catcher usually sampled turbidites rather than hemipelagic sediments. The first two core-catcher samples were examined, but this procedure was quickly abandoned and the succeeding cores were sampled for nannofossils after they had been split and the appropriate hemipelagic lithologies identified. There was relatively good recovery of autochthonous nannofossils (Table 2) down to Sample 157-950A-27X-6, 132.5 cm (245.33 mbsf). Below this point nannofossil preservation deteriorated markedly. The brown hemipelagic clays between the turbidites were often barren of nannofossils, indicating this area was below the CCD at their time of deposition. Below Sample 157-950A-31X-1, 69 cm, the brown hemipelagic clays were consistently barren of nannofossils, and, therefore, the carbonate turbidites were examined (Table 2).

By using the youngest possible age, based on first appearance datum (FAD) levels of species in the turbidites, maximum ages for the deposition of the hemipelagic sediments can be derived. The tops of species ranges observed here are suspect because of the possibility of reworking. Even thin hemipelagic clays can contain reworked material due to bioturbation with underlying turbidites. Reworking is clearly demonstrated in the Pleistocene hemipelagic section and probably also occurs in the older hemipelagic sediments as well.

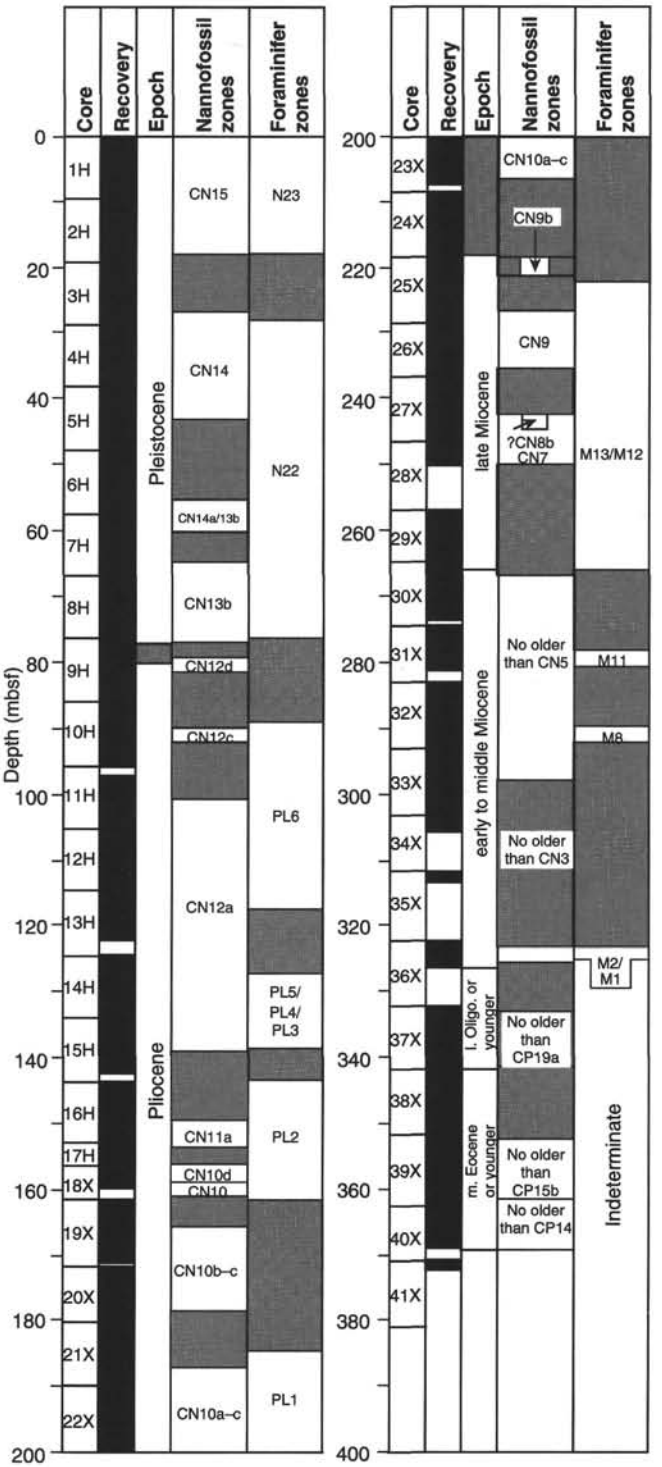

Figure 25. Comparison of stratigraphic extent of nannofossil and foraminiferal zones in Hole 950A.

Pleistocene

Well-preserved and abundant (Table 2) Pleistocene nannofossils were recovered from Cores 1H to 8H. *Emiliania huxleyi* was present down to Core 2H-7, 20.5 cm, indicating Zone CN15 (Fig. 25). Within CN15 rare specimens of the marker for the top of the underlying Zone

Table 2. Abundance, preservation, zone, and lithology of samples used in nannofossil zonation.

Core, section, interval (cm)	Depth (mbsf)	Abundance	Preservation	Zone	Lithology
157-950A-					
0-0, 0–0	0.00			CN15	Turbidite *b*
1H-6, 110–110	8.60	VH	M	CN15	Hemipelagic marl
2H-6, 107–107	17.47	VH	M	CN15	Hemipelagic marl
2H-7, 20.5–20.5	18.11	H	G	CN15	Hemipelagic marl
3H-7, 78–78	26.98	H	M	CN14a	Hemipelagic marl
3H-CC, 11–11	27.81	L	M	CN14a	Turbidite R sand
4H-6, 110.5–110.5	36.51	H	M	CN14a	Hemipelagic marl
4H-CC, 12–12	37.52	H	G	CN14a	Hemipelagic ooze
5H-4, 113–113	43.03	VH	G	CN14a	Hemipelagic ooze
5H-5, 2–2	43.42	VH	G	CN14a	Hemipelagic clay
6H-6, 90–90	55.00	VH	M	CN13b, lowermost 14a	Hemipelagic ooze
6H-6, 132.5–132.5	55.43	H	M	CN13b, lowermost 14a	Hemipelagic ooze
7H-6, 128–128	65.18	H	G	CN13b	Hemipelagic ooze
7H-CC, 4–4	66.17	H	G	CN13b	Hemipelagic marl
8H-6, 109–109	74.49	G	VG	CN13b	Hemipelagic ooze
9H-3, 70–70	79.10	VH	G	CN12d	Hemipelagic ooze
9H-6, 12–12	83.02	VH	G	CN12d	Hemipelagic marl
10H-5, 59–59	90.09	VH	G	CN12c	Hemipelagic ooze
10H-6, 17–17	91.17	VH	G	CN12c	Hemipelagic ooze
11H-5, 96–96	101.36	VH	M	CN12a	Hemipelagic marl
11H-6, 78–78	102.68	M	G	CN12a	Hemipelagic clay
11H-7, 42–42	103.82	H	G	CN12a	Hemipelagic marl
12H-6, 38–38	111.78	H	M	CN12a	Hemipelagic clay
13H-5, 16–16	119.56	H	M	CN12a	Calcareous turbidite
14H-2, 68–68	125.08	H	M	CN12a	Hemipelagic clay
14H-4, 104–104	128.44	H	G	CN12a	Hemipelagic clay
15H-5, 130–130	139.70	M	M	CN12a	Hemipelagic clay
16H-6, 80–80	150.20	M	M	CN11a	Hemipelagic clay
17H-2, 70–70	151.10	L	M	CN11a	Hemipelagic clay
17H-4, 21–21	154.58	M	M	CN11a	Hemipelagic clay
18X-2, 133.5–133.5	157.24	M	M	CN10d	Hemipelagic clay
18X-CC, 49–49	158.36	VL	P	CN10	Hemipelagic clay
19X-5, 99–99	167.23	L	M	CN10b–c	Hemipelagic clay
19X-6, 71–71	168.51	M	M	CN10b–c	Hemipelagic clay
20X-CC, 33–33	179.63	H	M	CN10b–c	Hemipelagic clay
21X-CC, 22–22	188.23	M	M	CN10a–c	Hemipelagic clay
22X-4, 53–53	193.23	L	M	CN10a–c	Hemipelagic clay
23X-6, 10–10	205.40	H	MG	CN10a–c	Hemipelagic clay
24X-2, 98–98	209.98	B		Barren	Hemipelagic clay
24X-6, 117.5–117.5	216.18	B		Barren	Hemipelagic clay
24X-7, 8–8	216.58	H	M	CN9b	Hemipelagic clay
25X-4, 133–133	223.03	B		Barren	Hemipelagic clay
25X-6, 97–97	225.67	L	P	CN9	Hemipelagic clay
25X-CC, 2–2	226.22	B		Barren	Hemipelagic clay
26X-5, 95.5–95.5	233.76	M	M	CN9	Hemipelagic clay
26X-6, 64.5–64.5	234.95	L	M	CN9	Hemipelagic clay
27X-4, 70–70	241.70	M	M	CN8b?	Brown turbidite
27X-6, 47–47	244.47	M	G	Upper CN7	Gray turbidite
27X-6, 132.5–132.5	245.33	B		Barren	Green turbidite
28X-2, 36–36	247.96	B		Barren	Green turbidite
28X-3, 23.5–23.5	249.34	B		Barren	Hemipelagic clay
28X-3, 33.5–33.5	249.44	B		Barren	Turbidite?
28X-3, 36–36	249.46	M	M	CN7	Dark green turbidite
29X-7, 14–14	264.84	B		Barren	Hemipelagic clay
29X-CC, 34.5–34.5	265.20	VL	P	CN5	Hemipelagic clay
30X-5, 85–85	272.25	VH	M	No older than CN5	Hemipelagic clay
30X-6, 30.5–30.5	273.21	L	P	CN5	Hemipelagic clay
31X-1, 69–69	275.79	B		Barren	Hemipelagic clay
31X-2, 59–59	277.19	B		Barren	Green/brown turbidite
31X-5, 56–56	281.66	VH	M	No older than CN5	Calcareous turbidite
32X-5, 132.5–132.5	292.13	B		Barren	Hemipelagic clay
32X-6, 19–19	292.49	VH	P-M	No older than CN5	Calcareous turbidite
32X-6, 121.5–121.5	293.52	B		Barren	Hemipelagic clay
33X-2, 89–89	296.79	M	M	No older than CN5	Gray turbidite
33X-6, 37.5–37.5	302.28	B		Barren	Hemipelagic clay
33X-7, 40–40	303.80	B		Barren	Hemipelagic clay
34X-1, 126–126	305.36	B		Barren	Hemipelagic clay
34X-2, 50.5–50.5	306.11	H	M	No older than CN3	Calcareous turbidite
36X-2, 57–57	325.37	VL	P	Probably CN5	Hemipelagic clay
37X-6, 86–86	341.36	B		Barren	Massive clay
37X-6, 120–120	341.70	VH	G	No older than CP19a	Laminated silt
38X-6, 49–49	350.59	VH	G	No older than CP15b	Brown clay
38X-CC, 36–36	352.41	B		Barren	Brown clay
38X-CC, 42–42	352.47	H	M	No older than CP15b	Brown clay
39X-6, 140–140	361.20	M	M	No older than CP15b	Brown clay
39X-6, 145–145	361.25	H	G	No older than CP14	Brown clay
39X-CC, 3–3	361.80	B		Barren	Brown clay
40X-3, 17.5–17.5	365.18	B		Barren	Clay
40X-3, 130–130	366.30	M	M	No older than CP14	Clay
40X-4, 17–17	366.67	H	G	No older than CP14	Clay
40X-CC, 5–5	367.79	VL	P	No older than CP14	Volcaniclastic sandstone
41X-1, 25–25	371.85	B		Barren	Volcaniclastic sandstone

Note: Key to abbreviations for abundance and preservation in "Explanatory Notes" (this volume).

CN14a, *Pseudoemiliania lacunosa,* were interpreted as reworked. The abundant occurrence of *P. lacunosa* in Sample 157-950A-3H-7, 78 cm, was used as the top of Zone CN14a. In Sample 157-950A-4H-CC, 12 cm, the top of *Reticulofenestra asanoi* marked the lowermost part of Zone CN14a, and its base in Sample 157-950A-5H-5, 2 cm, was taken to approximate the base of Zone CN14a. The base of *Gephyrocapsa caribbeanica* in Sample 157-950A-8H-6, 109 cm, marked the base of Zone CN13a. Reworked Pliocene–Miocene marker species, such as *Discoaster brouweri, D. pentaradiatus,* and *Reticulofenestra pseudoumbilicus* were found in low numbers throughout the Pleistocene samples.

Pliocene

The highest consistently occurring *Discoaster brouweri* was in Sample 157-950-9H-3, 70 cm, and marks the top of Zone CN12d (Fig. 25). Below this, in Sample 157-950A-10H-5, 59 cm, the highest consistent *D. pentaradiatus* indicates the top of Zone CN12c, and the top of consistent *D. tamalis* in Sample 157-950A-11H-5, 96 cm, indicates Zone CN12a. *D. surculus* also has its first downhole occurrence here. The base of common *D. tamalis* in the absence of *Reticulofenestra pseudoumbilicus* indicates the base of Zone CN12a in Sample 157-950A-15H-5, 130 cm. The top of persistently occurring *R. pseudoumbilicus* larger than 7 µm in diameter and *Sphenolithus* spp. were used to indicate the top of Zone CN11a at Sample 157-950A-16H-6, 80 cm. Occurrences of *R. pseudoumbilicus* above this are considered reworked. Zone CN11b was not observed. The top of *Amaurolithus delicatus* and the base of common *Discoaster asymmetricus* occur together in Sample 157-950A-18X-2, 133.5 cm, and indicate Zone CN10d. A single specimen of *Ceratolithus acutus* was observed in Sample 157-950A-20X-CC, 33 cm; therefore, this sample and those above it up to the base of CN10d must belong to Zones CN10b to CN10c. Since *C. acutus* was rare at this site, its absence below this sample was not used as an indication of CN10a, but a broader age call of CN10a to CN10c was used for samples down to Sample 157-950A-23X-6, 10 cm. Below this level the preservation and abundances of nannofossils in hemipelagic sediments drops off markedly.

Miocene

The first barren hemipelagic samples (Table 2) occur in Sample 157-950A-24X-2, 98 cm (209.98 mbsf), and Sample 157-950A-24X-6, 110.5 cm (216.18 mbsf). Sample 157-950A-24X-7, 8 cm, contains a low abundance, moderately preserved assemblage which contains *Discoaster quinqueramus* and a single specimen of *Amaurolithus amplificus,* indicating Zone CN9b of late Miocene age (Fig. 25). The base of *Discoaster berggrenii* was used to indicate the base of CN9 in Sample 157-950A-26X-6, 64.5 cm (234.95 mbsf). Sample 157-950A-27X-4, 70 cm, has a moderately abundant, moderately preserved assemblage that lacks *Discoaster quinqueramus* or *D. berggrenii,* and also lacks *Discoaster hamatus,* the marker for the underlying Zone CN7. This sample also contains rare specimens of a discoaster that closely resembles *D. loeblichii,* whose base marks CN8b. Accordingly, this sample is tentatively assigned to CN8b. The underlying sample, Sample 157-950A-27X-6, 47 cm, has a moderately abundant, well-preserved assemblage that contains the marker for Zone CN7, *Discoaster hamatus.* Below this, Samples 157-950A-27X-6, 132.5 cm, to 157-950A-28X-3, 33.5 cm, are barren. Sample 157-950A-28X-3, 36 cm, has a rare occurrence of *D. hamatus,* and so belongs to CN7.

Age control below 245.3 mbsf (Sample 157-950A-27X-6, 132.5 cm) deteriorates markedly, as most of the underlying hemipelagic samples are either barren or have very low abundances (Table 2). Samples 157-950A-29-CC, 34.5 cm, and 157-950A-30X-6, 30.5 cm (265.20 and 273.21 mbsf), contain a very low abundance assemblage of *Cyclicargolithus floridanus,* as well as rare *Reticulofenestra pseudoumbilicus* (larger than 7 µm). Together these species indicate Zone CN5a and the lower part of Zone CN5b (Fig. 25). This is a tentative assignment to CN5. The age may be significantly younger since the first evolutionary appearance of *R. pseudoumbilicus* is a difficult event to determine precisely with widely spaced sampling intervals and poorly preserved material, and the last appearance of *C. floridanus* is subject to reworking. A calcareous turbidite at Sample 157-950A-30X-5, 85 cm, contains abundant *R. pseudoumbilicus,* suggesting that the sample is no older than CN5.

Hemipelagic samples are barren below this sample (Table 2) down to Sample 157-950A-36X-2, 57 cm, which contains a similar assemblage and is similarly tentatively assigned to CN5 (Fig. 25). Calcareous turbidite units were sampled below this (Samples 157-950A-31X, 56 cm, 157-950A-32X-6, 19 cm, 157-950A-33X-2, 89 cm, and 157-950A-34X-2, 50.5 cm) and contained high abundance, moderately preserved assemblages. The first three samples all contain *Reticulofenestra pseudoumbilicus,* larger than 7 µm, and are tentatively considered to be no older than Zone CN5. The fourth sample contains *Sphenolithus heteromorphus* without *R. pseudoumbilicus* and is no older than Zone CN3. A hemipelagic clay in Sample 157-950A-36X-2, 57 cm, contains very rare *Cyclicargolithus floridanus* and *R. pseudoumbilicus* and may belong to CN5; however, this assignment is very tentative. The abundances are so low that either laboratory or core contamination may be at fault. Below this sample, all hemipelagic samples were barren except for a single occurrence of *Dictyococcites bisecta* in a red clay in Sample 157-950A-40X-4, 17 cm, which may indicate that the sample is no younger than Zone CN1a.

Calcareous turbidites sampled below 341.36 mbsf (Table 2) contain abundant Eocene to Oligocene assemblages (Fig. 25). The youngest, first evolutionary occurrence of a species in these samples provides maximum ages for the encased hemipelagic sediments. Sample 157-950A-37X-6, 120 cm, contained *Sphenolithus ciperoensis* and is probably no older than CP19, late Oligocene. Sample 157-950A-39X-6, 140 cm, contains *Isthmolithus recurvus* and is probably no older than CP15b. Sample 157-950A-40X-CC, 5 cm, contains common *Reticulofenestra umbilicus* and is probably no older than CP14 of the middle Eocene. These maximum ages poorly constrain the ages of the samples, and may be improved by careful shore-based study of the turbidites.

Planktonic Foraminifers

Planktonic foraminifers generally follow the pattern of carbonate concentration in the hole. They are abundant (Table 3) in the hemipelagic clays and bases of green turbidites and white turbidites from the surface to Sample 157-950A-9H-1, 77–79 cm (76.17 mbsf), but abundance and preservation of planktonic foraminifers decrease in the hemipelagic clays from Sample 157-950A-10H-5, 46–48 cm (89.96 mbsf), to Sample 157-950A-15H-5, 131–133 cm (139.71 mbsf), where hemipelagic clays are essentially barren. Below this depth, we sampled the bases of calcareous turbidites. The turbidites bear fossils that are contemporaneous with or older than the enclosing hemipelagic units. Specimens reworked from older zones are rare, especially in samples with abundant to common planktonic foraminifers.

The Pleistocene is defined by the range of *Globorotalia truncatulinoides,* and the sequence is divided into Zone N23 (Fig. 25) from the surface to Sample 157-950A-2H-CC at 18.41 mbsf (range of *Globigerina calida calida*) and Zone N22 from Sample 157-950A-3H-7, 82–84 cm (27.02 mbsf), to Sample 157-950A-9H-1 77–79 cm (76.17 mbsf). The assemblages contain abundant cool subtropical species, including *Globorotalia inflata,* with intervals of abundant dextral *Neogloboquadrina pachyderma.* Members of the "*Globorotalia menardii* plexus" and other tropical species like *Pulleniatina obliquiloculata* are generally rare and sporadic in occurrence.

Table 3. Abundance, preservation, zone, and lithology of samples used in foraminifer zonation.

Core, section, interval (cm)	Depth (mbsf)	Abundance	Preservation	Zone	Lithology
157-950A-					
1H-6, 108–110	8.58	A	P	N23	Hemipelagic marl
1H-CC, 0–2	8.75	A	P	N23	Hemipelagic marl
2H-6, 112–114	17.52	A	M	N23	Hemipelagic marl
2H-CC, 13–15	18.41	A	G	N23	Green turbidite
3H-7, 82–84	27.02	A	M	N22	Hemipelagic marl
3H-CC, 0–2	27.70	C	P	N22	Base of green turbidite
4H-CC, 19–21	37.60	A	G	N22	Hemipelagic ooze
5H-4, 116–118	43.07	A	G	N22	Hemipelagic ooze
6H-6, 132–134	55.42	A	M	N22	Hemipelagic ooze
6H-CC, 106–108	56.67	A	P	N22	Green turbidite
7H-6, 129–131	65.19	A	M	N22	Hemipelagic ooze
8H-6, 114–116	74.54	A	P	N22	Hemipelagic ooze
9H-1, 77–79	76.17	A	M	N22	Hemipelagic ooze
*					
10H-5, 46–48	89.96	C	P	PL6–PL4	Hemipelagic ooze
11H-6, 76–78	102.66	F	P	PL6	Hemipelagic clay
12H-5, 34–36	110.24	F	P	PL6–PL1	Hemipelagic marl
13H-5, 9–11	119.49	C	M	PL6	Hemipelagic ooze
14H-4, 102–104	128.42	C	P	PL4–PL1	Hemipelagic clay
15H-5, 131–133	139.71	C	P	PL3–M12	Hemipelagic clay
16H-2, 71–73	144.11	A	M	PL2	Calcareous turbidite
19X-2, 113–115	162.93	A	M	PL2	Calcareous turbidite
21X-5, 109–111	185.59	C	M	PL1	Hemipelagic clay
22X-1, 95–97	189.15	A	M	PL1	Calcareous turbidite
23X-2, 96–98	200.26	C	P	PL1	Calcareous turbidite
*					
24X-6, 81–83	215.81	F	P	PL1–M13	Calcareous turbidite
25X-4, 148–150	223.18	A	M	M13	Calcareous turbidite
26X-4, 89–91	232.19	A	M	M12	Calcareous turbidite
29X-6, 91–93	264.11	A	M	M13-M12	Calcareous turbidite
30X-1, 31–33	265.71	A	P	M12	Calcareous turbidite
31X-3, 111–113	279.21	A	P	M11	Calcareous turbidite
32X-6, 26–27	292.56	C	P	M8	Calcareous turbidite
34X-2, 19–21	305.80	F	P	early–middle Miocene	Calcareous turbidite
35X-1, 31–33	314.02	R	P	Barren	Calcareous conglomerate
35X-CC, 21–23	314.75	B		Barren	Calcareous conglomerate
35X-CC, 36–38	314.90	B		Barren	Calcareous conglomerate
36X-1, 99–101	324.29	F	P	M2–M1	Calcareous sand
37X-3, 7–8	336.07	F	P	?	Sand
37X-5, 27–29	339.28	B		?	Nannofossil-foraminifer ash
37X-5, 132–133	340.32	R	P	?	Volcaniclastic sandstone
38X-2, 122–125	345.32	F	P	Neogene	White foraminifer clay
39X-3, 79–81	356.09	B		?	Nannofossil clay

Notes: Key to abbreviations for abundance and preservation in "Explanatory Notes" (this volume). Asterisks (*) mark the Pliocene/Pleistocene and Miocene/Pliocene boundaries.

The Pliocene (Fig. 25) ranges from Sample 157-950A-10H-5, 46–47 cm (89.96 mbsf), to Sample 157-950A-23X-2, 96–98 cm (200.26 mbsf). Zone PL6 was recognized in four samples from 89.96 to 119.49 mbsf, but the base of the zone was not found because of the absence of the defining species, *Globorotalia miocenica.* Zones PL5 and PL4 could not be differentiated because of the absence of the defining globorotalid species, and PL3 could not be placed because *Globoquadrina altispira* disappears below the last occurrence of *Sphaeroidinellopsis seminulina* in an interval of poor preservation where hemipelagic muds become very low in calcium carbonate content. Zones PL2 and PL1 are well defined by the common occurrences of *Globigerina nepenthes, Globorotalia margaritae, Globorotalia puncticulata,* and *Globorotalia crassaformis.*

The base of PL1 and the Miocene/Pliocene boundary, however, are not precisely located. The sample beneath the last sample of Zone PL1 (Sample 157-950A-24X-6, 81–83 cm, 215.81 mbsf) contains only two species, which range into both the early Pliocene and the late Miocene, so this sample could not be assigned to a zone.

The Miocene (Fig. 25) extends from the upper Miocene in Sample 157-950A-25X-4, 148–150 cm, to the lower Miocene at the base of the core. Preservation is moderate in the upper Miocene turbidites (Table 3) but deteriorates near the base of lithologic Unit I. Preservation deteriorates drastically in the calcarenite, brown clays, and volcanic sands of lithologic Units II, III, and IV so that only sporadic samples can be assigned to zones.

In lithologic Unit I, Samples 157-950A-25X-4, 148–150 cm (223.18 mbsf), to 157-950A-30X-1, 31–33 cm, are assigned to Zones M13-M12 (Fig. 25) and contain variously *Globorotalia lenguaensis, Neogloboquadrina acostaensis, Globorotalia juanai, Globoquadrina dehiscens, Globigerina nepenthes, Globigerina decoraperta,* and *Sphaeroidinellopsis seminulina* among other species excluding the nominate taxa, *Globorotalia conomiozea, Globorotalia mediterranea,* and *Globorotalia margaritae.* Sample 157-950A-31X-3, 111–113 cm, is tentatively assigned to Zone M11. However, the nominate taxa, *Globorotalia miozea* and *Globorotalia conoidea,* do not occur in any of our samples in Hole 950A. Sample 157-950A-32X-6, 26–27 cm, is tentatively assigned to Zone M8 based on the presence of *Globorotalia peripheroronda.*

Lithologic Unit II contains a calcarenite with abundant, highly abraded bioclasts and neritic benthonic foraminifers including *Amphistegina.* The source for the coarse unit is likely one of the seamounts in the Cruiser/Hyères/Great Meteor seamount chain at a time when their peaks were at wave base or shallower.

Poorly preserved foraminifers occur sporadically in Unit III (Table 3), which consists of brown and red clays interbedded with thin turbidites. Sample 157-950A-36X-1, 99–101 cm, from this unit is tentatively placed in Zone M1/M2 (Fig. 25) because of the presence of a form transitional between *Globorotalia kugleri* and *Globorotalia peripheroronda.* Sample 157-950A-38X-3, 122–125 cm, is probably still Miocene in age based on the occurrences of *Globoquadrina ven-*

ezuelana and *Globigerinoides* sp. Deeper samples at the base of lithologic Unit III and Unit IV are barren of foraminifers.

PALEOMAGNETISM

Introduction

Paleomagnetic measurements were made on core recovered from Hole 950A to determine magnetostratigraphy and to investigate the fine structure of field changes during polarity transitions and paleosecular variation. Measurements were made on archive halves in the long-core mode with the 2G cryogenic magnetometer. Zijderveld plots were used to analyze the NRM when it was possible to carry out sufficient demagnetization steps.

All of the APC cores were demagnetized to at least 25 mT and analyzed to give a preliminary magnetostratigraphy. The results show a bias toward normal polarity, which was interpreted as a normal overprint either acquired naturally, or by drilling, or both. The latter appeared to impose a component directed downward almost vertically. This was frequently removed by low demagnetization fields of between 5 mT to 10 mT. In the absence of continuous reliable declination data, the inclination was used as the primary indicator of polarity. However, the declination was used where possible within single cores to discriminate between full reversals of the field and fluctuations in inclination.

The XCB cores were all measured in the long-core mode on the 2G magnetometer after demagnetization to 25 mT. The results show a stronger bias to normal polarity than the APC cores and appear to have acquired a stronger drill component that was again directed vertically downward. Selected cores were demagnetized progressively and showed systematic reduction of the drill moment. The XCB data have not yet been analyzed for magnetostratigraphy because of drilling-related effects.

Discrete samples from APC and XCB cores were also measured and were compared with the whole core measurement for quality control. However, the low intensity of magnetization of some samples fell below the reliable sensitivity of the instrument. In addition to standard analysis with Zijderveld plots and Schmidt nets, NRM, ARM, and IRM characteristics were utilized in an attempt to discriminate reliable primary depositional remanent magnetization (DRM) and post-depositional remanent magnetization (PDRM) from remagnetized and drilling contaminated magnetizations. A plot of ARM against IRM was used to monitor variations in magnetic phases present in the various lithologies.

Magnetostratigraphy

Plots of inclination from all cores, of inclination from pelagic interbeds, and the interpreted chron boundaries are shown in Figure 26. The locations of the various chron boundaries are also given in Table 4. The NRM intensity data and the susceptibility data from the APC whole-core MST measurements are shown in Figure 27. The peaks in susceptibility are correlatable to the gray (volcanic) turbidite layers.

The inclination change recording the onset of the Brunhes was observed between 35 and 36 mbsf, in interval 157-950A-4H-6, 20–40 cm, in a clay at the base of an interval dominated by nearly 10 m of green turbidite. The transition in direction is seen in declination as well, but there is no associated intensity decrease. In the preceding meter, a positive inclination may be a part of the reversal or of a normal event in the Matuyama. The Matuyama reversed interval appears to be further obscured by a positively magnetized volcanic rich turbidite.

There is a transition back to normal inclination between 39 and 40 mbsf, which we interpret provisionally as the top of C1r.1n, the Jaramillo. The transition lies in an interbedded pelagic layer of clay, beneath ~2 m of green turbidite and above 2 m of gray turbidite. The onset of C1r.1n is between 43 and 44 mbsf in an interval of ~1 m of interbedded pelagic clays and nannofossil oozes at the lower part of Section 157-950A-5H-4.

There is a sharp transition in inclination at the top of C2n, the Olduvai, which is observed in nannofossil ooze at 69–69.5 mbsf. This is a prominent pelagic interbed in volcanic turbidites. The base of the Olduvai also is found in nannofossil ooze at 77 mbsf, interval 157-950-9H-2, 80–85 cm. There are no reversed samples in the length representing the Olduvai.

C2r.1, the beginning of the Matuyama, is recorded as a clear reversed period, but it is followed by mixed polarities that may begin with the Réunion event.

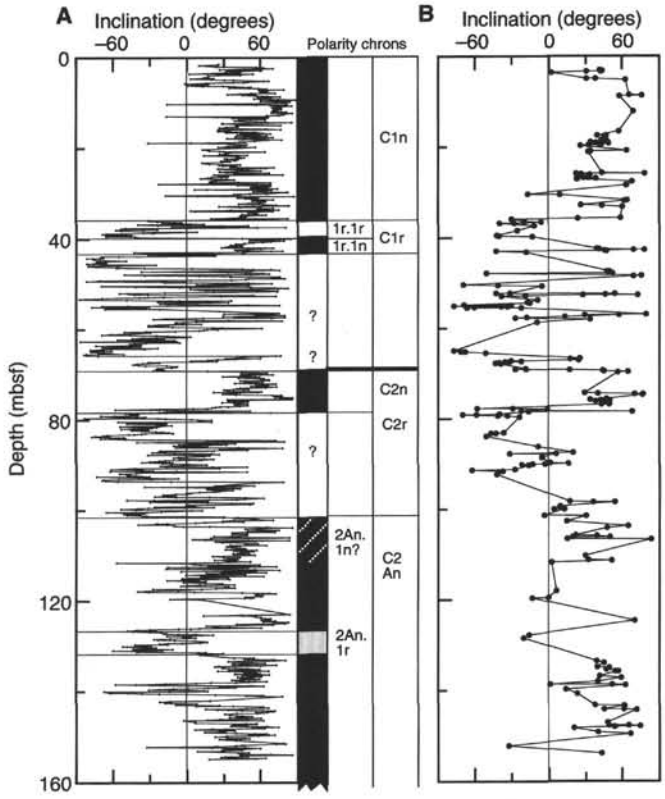

Figure 26. Magnetic data, NRM (25 mT), and interpreted polarity chrons from APC cores, Hole 950A. **A.** Inclination from all measurements. **B.** Inclination from measurements of pelagic interbeds. Filled areas = interpreted chrons and subchrons, shaded area = probable sub-chron, hatched area = problematic interval.

Table 4. Polarity chrons: ages and correlated core intervals.

Boundary	Name	Age (Ma)	Reference	Depth (mbsf)	Core, section	Length (cm)
C1n (o)	Brunhes	0.78	SBP90	35–36	4H-6	20–40
C1r.1n (t)	Jaramillo	0.99	SBP90	39–40	5H-2	60–80
C1r.1n (o)	Jaramillo	1.07	SBP90	43–44	5H-4	60–115
C2n (t)	Olduvai	1.77	SBP90	69.4	8H-3	20
C2n (o)	Olduvai	1.95	SBP90	77.5	9H-2	80–85
C2An.1n (t)	Gauss	2.60	SBP90	103.8	12H-1	15
C2An.1r (t)	Kaena	3.04	H91	126.0	14H-2	140
C2An.1r (o)	Kaena	3.11	H91	131.0	14H-6	60

Notes: (o) = onset, (t) = top. SBP90 = Shackleton et al., 1990 (see "Explanatory Notes"), H91 = Hilgen, 1991a and 1991b (see "Explanatory Notes").

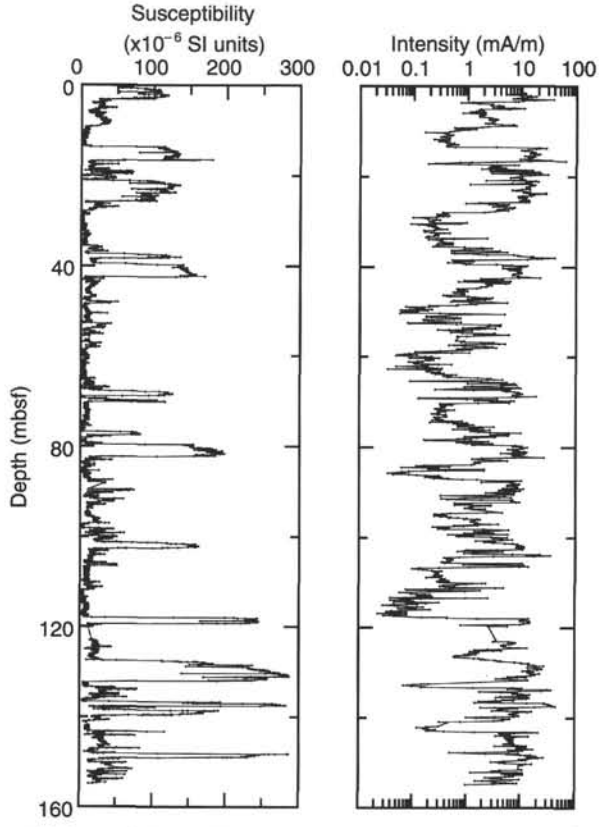

Figure 27. Susceptibility and intensity (NRM, 25 mT) from APC cores, Hole 950A.

No reversed directions are found over an interval of nearly 10 m below 104 mbsf, which we interpret to be C2An.1, the Gauss. This is followed by another length of mixed polarities, which may represent a previously undetected event. The Kaena event appears to be recorded between depths of approximately 126 and 131 mbsf. Below this, the remaining APC cores are predominantly normal and interpreted to be C2An.

The magnetostratigraphy of the XCB cores has not yet been analyzed. Shore-based analyses are necessary.

Rock Magnetism

Preliminary rock magnetism analysis was conducted utilizing NRM, ARM, and IRM demagnetization characteristics. The magnitudes of these magnetizations have also revealed systematic differences between the various lithologies. For example, in Figure 28 the intensities of ARM and IRM are plotted against each other for a selection of lithologies. The dark green, green-brown, green, and calcareous turbidites all carry relatively weak remanence. In contrast, the group of four gray turbidites and the pelagic red clays have very strong IRM and ARM. The variation in the turbidites is consistent with the volcanic nature of the gray turbidites, in contrast to the high organic content of the green and dark green turbidites. The strength of the remanence of the red clays is, however, somewhat surprising.

Plots of progressive demagnetization of NRM, and ARM against IRM, display concisely the AF demagnetization characteristics of all three remanences and can help to distinguish samples with strong overprints from those more likely to be carrying a primary NRM of a DRM or PDRM nature. For example, the ratio of NRM:IRM for depositional remanence should be of the order of 10^{-3} and about two orders of magnitude smaller than a 10^{-1} mT ARM, as is illustrated in

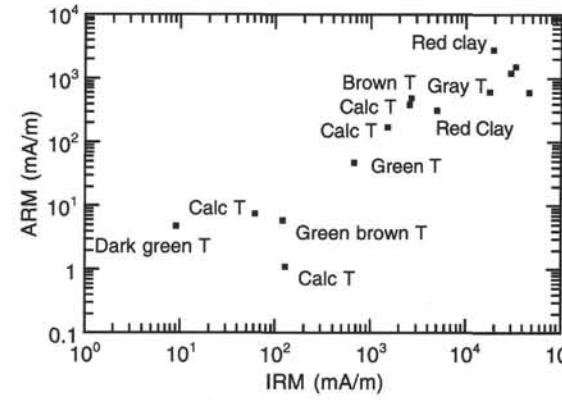

Figure 28. ARM and saturation IRM for various lithologies.

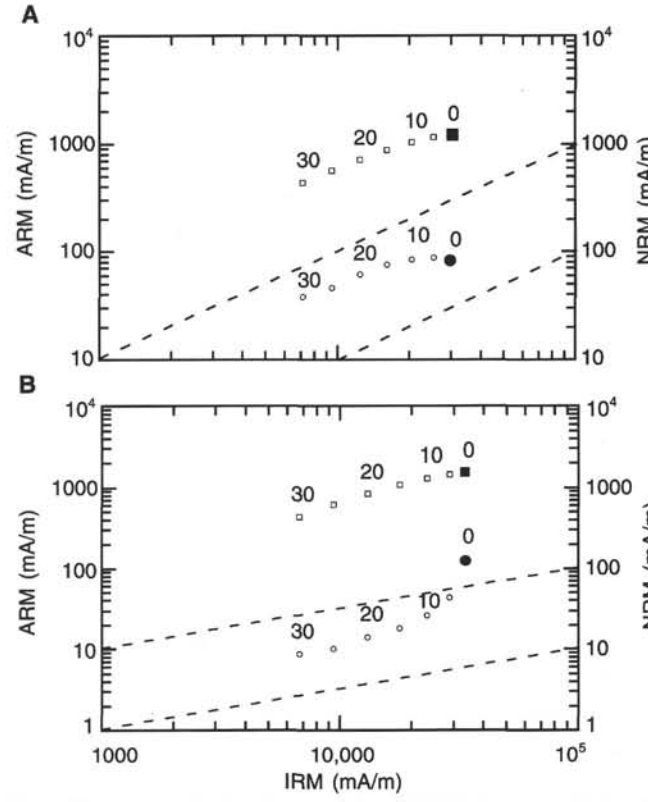

Figure 29. Demagnetization characteristics of NRM, ARM, and IRM. **A.** Sample 157-950A-14H-4, 115 cm. **B.** Sample 157-950A-13H-4, 34 cm.

the gray turbidite Sample 157-950A-14H-4, 115–117 cm (Figure 29A). The form of the demagnetization curve should follow the demagnetization plot of ARM again as it does in Figure 29A. In contrast, the gray turbidite Sample 157-950A-13H-4, 34–36 cm (Figure 29B) appears to have picked up more drill contamination, which disappears after the first three steps of demagnetization.

Conclusions

The magnetostratigraphy of Site 950 sediments is difficult to establish because the turbidites are so dominant over the interlayered pelagics in the section. However, a preliminary magnetostratigraphy for the APC cores has been produced with the assistance of the shipboard paleontologists and sedimentologists. Rock magnetic studies have provided data for the individual lithologies encountered, show-

Table 5. Interstitial-water geochemistry, Hole 950A.

Core, section, interval (cm)	Depth (mbsf)	pH	Salinity (g/kg)	Cl (mmol/L)	Alkalinity (mmol/L)	SO_4 (mmol/L)	NH_4 (μmol/L)	Na (mmol/L)	K (mmol/L)	SiO_2 (μmol/L)	Ca (mmol/L)	Mg (mmol/L)	Mg/Ca (molar ratio)
157-950A-													
1H-4, 145–150	5.95	7.49	35.0	559	4.81	27.1	152	495	11.8	489	10.5	54.2	5.18
2H-4, 145–150	14.85	7.53	35.0	557	5.38	25.1	320	502	11.7	493	10.1	53.6	5.31
3H-6, 145–150	26.15	7.55	34.5	556	5.52	22.6	353	502	12.1	556	9.32	52.1	5.59
4H-5, 145–150	35.35	7.58	34.5	564	6.05	21.7	435	500	11.0	726	8.94	50.2	5.62
5H-5, 145–150	44.85	7.58	34.5	571	6.20	20.1	601	507	11.1	619	8.61	49.5	5.75
6H-4, 145–150	52.55	7.62	34.0	558	5.83	18.0	635	499	9.81	373	8.27	50.0	6.04
7H-3, 145–150	60.85	7.67	34.0	555	4.59	16.7	685	506	10.5	312	7.81	48.6	6.22
8H-5, 145–150	73.35	7.62	34.0	553	4.66	14.8	785	499	9.74	358	7.36	45.7	6.21
9H-4, 145–150	81.35	7.62	34.0	557	4.13	13.7	873	488	9.52	285	6.83	44.8	6.55
10H-4, 145–150	89.45	7.55	34.0	553	4.10	13.7	823	503	9.19	228	7.44	45.1	6.06
12H-4, 145–150	109.85	7.62	33.0	551	4.21	10.1	978	509	8.57	268	8.42	41.4	4.92
14H-4, 145–150	128.85	7.47	33.0	553	3.83	7.94	1040	552	7.96	182	8.23	40.4	4.91
16H-4, 145–150	147.85	7.45	33.0	562	3.95	7.18	949	497	7.24	154	9.28	38.4	4.14
18-X-2, 145–150	157.35	7.63	33.0	557	3.69	6.55	871	485	7.04	272	9.69	36.5	3.76
20X-4, 140–150	175.80	7.69	32.0	547	3.46	7.36	710	477	6.17	245	10.4	37.0	3.55
22X-3, 140–150	192.60	7.62	32.0	556	3.19	6.06	886	494	7.43	226	10.7	36.5	3.43
25X-3, 140–150	221.60	7.62	32.0	555	3.14	6.68	767	490	6.92	283	12.5	37.8	3.03
27X-5, 145–150	243.95	7.58	33.0	516	3.63	5.53	700	467	5.79	201	14.2	35.4	2.49
30X-4, 140–150	271.30	7.36	33.0	527	3.70	6.12	598	490	5.78	459	19.1	33.3	1.74
33X-5, 140–150	301.80	ND	33.0	520	ND	7.72	324	430	4.03	245	25.2	32.8	1.30
36X-2, 140–150	326.20	ND	34.0	568	ND	11.8	450	489	6.10	232	25.6	31.4	1.22
39X-1, 140–150	353.70	ND	33.0	549	ND	10.8	261	440	3.53	356	33.6	26.8	0.80

Note: ND = not determined due to insufficient pore water.

Table 6. Mineralogy of Site 950 sediments determined by XRD analysis.

Core, section, interval (cm)	Depth (mbsf)	Lithology	Mineralogy	
			Dominant minerals	Accessory phases
157-950A-				
1H-4, 63–64*	5.13	Green turbidite	Calcite	Chlorite, dolomite, illite, kaolinite, quartz, smectite
1H-4, 145–150	5.95	Green turbidite	Calcite	Chlorite, dolomite, illite, kaolinite, quartz, smectite
2H-4, 145–150	14.85	Gray turbidite	Calcite	Chlorite, feldspar, illite, kaolinite, quartz, smectite
3H-6, 145–150	26.15	Pelagic marl	Calcite	Chlorite, illite, I ill-sm, kaolinite, phillipsite, quartz, smectite
4H-5, 145–150	35.35	Green turbidite	Calcite	Chlorite, feldspar, illite, kaolinite, phillipsite, quartz, smectite
5H-5, 145–150	44.85	Green turbidite	Calcite	Chlorite, illite, kaolinite, phillipsite, quartz, smectite
6H-4, 145–150	52.55	Pelagic ooze	Calcite	Quartz
7H-3, 145–150	60.85	Gray turbidite	Calcite	Quartz, smectite
8H-5, 145–150	73.35	Green turbidite	Calcite, quartz	Dolomite, feldspar, illite, kaolinite, smectite
9H-4, 145–150	81.35	Gray turbidite	Calcite	Feldspar, illite, smectite
10H-4, 145–150	89.45	Pale gray turbidite	Calcite	Quartz, smectite
12H-4, 145–150	109.85	Green turbidite	Calcite	Quartz
14H-4, 145–150	128.85	Gray turbidite	Calcite	Feldspar, quartz, smectite
16H-4, 145–150	147.85	Calcareous turbidite	Calcite	Quartz
18X-2, 145–150	157.35	Gray turbidite	Quartz, calcite	Chlorite, dolomite, illite, I ill-sm, kaolinite, smectite
20X-4, 140–150	175.80	Green turbidite	Calcite, quartz, smectite, kaolinite	Illite, I ill-sm
22X-3, 140–150	192.60	Gray turbidite	Calcite	Chlorite, dolomite, illite, quartz
25X-3, 140–150	221.60	Gray turbidite	Calcite	Chlorite, dolomite, illite, phillipsite, quartz
27X-5, 145–150	243.95	Green turbidite	Calcite, quartz	Kaolinite, I ill-sm, smectite
30X-4, 140–150	271.30	Green turbidite	Calcite, quartz	Chlorite, illite, kaolinite, phillipsite, smectite
33X-5, 140–150	301.80	Green turbidite	Quartz, smectite, kaolinite	Feldspar, illite
36X-2, 140–150	326.20	Calcareous turbidite	Calcite	
39X-1, 140–150	353.70	Red clay	Quartz, smectite	Chlorite, feldspar, illite, kaolinite, phillipsite, pyroxene
39X-7, 14–16*	361.44	Brown clay	Phillipsite, smectite	Chlorite, illite, pyroxene, quartz
39X-7, 38–40*	361.68	Brown clay	Feldspar, smectite	Chlorite, illite, I ill-sm, natrolite, quartz

Notes: All samples are pore-water squeeze cakes except those marked by an asterisk, which are additional material. I ill-sm = interstratified illite-smectite.

ing that the gray turbidites carry the strongest magnetization. Analysis of AF demagnetization of NRM suggests that the drilling component is largely, but not completely, removed by 25 mT treatment. The availability of transitions in sediments with differing sedimentation rates will permit the study of the effect of sedimentation rate on the recording of reversal transitions.

INORGANIC GEOCHEMISTRY

Introduction and Operation

A total of 22 interstitial-water samples, squeezed from 5–10-cm-long whole-rounds, were obtained between 6 and 354 mbsf at Site 950 (Table 5). Interstitial waters were extracted by routine shipboard squeezing of sediment samples, immediately after retrieval of the cores. Samples were squeezed at room temperature, and although largely excluded from contact with air, they were not processed in an oxygen-free environment. Consequently, no attempt was made to determine iron or phosphate concentrations. Samples were analyzed for pH, salinity, chlorinity, alkalinity, sulfate, ammonia, sodium, silica, potassium, calcium, and magnesium. The bulk mineralogies of pore-water squeeze cakes were determined qualitatively by XRD analysis (Table 6).

Major changes in pore-water composition occur through the sequence in response to biogeochemical reactions caused by the bacterially mediated oxidation of organic matter located principally in the organic-rich turbidites. Additional reactions in the lower half of the succession are attributed to diagenetic reactions in the silicate fraction, particularly the appearance of smectites and zeolites forming at the expense of volcanic glass.

Chloride and Salinity

Salinity decreases from seawater values (35 g/kg) in the upper 15 m to a minimum of 32 g/kg around 170–230 mbsf. Chloride shows

little depletion in this interval (Table 5). Salinity increases to 33 g/kg below 240 mbsf. An anomalously high value at 326 mbsf has probably been caused by drilling contamination, since this level also displays anomalously high chloride, sulfate, ammonia, and potassium.

Chloride fluctuates at ~555 mmol/L (slightly below the 559 mmol/L of seawater) in the upper 230 m of sediment, but falls suddenly to <530 mmol/L before increasing slightly toward the base of the hole. This Cl^- minimum, which is offset some distance below the salinity minimum, might result from the release of chemically bound water at depths from clays; the introduction of chloride-depleted pore fluids from external sources is unlikely in this open-ocean setting.

Sulfate and Alkalinity

The interstitial water SO_4^{2-} profile (Fig. 30) shows progressive depletion from 27 mmol/L at 6 mbsf (slightly less than the typical 28.9 mmol/L value of seawater) to constant levels of ~6 mmol/L between 150 and 270 mbsf and then increasing values again in the lower 80 m of core. This profile is typical of deep-water sequences undergoing moderate rates of sulfate reduction. The persistence of an SO_4^{2-} diffusion gradient to ~150 mbsf suggests that the bulk sediment accumulation rates of 3.4 cm/k.y. observed in the upper part of the section are sufficiently low to allow sulfate diffusion to keep pace with sulfate consumption. Furthermore, low residual values of SO_4^{2-} in the deeper parts and the absence of significant methane indicate that sulfate reduction has not reached completion. Decreasing sulfate in the upper beds is matched by increasing alkalinity and ammonia production to around 50 mbsf (Fig. 30). Increasing SO_4^{2-} levels at the base of the core indicate sulfate replenishment from below.

Alkalinity increases from 4.8 mmol/L at 6 mbsf (significantly higher than 2.3 mmol/L typical of seawater), to a maximum of 6.2 mmol/L around 50 mbsf (Fig. 30), then declines slowly to a minimum of 3.1 mmol/L around 220 mbsf, before increasing slightly in the lowest samples. Increasing alkalinity may be attributed to H_2S and HCO_3^- production accompanying sulfate reduction. The location of the alkalinity maximum some distance above the sulfate minimum and the ammonia maximum may be explained by carbonate precipitation at and below 80 mbsf consuming alkalinity. Declining alkalinity in the lower parts of the section may be caused by dolomite precipitation and decreasing NH_4^+ concentrations.

Ammonia

Ammonia increases progressively from 152 to 1040 µmol/L at ~130 mbsf (Fig. 30) and then declines to 261 µmol/L at the base of the sequence. Some of the decrease in the lower beds may be a result of NH_4^+ reactions with silicates. Ammonia and sulfate show essentially opposing trends confirming that the former is being regenerated largely by sulfate reduction of organic matter in the turbidites.

Calcium and Magnesium

Calcium shows a very coherent pore-water profile (Fig. 31), with close to seawater values (10.5 mmol/L) at 6 mbsf, declining linearly to a marked minimum of 6.8 mmol/L at 81 mbsf, indicating Ca^{2+} uptake into the solid phase at that level. Below 81 mbsf there is an exponential increase in dissolved Ca^{2+} concentrations, which attain a maximum of 33 mmol/L in the bottom sample. The Ca^{2+} minimum lies immediately below the alkalinity maximum, which is consistent with carbonate precipitation consuming bicarbonate.

By contrast, Mg^{2+} declines in the pore waters, from seawater values of 54.2 mmol/L near the surface (Fig. 31) to a minimum of 26.8 mmol/L in the basal sample. A temporary reversal in this trend occurs between 160 and 220 mbsf. The Mg/Ca ratio peaks at the Ca^{2+} minimum, indicating that sulfate reduction and alkalinity production are promoting calcite precipitation in the upper 80 m, below which dolomite precipitation and calcite dissolution occur.

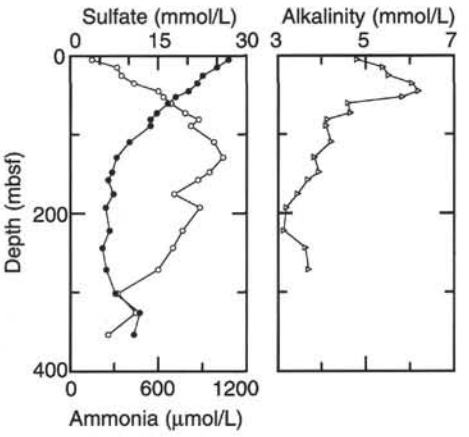

Figure 30. Interstitial-water sulfate (filled circles), ammonia (open circles), and alkalinity, Hole 950A.

Dolomite, which is a common accessory phase down to 220 mbsf (Table 6), could be precipitating through much of the sequence, although the rate of the reaction should decrease significantly below 250 mbsf, where the Mg/Ca ratio falls below 2. The renewed decline in pore-water Mg^{2+} below 220 mbsf and associated rapid Ca^{2+} production indicates reaction with the silicate fraction, probably controlled by the formation of smectites.

Silica

Silica concentrations are sensitive indicators of lithological changes, so the pore-water profile for silica is relatively uneven. However, silica climbs sharply from surficial values of 490 µmol/L to a maximum of more than 700 µmol/L at 35 mbsf (Fig. 32) before steadily declining to a minimum of 150 µmol/L at 150 mbsf. The silicate maximum at 35 mbsf, which occurs within an organic-rich turbidite, is probably caused by the dissolution of biogenic opal-A in the sediment. This is supported by the observation that diatoms occur as a minor component of organic-rich turbidites in the shallower part of the sequence, but disappear around the silica pore-water maximum.

Declining silica concentrations below 35 mbsf indicate uptake of silica by the precipitation of diagenetic phases at depth, probably smectites. It is noteworthy that an Si minimum around 150 mbsf coincides with temporary reversal in the Mg gradient, supporting the view that smectites are forming at this level. Concentrations fluctuate around 250 µmol/L in the lower part of the section, with a single anomalously high value of 459 µmol/L at 271 mbsf.

Potassium and Sodium

Pore-water potassium concentrations decline below 26 mbsf (Fig. 32) from slightly higher than seawater values of around 11–12 mmol/L to <4 mmol/L in the deepest sample. A reduction in the pore-water gradient below 170 mbsf is associated with increased phillipsite in the sediment. Further decline in potassium and falling sodium pore-water concentrations (Table 5) in the lower beds may also be ascribed to the formation of zeolite minerals (Table 6), principally phillipsite and natrolite.

ORGANIC GEOCHEMISTRY

The shipboard organic geochemistry program at Site 950 consisted of analyses of volatile hydrocarbons and determinations of inorganic carbon, total nitrogen, total carbon, and total sulfur (for methods see "Explanatory Notes," this volume).

Table 7. Elemental and organic carbon compositions of sediments, Hole 950A.

Core, section, interval (cm)	Depth (mbsf)	Sediment type	Inorganic carbon (%)	$CaCO_3$ (%)	Total carbon (%)	TOC (%)	Total nitrogen (%)	Total sulfur (%)	C/N (ratio)
157-950A-									
4H-2, 60–61	30.00	O	5.81	48.4	7.76	1.95	0.15	0.88	13.0
5H-2, 30–31	39.20	O	5.63	46.9	6.38	0.75	0.08	0.44	9.4
5H-6, 95–96	45.85	O	5.77	48.1	6.71	0.94	0.07	0.51	13.4
6H-5, 88–89	53.48	O	7.05	58.7	7.76	0.71	0.07	0.16	10.1
7H-3, 78–79	60.18	V	8.19	68.2	8.70	0.51	0.03	0.16	17.0
8H-5, 18–19	72.08	O	6.03	50.2	6.75	0.72	0.06	0.49	12.0
10H-2, 34–35	86.74	O	5.38	44.8	6.23	0.85	0.08	0.61	10.6
11H-1, 74–75	95.14	O	6.09	50.7	6.70	0.61	0.06	0.46	10.2
12H-3, 87–88	107.77	O	6.05	50.4	6.65	0.60	0.04	0.62	15.0
13H-2, 53–54	115.43	O	4.74	39.5	6.45	1.71	0.11	1.18	15.6
14H-1, 81–82	123.71	O	5.37	44.7	5.96	0.59	0.03	0.47	20.0
14H-5, 79–80	129.69	V	7.97	66.4	8.09	0.12	BD	0.14	ND
16H-1, 69–70	142.59	O	3.60	30.0	5.26	1.66	0.10	0.65	16.6
17H-4, 4–5	154.41	O	1.65	13.7	3.15	1.50	0.10	1.23	15.0
18X-2, 100–101	156.90	O	5.34	44.5	5.92	0.58	0.05	0.56	11.6
20X-3, 43–44	173.33	V	5.73	47.7	5.79	0.06	BD	0.15	ND
21X-4, 34–35	183.34	O	4.18	34.8	5.77	1.59	0.09	0.60	17.7
22X-2, 18–19	189.88	O	5.72	47.6	6.93	1.21	0.08	0.28	15.1
23X-1, 11–12	197.91	V	6.54	54.5	6.73	0.19	0.02	0.28	9.5
24X-1, 97–98	208.47	O	3.90	32.5	5.06	1.16	0.08	1.10	14.5
27X-5, 94–95	243.44	O	0.30	2.5	1.21	0.91	0.06	0.47	15.2
28X-1, 48–49	246.58	O	2.37	19.7	4.12	1.75	0.15	1.19	11.7
28X-3, 7–8	249.17	O	2.64	22.0	3.52	0.88	0.08	0.37	11.0
29X-1, 78–79	256.48	O	1.94	16.2	3.3	1.36	0.10	1.14	13.6
29X-5, 64–65	262.34	O	0.71	5.9	2.6	1.89	0.16	0.89	11.8
30X-5, 65–66	272.05	O	1.59	13.2	3.47	1.88	0.14	2.63	13.4
31X-5, 125–126	282.35	O	3.83	31.9	5.16	1.33	0.09	1.13	14.8
32X-7, 21–22	294.01	O	1.10	9.2	2.68	1.58	0.10	2.03	15.8
33X-5, 115–116	301.55	O	0.12	1.0	1.39	1.27	0.09	0.23	14.1
36X-1, 55–56	323.85	O*	0.33	2.7	0.36	0.03	BD	0.10	ND

Note: BD = below detection, ND = not determined, O = organic-rich turbidite, V = volcanic turbidite, and O* = oxidized turbidite top.

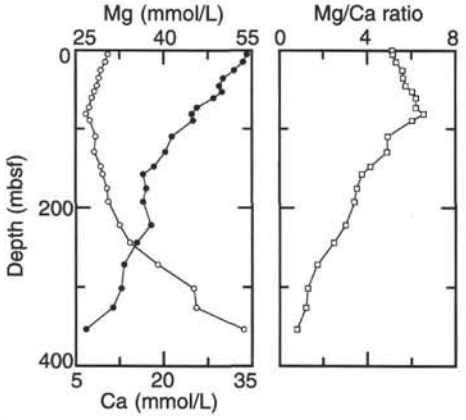

Figure 31. Interstitial-water calcium (open circles), magnesium (filled circles), and Mg/Ca ratio, Hole 950A.

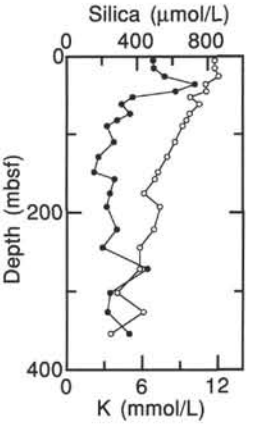

Figure 32. Interstitial-water silica (filled circles) and potassium (open circles), Hole 950A.

Volatile Hydrocarbons

Concentrations of methane (C_1) and ethane (C_2) gases were monitored in every core using the standard ODP headspace-sampling technique as part of the shipboard safety and pollution program (SSP). Throughout the entire sediment sequence of Hole 950A, the methane content remained constantly low (2–12 ppmv). A small peak at 120 mbsf (Fig. 33) coincides with a maximum in ammonia content in the analyzed pore water from squeezed sediment samples taken in core intervals adjacent to the headspace sampling. Ethane was not detected.

Carbon, Nitrogen, and Sulfur Concentrations

Results for determinations of organic carbon, total carbon, total nitrogen, and total sulfur are presented in Figure34 and Table 7. Hole 950A was sampled for carbonate with a total of 190 samples. Inorganic carbon was analyzed by the Coulometrics instrument; total carbonate as calcium carbonate showed a distinct variation with depth for four lithologies (Fig. 7): (1) pelagic interbeds (showing a marked decrease below 150 mbsf); (2) organic-rich turbidites (decreasing carbonate with depth); (3) volcanic turbidites (change from high to low carbonate at 200 mbsf); and (4) calcareous turbidites (exhibiting high carbonate contents throughout, see "Lithostratigraphy," this chapter). An overall decline in the carbonate contents of organic-rich turbidites is observed between 150 and 250 mbsf, with the darker green organic-rich turbidites found below 250 mbsf typically containing <30% $CaCO_3$.

A total of 30 samples were analyzed on the CNS-instrument. TOC for organic-rich turbidites varied between 0.6% and 2%. One sample at 323.85 mbsf contained virtually no organic carbon as this turbidite was thin and completely oxidized (Fig. 34; Table 7). The volcanic turbidites vary only from 0.05% to 0.5% organic carbon. One sample

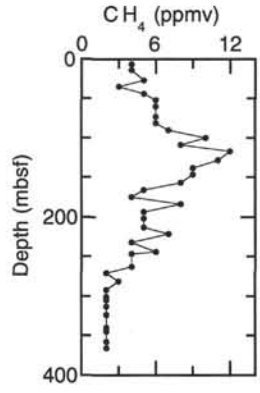

Figure 33. Methane concentrations in headspace samples from Hole 950A.

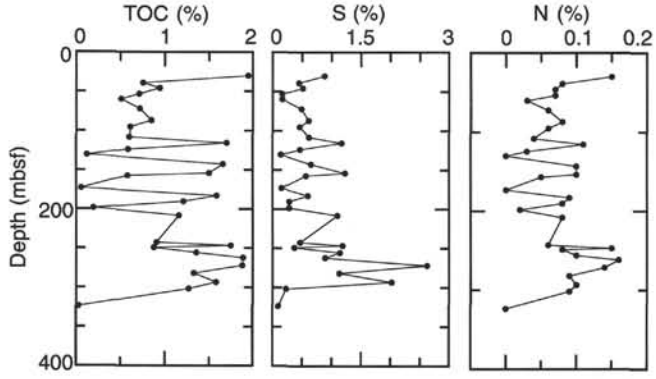

Figure 34. Concentration profiles of TOC, total sulfur, and total nitrogen from Hole 950A.

of green/brown turbidite at 294.01 mbsf contained 1.58% organic carbon (Table 7) indicating that it falls in the organic-rich category. Sulfur contents varied between 0.1% and 2.6% in the same samples as organic carbon was determined. Nitrogen contents ranged from below detection to 0.16%. Organic carbon, nitrogen, and sulfur have coinciding elevated values around 270 mbsf (Fig. 34). This probably indicates that these sediments have preserved their original organic matter and have not been subject to any major oxidation.

The C/N ratio may reveal information about the source of the organic matter. At Site 950 C/N values varied between 9 and 20 (Table 7). Marine-derived organic matter has values between 5 and 10, while land-plant organic matter has values between 20 and 100. Results from Site 950 fall between these categories. However, the richest darker green turbidites (TOC = 1.85%–1.95%) have C/N ratios between 11 and 13, which indicate more input from a marine source. Dilution with volcanic-derived material may increase the C/N ratios slightly.

PHYSICAL PROPERTIES

Introduction

The shipboard physical properties measurements program for Hole 950A included nondestructive measurements of bulk density, bulk magnetic susceptibility, compressional-wave velocity, and total natural gamma activity on whole sections of core using the MST as well as discrete measurements of shear strength and index properties. Sample intervals for the discrete measurements were selected from the most undisturbed sections of the working half of the core.

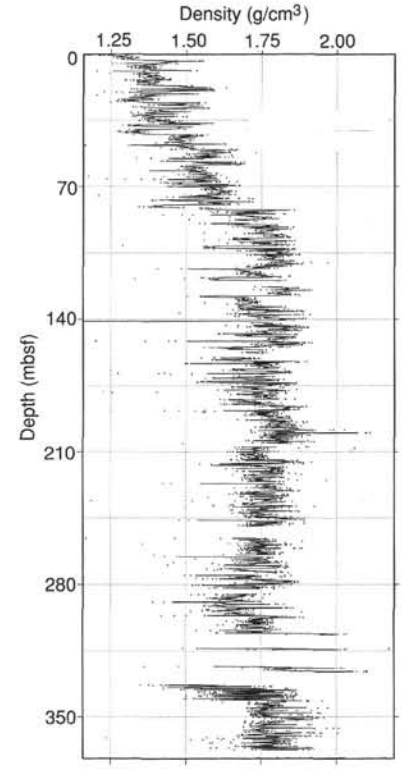

Figure 35. MST density, Hole 950A. Filtered data indicated by lines, raw data by discrete points.

Whole-core Measurements

MST

Whole-round measurements of GRAPE density and magnetic susceptibility were made on all cores from Hole 950A, and *P*-wave velocity measurements were made on cores down to ~160 mbsf. Natural gamma measurements were not made between Core 6H (50.75 mbsf) and Core 35X (131.85 mbsf) because the slow sampling rate was in conflict with the need to split the cores rapidly after retrieval for detailed pore-water analysis. Figures 35, 36, and 37 show data from the GRAPE density, *P*-wave velocity, and magnetic susceptibility sensors, respectively. The data are filtered by a running median of 12.5 cm intervals and are shown together in Figures 38 through 41 for ranges 0–100, 100–200, 200–300, and 300–400 mbsf, respectively. The plots show a significant variation in physical properties at a relatively fine scale. There is a marked correlation between these changes and the different lithologies (see "Lithostratigraphy," this chapter). For example, highs in magnetic susceptibility correspond to lows in velocity and bulk density. Many of these zones of high magnetic susceptibility were volcanic-rich gray turbidites (see "Paleomagnetism" and "Lithostratigraphy," this chapter).

Split-core Measurements

Shear Strength

Both the mechanical vane shear and the handheld penetrometer were used to measure the sediment strength and to provide a means of comparison between the two instruments. Vane shear measurements were made beginning with Core 157-950A-10H at 85.73 mbsf and were made as deep as Core 157-950A-19X at 167.66 mbsf where the sediments became too stiff for any of the vane springs; penetrometer measurements were made from 100.75 mbsf and continued to a

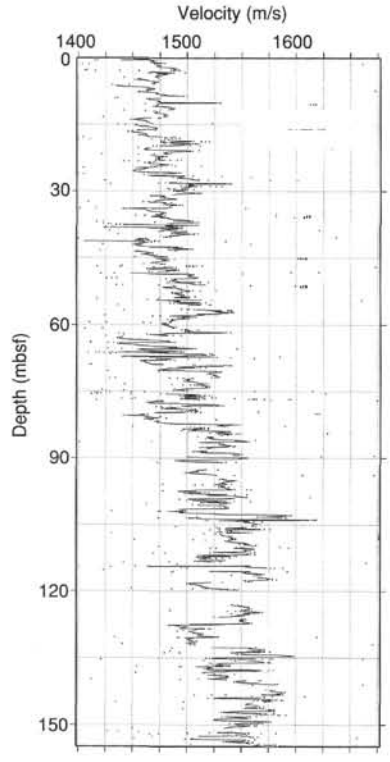

Figure 36. MST velocity, Hole 950A. Filtered data indicated by lines, raw data by discrete points.

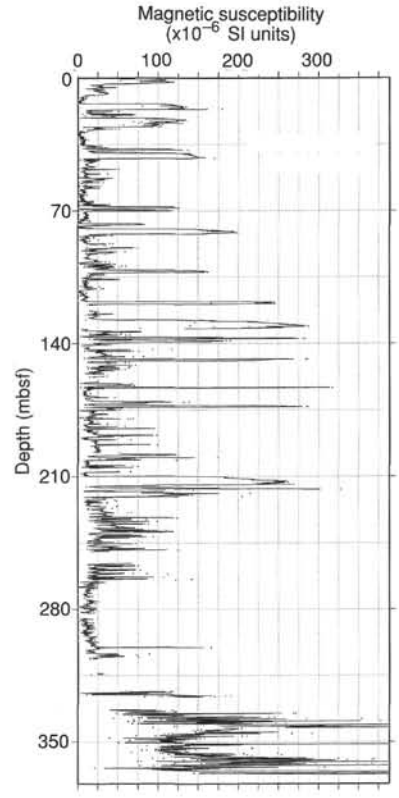

Figure 37. MST magnetic susceptibility, Hole 950A. Filtered data indicated by lines, raw data by discrete points.

depth of 268.33 mbsf where the strength of the sediment finally exceeded the measuring capability of the instrument. Data are presented in Table 8 and plotted together vs. depth downhole in Figure 42. Notice that the vane shear and penetrometer values correlate well throughout the entire interval in which both measurements were made simultaneously.

The data show a general trend of increasing strength downhole from about 40 kPa to 200 kPa, near the limit of the systems used. However, the data show a wide scatter throughout, corresponding to the variations with lithologic changes within the turbidites. Note the low strength values (50–100 kPa) in the interval between 200 and 220 mbsf. These values correspond to the weaker nannofossil-rich beds. Limitations in the instrumentation may also account for some of the data scatter.

Index Properties

Index properties were determined by gravimetric methods using discrete samples taken at an average rate of one per section in each core from Hole 950A. Calculations of index properties have been made following Methods B and C (see "Explanatory Notes," this volume). Although some variation in the values calculated by the different methods clearly exists, this difference is particularly noticeable with grain density. Values of grain density obtained by Method B (using the volume of the sample) are generally on the order of 0.2 g/cm^3 higher than those calculated by Method C (using the volume of the sample), or even higher. In some core intervals, downhole variation of both values clearly follows different trends (Fig. 43). The difficulty in measuring the true volume of the wet sample may account for these differences. Method B gives more accurate results for bulk density and dry density, whereas Method C more realistically calculates grain density, porosity, and void ratio. The two methods are correlated for each of the index properties (Fig. 44).

Values of the index properties from both methods are presented in Table 9. Figure 45 shows wet-water content, void ratio, and porosity calculated using Method C, and bulk density calculated using Method B. Between 0 and 200 mbsf there is a gradual increase with depth in bulk density values from 1.420 g/cm3 to 1.830 g/cm3, and a corresponding decrease in water content (54% to 32%), porosity (76% to 54%), and void ratio (3.4 to 1.2). Below this depth variations on all properties are more subtle, but there is marked variability in the interval between 300 and 335 mbsf. This region corresponds to a zone of low core recovery. Figure 46 shows dry density calculated using Method B and grain density calculated using Method C, alongside strength (vane shear and penetrometer values plotted together). The dry density shows a similar trend to that observed for bulk density, increasing downhole from 0.6 g/cm^3 near the seafloor to 1.6 g/cm^3 at 200 mbsf. Grain density decreases downhole from 2.84 g/cm^3 near the seafloor to 2.62 g/cm^3 at approximately 150 mbsf where a break in the general trend is observed and relatively higher values (average of 2.74 g/cm^3) have been measured. Below this depth, grain density values show a slight decrease with depth and have a wide scatter of data in the low-recovery zone. The variability in the data from this low-recovery zone can be substantiated with MST density and logging data (Fig. 35; see "Downhole Measurements," this chapter).

DOWNHOLE MEASUREMENTS

Logging Operations

A total of four Schlumberger tool strings were run in Hole 950A: the seismic stratigraphy and lithoporosity combinations, the FMS, and the geochemical logging tool. The wireline heave compensator (WHC) was used to counter ship heave resulting from the mild sea state conditions (0.3–1.5 m heave). The base of the drill pipe was set at 95 mbsf and was raised to 70 mbsf at the end of each main upgoing log. A summary of the logging tool strings used on Leg 157, the basis of their measurement principles, and logging operations are dis-

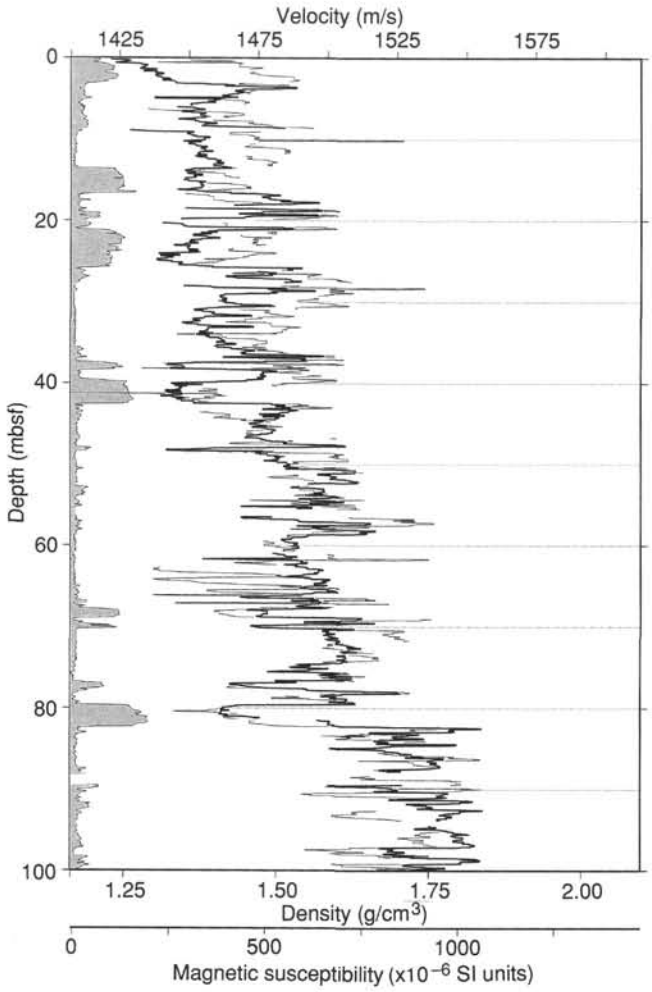

Figure 38. Filtered MST magnetic susceptibility (shading), velocity (light trace), and gamma-ray density (bold trace) for 0–100 mbsf, Hole 950A.

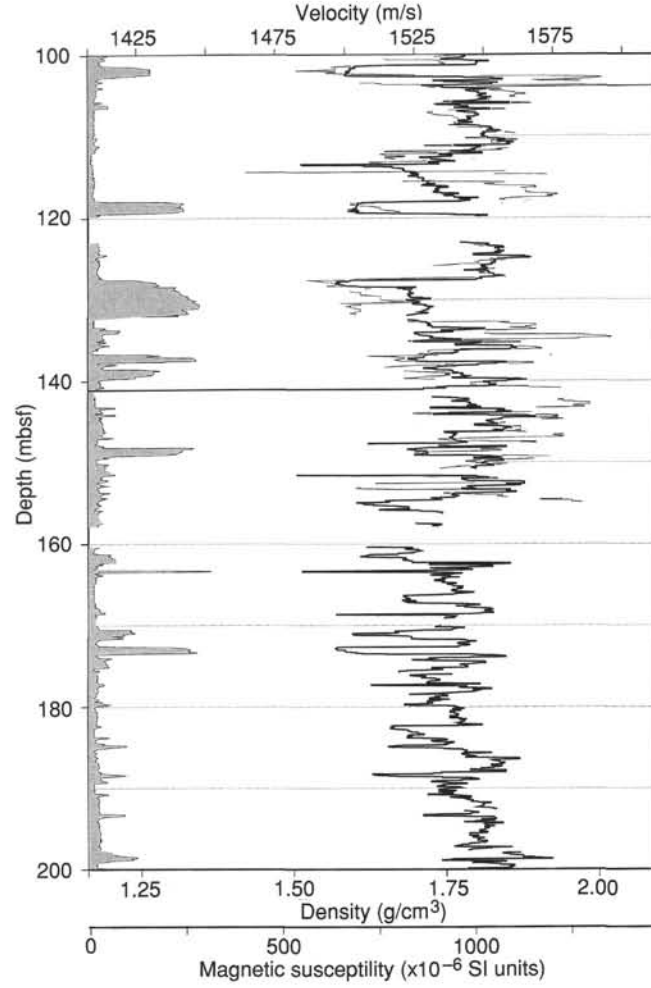

Figure 39. Filtered MST magnetic susceptibility (shading), velocity (light trace), and gamma-ray density (bold trace) for 100–200 mbsf, Hole 950A.

cussed in the "Explanatory Notes" (this volume). A summary of the Hole 950A logging operations is given in Table 10.

The seismic stratigraphic tool string comprising sonic (LSS), induction (DIT), and natural gamma-ray (NGT) tools along with the Lamont-Doherty temperature logging tool was run first. Total penetration in Hole 950A was 381.3 mbsf, the tool string was able to reach a depth of 365 mbsf, indicating about 16 m of hole fill. Data were recorded at a logging speed of 1600 ft/hr from this depth to 251 mbsf. A second main upgoing log was then recorded at 1600 ft/hr from 363 mbsf to the mud line. The second tool string, the lithoporosity, comprising density (HLDT), neutron porosity (CNT), and natural gamma-ray (NGT) was run from 364 mbsf to 259 mbsf at 900 ft/hr. The tool was then lowered back down to 359 mbsf and the main upgoing log recorded at 900 ft/hr to the base of pipe (70 mbsf).The HLDT was run in high resolution mode recording data at 1.2 in. increments. The third tool string run was the geochemical, consisting of an NGT, an aluminum activation clay tool (AACT), and the gamma-ray spectrometry tool (GST). This tool string reached a depth of 326 mbsf where further downward progress was prevented by an obstruction, probably a bridge caused by swelling smectite clays, as indicated from the caliper log of the previous run. A main upgoing log was recorded from this depth to the mud line and then a repeat pass was conducted from 325 mbsf to 251 mbsf both at a logging speed of 550 ft/hr. The final tool string run in Hole 950A was the FMS consisting of a FMS in combination with an NGT. Three upgoing logs were recorded in all: the first from 314 mbsf to 75 mbsf at 1500 ft/hr, the second from 312 to 233 mbsf at 1500 ft/hr, and the final from 305 mbsf to the end of pipe (at 70 mbsf) at a logging speed of 1800 ft/hr.

Log Quality

The main logs from Hole 950A are shown in Figures 47 and 3. The logs are generally of good quality, although above 70 mbsf in the drill-pipe section, the sonic, induction, and density data are invalid, and the natural gamma-ray and other geochemical data are highly attenuated by the presence of the drill pipe. Hole 950A is rugose in parts, shown by the hole caliper in Figure 3; the density and FMS logs have suffered as a result. The white area in the center of the figure shows the diameter of a gauge hole drilled with the XCB bit, while the shaded areas show how much wider the hole is than originally drilled. In the comparison of log bulk density to discrete measurements on core (Fig. 48), the log bulk density appears to have some low density "dropouts" that correlate, for the most part, with zones of wider borehole. Dropouts occur when pad contact with the borehole wall is incomplete and results in a small amount of borehole fluid being included with the measurement of sediment density.

For the most part, the velocity data from the logs are high quality. Some cycle skipping and other noise is present in the raw log data,

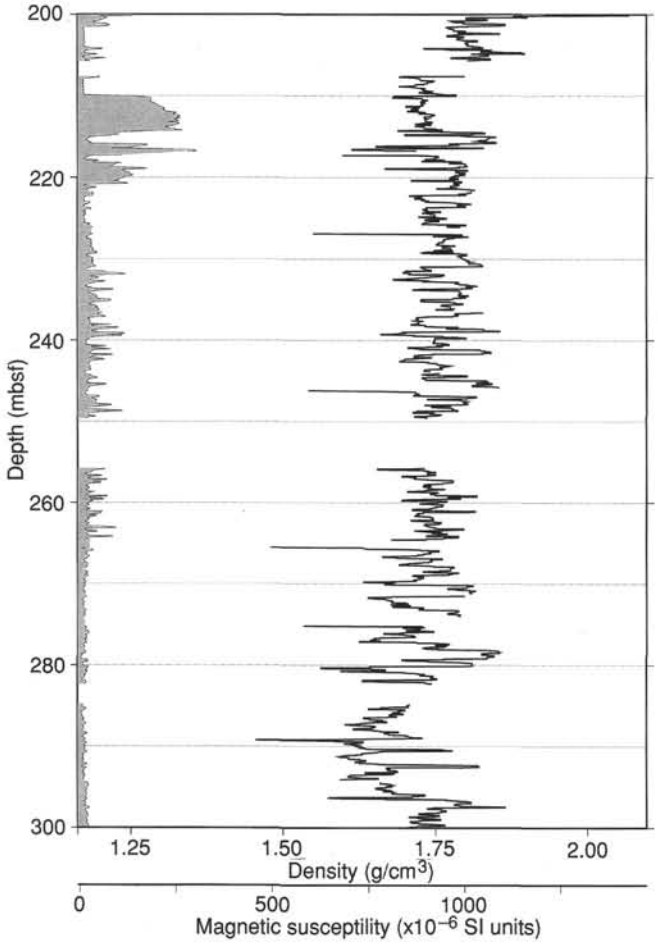

Figure 40. Filtered MST magnetic susceptibility (shading) and gamma-ray density (bold trace) for 200–300 mbsf, Hole 950A.

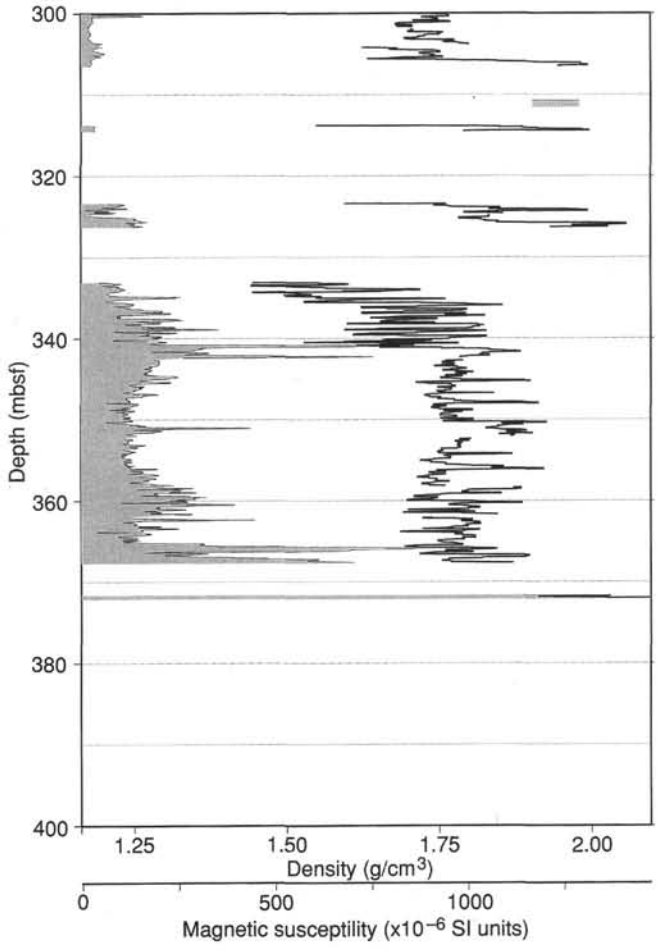

Figure 41. Filtered MST magnetic susceptibility (shading) and gamma-ray density (bold trace) for 300–400 mbsf, Hole 950A.

but shipboard processing of the traveltimes eliminated most of these excursions. The sonic velocity presented in Figure 3 is the processed data and has been merged with the *P*-wave velocity data from the MST (see "Physical Properties," this chapter). Post-cruise waveform analysis could enhance these data.

Hole width also affects the natural gamma-ray activity log by artificially raising the count rate where the hole is narrow and lowering it where it is wide. Post-cruise processing of these data will remove such artifacts. The other geochemical data from the AACT and GST require extensive post-cruise processing to transform the relative elemental data, obtained aboard the *JOIDES Resolution*, into weight percent elemental and oxide concentrations. Ratios of the relative elemental yields and the thermal neutron capture cross-section (sigma), however, can be used to show lithological variation downhole (Fig. 49).

Results

Lithology-log Units

The interval logged in Hole 950A (~70–365 mbsf) covers lithologic Units I to III, which are based on sedimentological descriptions of the recovered cores (see "Lithostratigraphy," this chapter). The Quaternary to middle Eocene lithologic sequence that this interval represents is dominated by an unlithified sequence of thick turbidite muds separated by thin pelagic ooze in the upper 305.6 mbsf; beneath it is dominated by pelagic red clay.

Based on the wireline data, the logged section can be divided into five main log units that broadly correspond to the lithologic units. Log Unit I covers the region from the end of pipe, 70 mbsf, to 205 mbsf. This unit is characterized by a broadly cyclical total gamma-ray activity with no major trends downhole (Fig. 47). The cyclical nature of this log reflects the varying clay component of this sequence of thick interbedded turbidites. The high gamma-ray values correspond to the clay-rich organic and volcanic turbidites, and the low values correspond to the low-clay carbonate-rich turbidites. The low gamma-ray carbonate-rich intervals can also be delineated as high values in the carbonate index log (Ca/[Ca + Si + Fe]) from the gamma-ray spectrometry tool (Fig. 49). The physical logs of bulk density and resistivity are fairly constant over log Unit I, increasing gradually downhole and following a normal compaction trend (Fig. 3).

Log Unit II (205–235 mbsf) is a transitional zone between log Units I and III, and it has an increasing trend in gamma-ray and a corresponding decrease in carbonate index (Figs. 47 and 49). The density, sonic, and resistivity logs show an inflection in the downward lithification trend, seen in log Unit I, with constant or slightly decreasing values with depth (Fig. 3).

Log Unit III (235–308 mbsf) is characterized by a higher and more constant gamma-ray (Fig. 47) with corresponding very low carbonate values (Fig. 49). This corresponds to a higher clay component of the formation both in the turbidites and pelagics with much lower carbonate values than in the log units above. While this is broadly recognized in the lithological description of core material it is clear

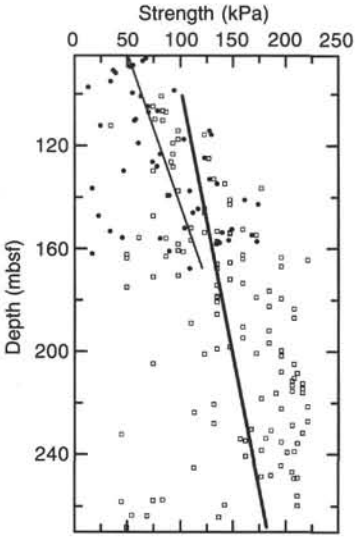

Figure 42. Strength data determined by vane shear (filled circles) and hand-held penetrometer (open squares) methods, Hole 950A.

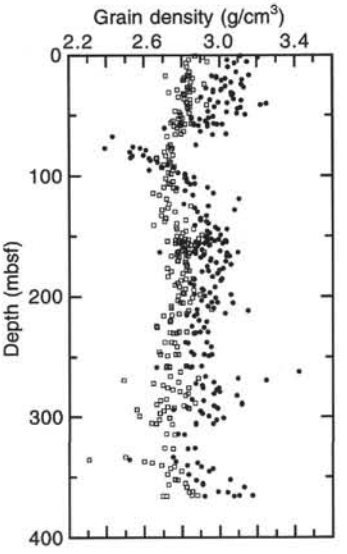

Figure 43. Contrast in Methods B (filled circles) and C (open squares) calculations for grain density.

Table 8. Strength measurements, Hole 950A.

Core, section, interval (cm)	Depth (mbsf)	Vane (kPa)	Res (kPa)	Pen (kPa)
157-950A-				
10H-1, 83–84	85.73	67	34	
10H-2, 72–73	87.12	64	32	
10H-3, 88–89	88.78	56	30	
10H-4, 132–133	89.32	53	29	
10H-5, 120–121	90.70	36	20	
10H-6, 68–69	91.68	39	19	
11H-1, 59–60	94.99	34	17	
11H-2, 137–138	97.27	13	5	
11H-3, 102–103	98.42	94	43	
11H-4, 48–49	99.38	55	30	
11H-5, 30–31	100.70	63	34	
11H-5, 35–36	100.75			82
12H-1, 69–70	104.59	69	34	
12H-1, 75–76	104.65			74
12H-2, 98–99	106.38	79	43	
12H-2, 104–105	106.44			83
12H-3, 5–6	106.95	70	32	
12H-3, 5–6	106.95			86
12H-4, 121–122	109.61	58	29	
12H-4, 121–122	109.61			76

Note: Vane = undrained shear strength as measured by the vane shear, Res = residual shear strength, and Pen = unconfined shear strength as measured by the penetrometer, converted to kPa.

Only a part of this table is reproduced here. The entire table appears on the CD-ROM (back pocket).

from the log data where this transition occurs. Sediment accumulation rate calculations (see "Sediment Accumulation Rates," this chapter) correlate with this lithological change, indicating a much slower rate of sedimentation than in the units above. In log Unit III, resistivity values (Fig. 3) are slightly lower, and hence porosity values (Fig. 50) are higher than in the log unit above. This is probably a result of the chemically bound water within the clay minerals. The thermal neutron capture cross-section recorded by the GST defines this unit well with fairly high constant readings in comparison to the beds above and below.

The transition downward into log Unit IV (308–332 mbsf) is sharply defined in all of the logging data (Figs. 3, 47, 49). It represents a change to a massive calcareous floatstone unit. Core recovery in this zone was very poor (Cores 34X to 36X) and only 1.1 m of this lithology was recovered within Core 34X. The log data show that there are three main "floatstone" units within this zone. The uppermost and thickest is from 308–318.5 mbsf, and it is well defined by low gamma-ray and thermal neutron capture cross section and by high density, resistivity, velocity, and carbonate log values (Figs. 3, 47, and 49). This bed also exhibits a grading from top to bottom in the physical logs (Fig. 3) that indicates that it is coarser grained toward the bottom. The physical logs also best delineate two further "floatstone" beds (from 322 to 324.5 mbsf and 326 to 332.5 mbsf) that are interbedded with thin pelagic and turbidite beds, which were the only material recovered in the corresponding cores (Cores 35X and 36X; see "Lithostratigraphy," this chapter).

Log Unit V (332–355 mbsf; the base of the logged section) exhibits a sharp increase in total gamma-ray counts, which is attributable mainly to increased K and Th components in the formation (Figs. 47). This unit corresponds to the lower Miocene to middle Miocene "red clays" recovered in the cores. Volcanic ash also was present in many layers within this zone and is probably responsible for the striking increase in the Th/U ratio observed in the logging data (Fig. 51). Bulk density is relatively high and constant in this zone. Apparent in the caliper log within this unit are narrow zones (Fig. 3) interpreted as bridges formed by the swelling of smectite clays; such smectite clays were observed in the recovered split core material when it came into contact with fresh water. This bridge formation was probably the cause of the obstruction that prevented the following geochemical and FMS tool strings from reaching the base of the hole.

Temperature

The Lamont-Doherty temperature tool was deployed on three of the four tool strings in Hole 950A. During the drilling process cold seawater is circulated in the hole to cool the formation surrounding the borehole. Once drilling ceases the temperature of the formation will gradually rebound to equilibrium temperature. Three readings of bottom hole temperature were obtained over a period of 25 hr by the temperature tool, allowing us to apply the principles of Lachenbruch and Brewer (1959). In this method the temperature evolution can be extrapolated to calculate the initial or "virgin" formation temperature (Fig. 52). This calculation gave a virgin formation temperature of 13.28°C at a depth of 365 mbsf; with a mud line temperature of 2.25°C this translates to a thermal gradient of 30.22°C/km.

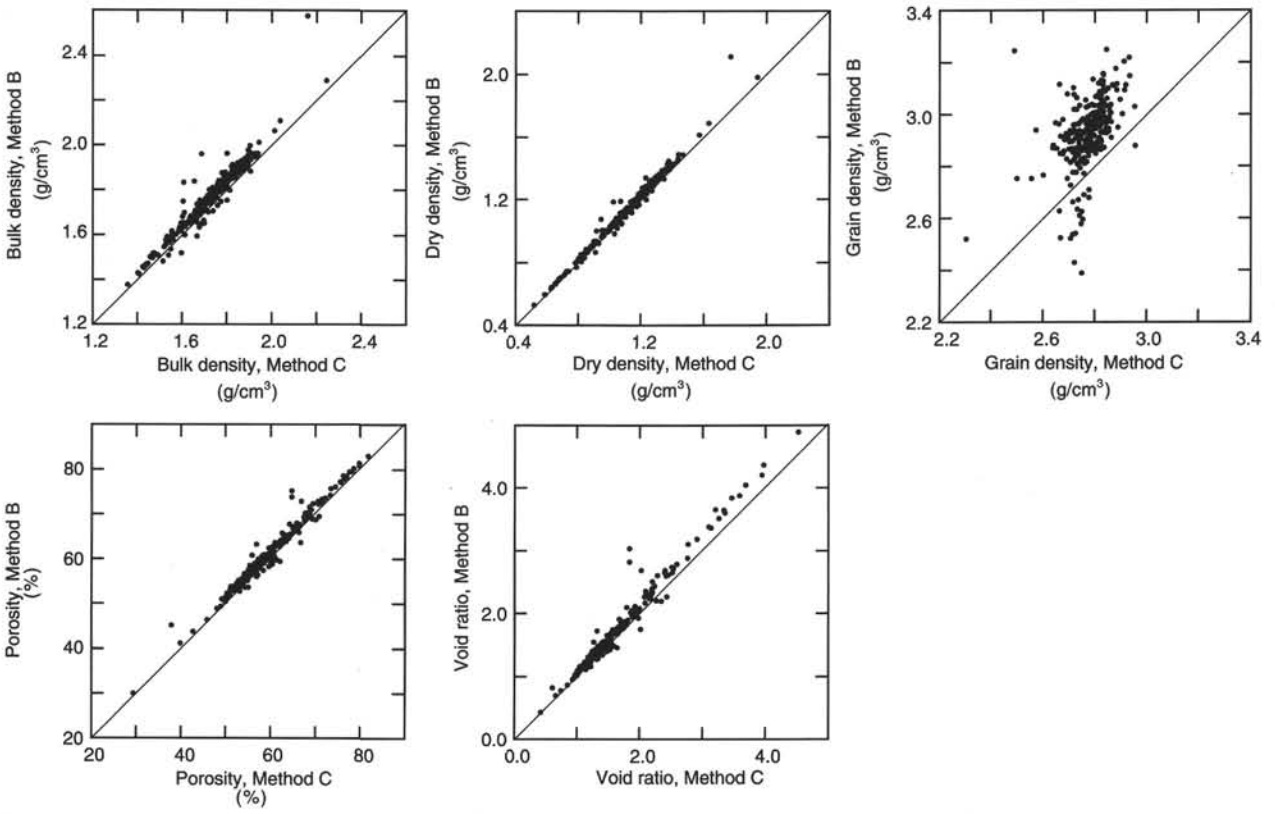

Figure 44. Correlations between Methods B and C for bulk density, dry density, grain density, porosity, and void ratio.

Table 9. Index properties, Hole 950A.

Core, section, interval (cm)	Depth (mbsf)	WCw (%)	WCd (%)	BDb (g/cm³)	BDc (g/cm³)	GDb (g/cm³)	GDc (g/cm³)	DDb (g/cm³)	DDc (g/cm³)	Porb (%)	Porc (%)	VRb	VRc
157-950A-													
1H-1, 86–88	0.86	61.71	161.15	1.38	1.36	3.11	2.87	0.53	0.52	83.04	81.88	4.89	4.52
1H-2, 52–54	2.02	58.29	139.75	1.43	1.40	3.21	2.91	0.60	0.59	81.39	79.90	4.37	3.97
1H-3, 100–102	4.00	48.39	93.75	1.56	1.53	3.04	2.84	0.80	0.79	73.58	72.19	2.79	2.60
1H-4, 86–88	5.36	52.24	109.36	1.51	1.49	3.15	2.94	0.72	0.71	77.07	75.80	3.36	3.13
1H-5, 48–50	6.48	54.81	121.30	1.47	1.44	3.08	2.83	0.66	0.65	78.47	76.99	3.65	3.35
2H-1, 69–71	9.59	54.18	118.23	1.47	1.45	3.04	2.83	0.67	0.66	77.84	76.55	3.51	3.26
2H-4, 79–81	14.19	54.67	120.62	1.47	1.44	3.09	2.84	0.67	0.65	78.44	76.99	3.64	3.35
2H-6, 38–40	16.78	46.55	87.11	1.60	1.56	3.16	2.83	0.86	0.83	72.87	70.66	2.69	2.41
2H-6, 86–88	17.26	45.79	84.47	1.59	1.55	2.96	2.72	0.86	0.84	70.93	69.13	2.44	2.24
2H-6, 141–143	17.81	39.49	65.27	1.70	1.67	2.98	2.84	1.03	1.01	65.52	64.42	1.90	1.81
3H-1, 38–40	18.78	38.61	62.89	1.72	1.68	2.98	2.81	1.05	1.03	64.68	63.33	1.83	1.73
3H-1, 120–122	19.60	46.91	88.34	1.58	1.55	3.03	2.86	0.84	0.83	72.32	71.13	2.61	2.46
3H-3, 46–48	20.66	55.79	126.20	1.46	1.43	3.12	2.81	0.64	0.63	79.35	77.61	3.84	3.47
3H-3, 65–67	20.85	41.14	69.90	1.68	1.64	3.01	2.81	0.99	0.96	67.26	65.69	2.05	1.92
3H-4, 79–81	22.49	54.69	120.69	1.47	1.44	3.06	2.85	0.67	0.65	78.29	77.03	3.61	3.35
3H-5, 82–84	24.02	58.06	138.41	1.43	1.41	3.12	2.92	0.60	0.59	80.80	79.77	4.21	3.94
3H-6, 119–121	25.89	41.11	69.80	1.68	1.64	3.03	2.85	0.99	0.97	67.39	65.98	2.07	1.94
3H-7, 85–87	27.05	46.50	86.92	1.60	1.56	3.13	2.83	0.86	0.83	72.64	70.61	2.66	2.40
3H-7, 133–135	27.53	41.33	70.46	1.66	1.64	2.93	2.84	0.97	0.96	66.83	66.17	2.01	1.96
4H-1, 70–72	28.60	40.42	67.85	1.69	1.65	3.01	2.83	1.01	0.99	66.60	65.23	1.99	1.88

Notes: WCw = water content (% wet sample weight), WCd = water content (% dry sample weight), BD = bulk density, GD = grain density, DD = dry density, Por = porosity, and VR void ratio. Suffixes "b" and "c" on column heads indicate value calculated using Method B and Method C, respectively (see "Explanatory Notes," this volume).

Only a part of this table is reproduced here. The entire table appears on the CD-ROM (back pocket).

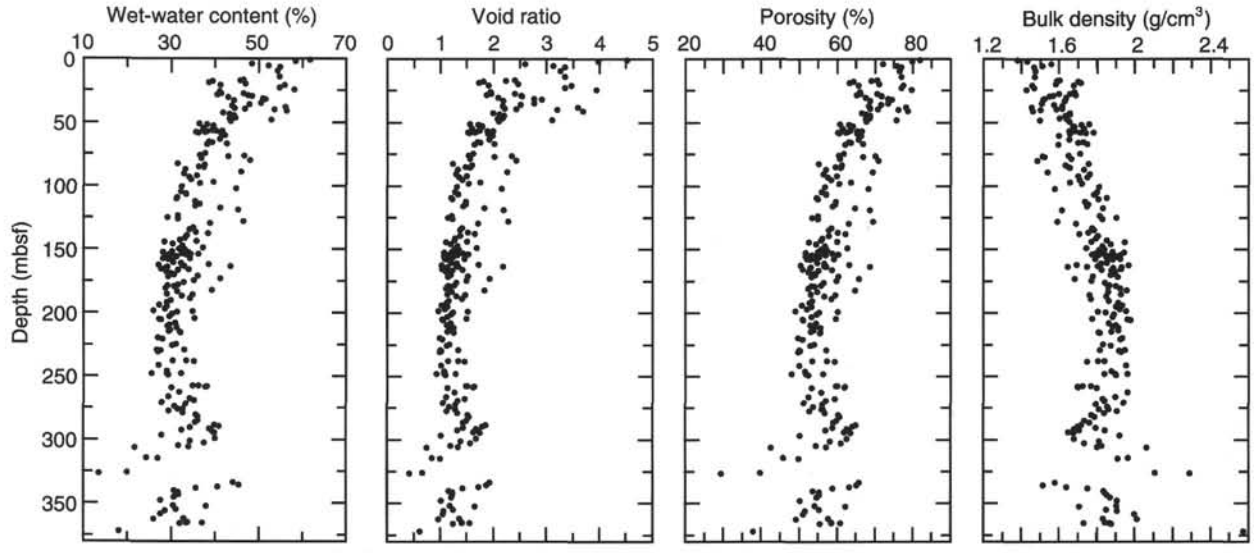

Figure 45. Wet-water content, void ratio (Method C), porosity (Method C), and bulk density (Method B), Hole 950A.

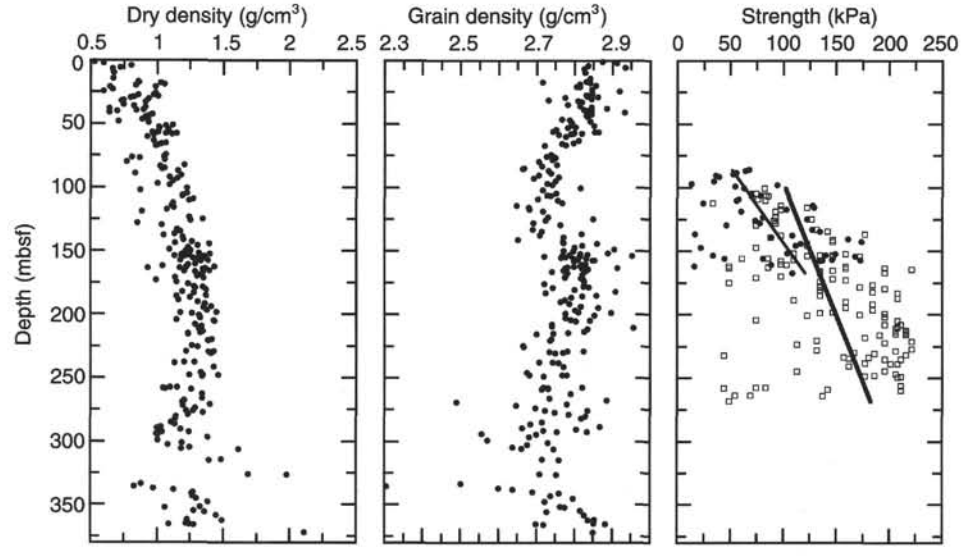

Figure 46. Dry density (Method B), grain density (Method C), and strength data determined from vane shear (filled circles) and penetrometer (open squares), Hole 950A.

Porosity Estimates from Resistivity

Porosity can be determined from the resistivity logs by using the Archie equation (Archie, 1942):

$$S_w^{\ a} = aR_w/f^m R_t,$$

where S_w is the water saturation, equal to 1 for these virtually hydrocarbon-free sediments, R_w is the resistivity of the formation water, f is the fractional porosity, R_t is the measured formation resistivity, and both a and m are constants depending on lithology and pore space geometry.

We calculated porosity using the medium phasor induction resistivity log (IMPH) from the dual induction tool with set values of a = 1 and m = 2.4. R_w was calculated based on its known relationships to temperature and salinity (Keller, 1982); temperature was taken from the Lamont-Doherty temperature tool, and interstitial salinities from core measurements (see "Inorganic Geochemistry," this chapter).The calculated porosities show an excellent correlation with those determined from discrete core samples (Fig. 50), verifying the high quality of the induction log data.

FMS

The three passes of the FMS in the hole visually define the cyclic bedding of this thick sequence of turbidites and pelagic sediments in the form of microresistivity images, which are recorded on this volume's accompanying CD-ROM (back pocket). The individual turbidites are more homogenous features in the images, and the pelagic intervals exhibit a more laminated nature. Figure 53 shows a 2 m section of images from 288 to 290 mbsf. The thick, more resistive (light) bed is a volcanic turbidite exhibiting some internal bioturbation, evident as darker patches, which was also noted in core material recovered from this interval. The FMS images should help to integrate the

Table 10. Summary of logging operations, Hole 950A.

Date (August 1994)	Time (UTC)	Activity
09	0500	Last core on deck.
		Prepare hole for logging.
	1200	Rig up NGT-LSS-DIT (+TLT).
	1227	RIH with NGT-LSS-DIT.
	1439	Start downgoing log from 120 to TD 365 mbsf (16 m of hole fill).
	1518	Upgoing log at 1300 ft/hr from 365 to 251 mbsf. RIH to TD.
	1539	Main upgoing log at 1300 ft/hr from 363 mbsf to the mudline (pipe pulled to 70 mbsf).
	1638	POOH.
	1810	Rig up NGT-CNT-HLDT (+TLT).
	1845	RIH with NGT-CNT-HLDT.
	2026	Upgoing log from 363 to 260 mbsf at 900 ft/hr. HLDT run in high resolution mode. RIH to TD.
	2109	Main upgoing log at 900 ft/hr from 363 mbsf to EOP (pulled to 70 mbsf).
	2218	End of upgoing log, POOH.
09	0030	Rig up NGT-AACT-GST (+TLT).
	0100	RIH with NGT-AACT-GST. Unable to pass obstruction at 326 mbsf.
	0325	Main upgoing log at 550 ft/hr from 325 mbsf to mudline (pipe pulled to 70 mbsf). RIH for repeat section.
	0532	Upgoing log at 550 ft/hr from 325 to 251 mbsf. POOH.
	0750	Rig up NGT-FMS.
	0825	RIH with FMS.
	1027	Upgoing log from 310 to EOP (pulled to 70 mbsf) at 900 ft/hr. RIH to TD
	1112	Upgoing log from 312 to 233 mbsf at 900 ft/hr. RIH to TD.
	1140	Upgoing log from 305 mbsf to EOP (pulled to 70 mbsf). POOH.
	1340	Rig down (2 hr). End of logging operations.

Note: Drillers TD = 381.3 mbsf. WD = 5448.6 mbrf. EOP = 95.24 mbsf.

core and logging measurements and aid the delineation of individual turbidites. It is hoped that the dipmeter data calculated from the images may provide information on the emplacement direction of the different turbidite units on to the abyssal plain.

SEDIMENT ACCUMULATION RATES

Sediment accumulation rates for Site 950 are based on 24 nannofossil, 10 planktonic foraminiferal, and 8 paleomagnetic age determinations (Table 11). Because calcium carbonate is better preserved in the pelagic layers in the upper part of the hole (0–150 mbsf), most of the age data is concentrated in this interval. Nannofossils, however, were found consistently in pelagic layers to 200 mbsf and rarely between 200 and 275 mbsf. Below this all datum levels are based on nannofossil and foraminiferal FOs in turbidites.

Two types of sediment accumulation rate curves have been produced, one for the total sediment including turbidites, pelagic layers and the calcarenites (Figs. 54 and 55) and one for the pelagic layers only (Figs. 56 and 57). The pelagics-only curve is based on the stacked thicknesses of pelagic clays, marls, and oozes and gives an indication of the background accumulation rate. This curve shows the timing of major changes in the CCD that have affected calcium carbonate preservation. The pelagics-only curve allows the extrapolation of the accumulation rate for the pelagic red clays in the lower part of the hole where age data are absent. Ages taken from this plot were then used to constrain plots of the total sediment sequence of deeper intervals.

Pelagic Accumulation Rates

The pelagic accumulation rates are well constrained by numerous data points in the upper 20 m of the stacked pelagic sequence, including eight paleomagnetic reversals (Fig. 54). The accumulation rate from 2.6 Ma to the present averages 5.6 m/m.y; this decreases sharply to 1.5 m/m.y. between 2.6–6.5 Ma. The change in accumulation rate is coincident with a change in pelagic sediment type from constant clays below to alternating clays, marls, and oozes. It also coincides with the onset of Northern Hemisphere glaciation (Shackleton et al., 1984), which was accompanied by a sharp lowering of the CCD. This lowering of the CCD allowed carbonate to be preserved at Site 950, but the alternation of clays, marls, and oozes suggests strong fluctuations in the depth of the CCD over the past 2.6 Ma.

Microfossils are rare below 20 m in the pelagic layers and many samples were barren. Nevertheless, datum points were found between 6.5 and 13.2 Ma in pelagic layers. Of these the first appearances are likely to be the most reliable as these are not subject to reworking. The accumulation rate curve drawn through these points (ignoring LO points 34 and 37, which lie above the curve indicating reworking), gives a rate of 0.85 m/m.y. for the interval 6.5–10.4 Ma (Fig. 55). This rate of accumulation for pelagic clay has been extrapolated for the clay sequence to the base of the hole where it gives an age of 47.4 Ma. The FADs of *Chiasmolithus oamaruensis* and *Reticulofenestra umbilicus* (points 41 and 42, respectively) near the base of the hole, however, suggest a slightly younger age, and therefore a higher rate of accumulation of the pelagic clay. This is unlikely to be greater than the pelagic accumulation rate between 2.6 and 6.5 Ma, where a small amount of carbonate was still preserved, and so a second (and more tentative) accumulation rate has been extrapolated from the 1.5 m/m.y. rate (shown as a dashed line in each figure).

Total Sediment Accumulation Rates

The pelagic accumulation rate curves were used to calculate the age of the base of each core from Core 28X to the base of the hole, and this data is plotted with the conventional microfossil and paleomagnetic data in Figures 56 and 57. In each graph the dashed line represents an alternative higher accumulation rate based on the dashed extrapolated line in Figure 55. The accumulation rate between 0–3.1 Ma averages 42 m/m.y. Between 3.1 and 6.5 Ma, the rate falls to 28 m/m.y., with a further fall to 9 m/m.y. between 6.5 and 11 Ma. From 11 to 13.6 Ma the rate is higher again at 21 m/m.y. The lower rates between 6.5 and 11 Ma are marked in the cores by thinner turbidites and thicker pelagic layers indicating less frequent turbidity flows.

Cores 34X, 35X, and 36X all had poor recovery. The cores and the downhole logging showed this interval to consist of three calcarenite floatstone units (at 308–318.5, 322–324.5, and 326–332.5 mbsf) interlayered with turbidites. Below the floatstones the sedi-

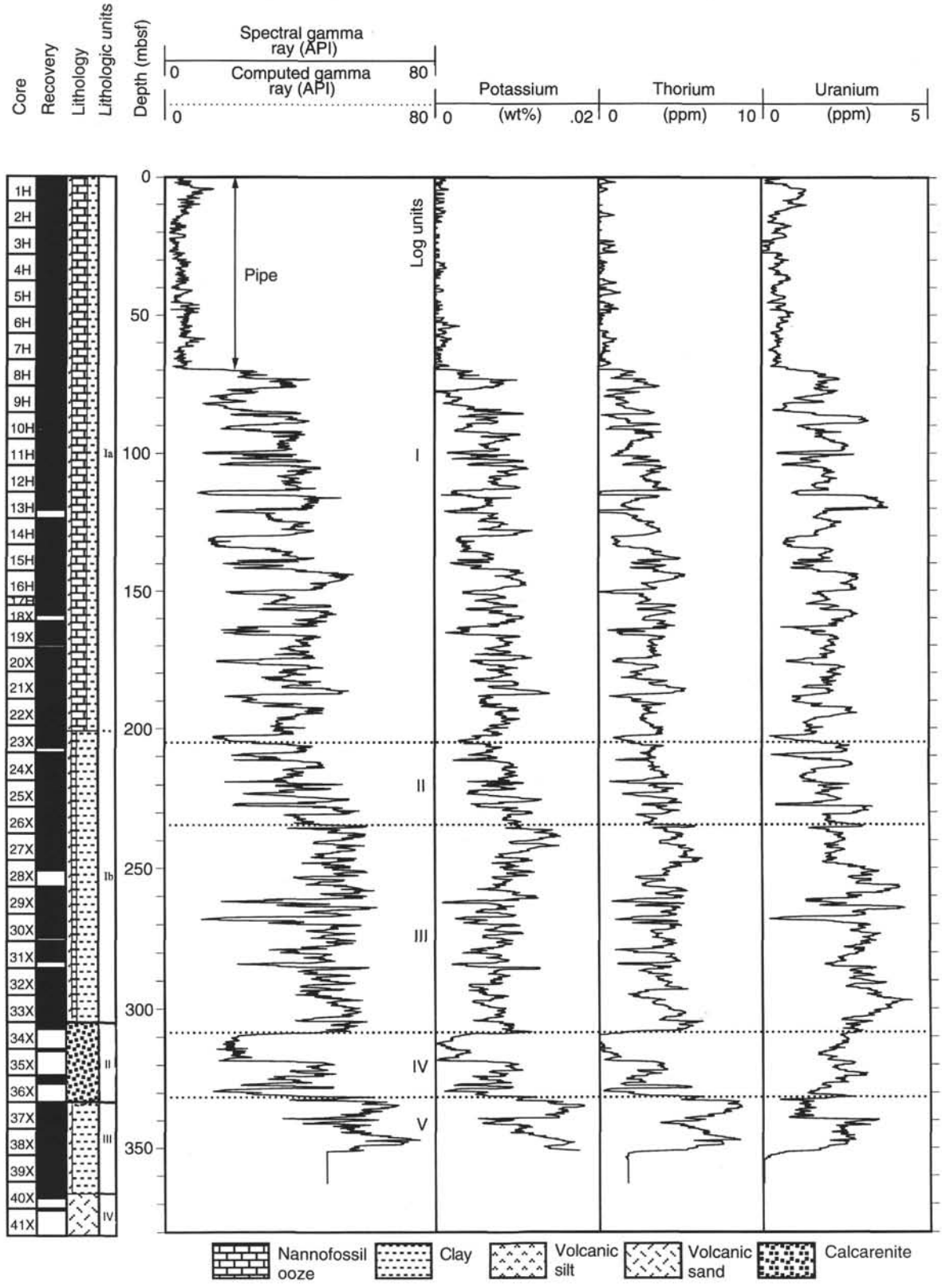

Figure 47. Natural gamma-ray data, Hole 950A, from the NGT recorded on the seismic stratigraphic tool string. The left shows the total gamma-ray count; tracks for K, U, and Th components of the total gamma-ray signal follow.

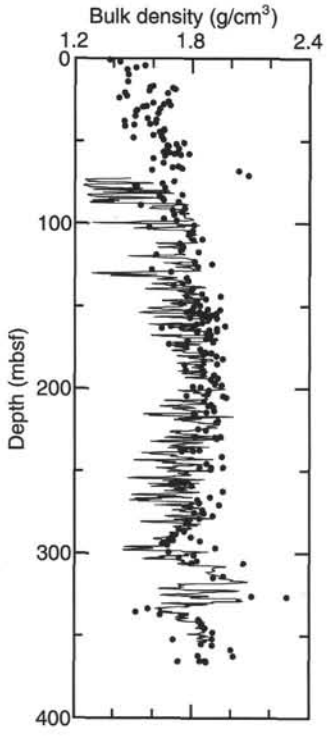

Figure 48. Bulk density log from the HLDT plotted as a function of depth against porosity measurements on discrete core samples (see "Physical Properties," this chapter).

ment consists of predominantly pelagic clay with thin volcaniclastic turbidites. Sediment accumulation rates here are about 1 m/m.y. The floatstones were deposited between 13.5 and 15 Ma, and this age marks the onset of turbidites derived from the northwestern African margin.

REFERENCES

Archie, G.E., 1942. The electrical resistivity log as an aid in determining some reservoir characteristics. *Trans. Am. Inst. Min. Metall. Pet. Eng.,* 146:54–62.

Bouma, A.H., 1962. *Sedimentology of Some Flysch Deposits: A Graphic Approach to Facies Interpretation:* Amsterdam (Elsevier).

Colley, S., and Thomson, J., 1985. Recurrent uranium relocations in distal turbidites emplaced in pelagic conditions. *Geochim. Cosmochim. Acta,* 49:2339–2348.

Crowley, T.J., 1983. Calcium carbonate preservation patterns in the central North Atlantic during the last 150,000 years. *Mar. Geol.,* 51:1–14.

de Lange, G.J., Jarvis, I., and Kuijpers, A., 1987. Geochemical characteristics and provenance of late Quaternary sediments from the Madeira Abyssal Plain, North Atlantic. *In* Weaver, P.P.E., and Thomson, J. (Eds.), *Geology and Geochemistry of Abyssal Plains.* Geol. Soc. Spec. Publ., 31:147–165.

Gardner, J.V., 1975. Late Pleistocene carbonate dissolution cycles in the eastern equatorial Atlantic. *In* Sliter, W.V., Bé, A.W.H., and Berger, W.H. (Eds.), *Dissolution of Deep-Sea Carbonates.* Spec. Publ. Cushman Found. Foraminiferal Res., 13:129–141.

Keller, G.V., 1982. Electrical properties of rocks. *In* Carmichael, R.S. (Ed.), *Handbook of Physical Properties of Rocks* (Vol. 1): Boca Raton, FL (CRC Press), 217–293.

Lachenbruch, A.H., and Brewer, M.C., 1959. Dissipation of the temperature effect in drilling a well in Arctic Alaska. *U.S. Geol. Surv. Bull.,* 1083-C:73–109.

Mazzullo, J.M., Meyer, A., and Kidd, R.B., 1988. New sediment classification scheme for the Ocean Drilling Program. *In* Mazzullo, J., and Graham, A.G., *Handbook for Shipboard Sedimentologists.* ODP Tech. Note, 8:45–67.

Piper, D.J.W., 1978. Turbidite muds and silts on deep-sea fans and abyssal plains. *In* Stanley, D.J., and Kelling, G. (Eds.), *Sedimentation in Submarine Canyons, Fans and Trenches:* Stroudsburg, PA (Hutchinson and Ross), 163–176.

Rothwell, R.G., Pearce, T.J., and Weaver, P.P.E., 1992. Late Quaternary evolution of the Madeira Abyssal Plain, Canary Basin, NE Atlantic. *Basin Res.,* 4:103–131.

Searle, R.C., 1987. Regional setting and geophysical characterization of the Great Meteor East area in the Madeira Abyssal Plain. *In* Weaver, P.P.E., and Thomson, J. (Eds.), *Geology and Geochemistry of Abyssal Plains.* Spec. Publ. Geol. Soc. London, 31:49–70.

Shackleton, N.J., Backman, J., Zimmerman, H., Kent, D.V., Hall, M.A., Roberts, D.G., Schnitker, D., Baldauf, J.G., Desprairies, A., Homrighausen, R., Huddlestun, P., Keene, J.B., Kaltenback, A.J., Krumsiek, K.A.O., Morton, A.C., Murray, J.W., and Westberg-Smith, J., 1984. Oxygen isotope calibration of the onset of ice-rafting and history of glaciation in the North Atlantic region. *Nature,* 307:620–623.

Thomson, J., Colley, S., Higgs, N.C., Hydes, D.J., Wilson, T.R.S., and Sørensen, J., 1987. Geochemical oxidation fronts in NE Atlantic distal turbidites and their effects on the sedimentary record. *In* Weaver, P.P.E., and Thomson, J. (Eds.), *Geology and Geochemistry of Abyssal Plains.* Geol. Soc. Spec. Publ. London, 31:167–178.

Weaver, P.P.E., and Kuijpers, A., 1983. Climatic control of turbidite deposition on the Madeira Abyssal Plain. *Nature,* 306:360–363.

Weaver, P.P.E., and Rothwell, R.G., 1987. Sedimentation on the Madiera Abyssal Plain over the last 300,000 years. *In* Weaver, P.P.E., and Thompson, J. (Eds.), *Geology and Geochemistry of Abyssal Plains.* Geol. Soc. Spec. Publ. London, 31:71–86.

Weaver, P.P.E., Rothwell, R.G., Ebbing, J., Gunn, D., and Hunter, P.M., 1992. Correlation, frequency of emplacement and source directions of megaturbidites on the Madeira Abyssal Plain. *Mar. Geol.,* 109:1–20.

Weaver, P.P.E., and Thomson, J. (Eds.), 1987. *Geology and Geochemistry of Abyssal Plains.* Geol. Soc. Spec. Publ. London, 31.

Weaver, P.P.E., Thomson, J., and Jarvis, I. 1989. The geology and geochemistry of Madeira Abyssal Plain sediments: a review. *In* Freeman, T.J. (Ed.), *Advances in Underwater Technology, Ocean Science and Offshore Engineering* (Vol. 18): London (Graham and Trotman), 51–78.

Wendt, I., Kreuzer, H., Müeller, P., von Rad, U., and Raschka, H., 1976. K-Ar age of basalts from Great Meteor and Josephine seamounts (eastern North Atlantic). *Deep-Sea Res.,* 23:849–862.

Ms 157IR-104

NOTE: For all sites drilled, core-description forms ("barrel sheets") and core photographs can be found in Section 3, beginning on page 181. Smear-slide and thin-section data are given in Section 4, beginning on page 305. The CD-ROM (back pocket, this volume) contains physical properties and geochemical data, MST data, logging data, and color core photographs (Sites 950 and 953 only).

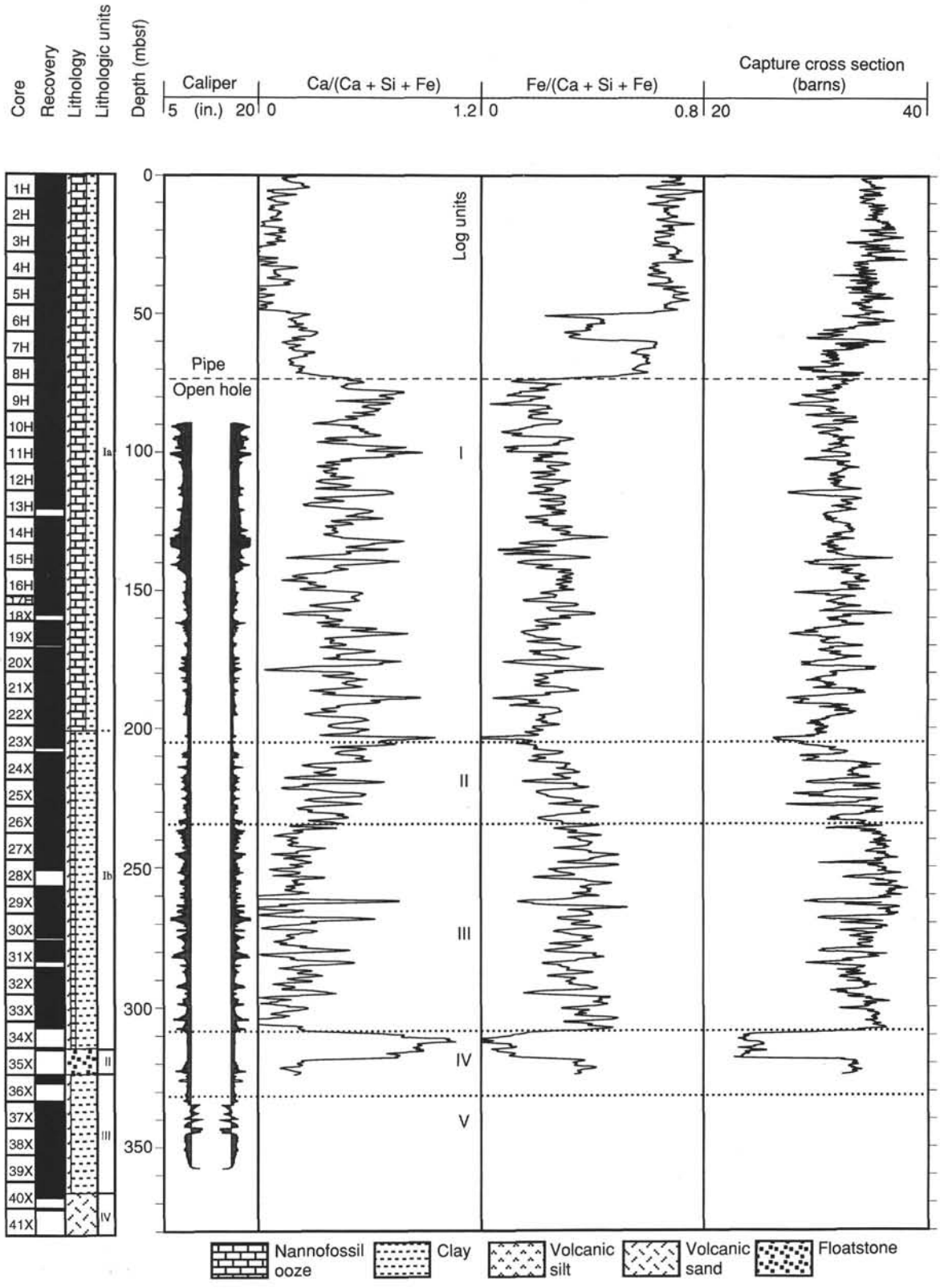

Figure 49. Hole 950A geochemical logs. Caliper data from the HLDT shown with data from the GST, a carbonate index (Ca/[Ca + Si + Fe]) and iron index (Fe/[Ca + Si + Fe]), as well as the thermal neutron capture cross section of the formation. The carbonate and iron indices logs have undergone a linear five-point (0.75 m) moving average smoothing for presentation clarity.

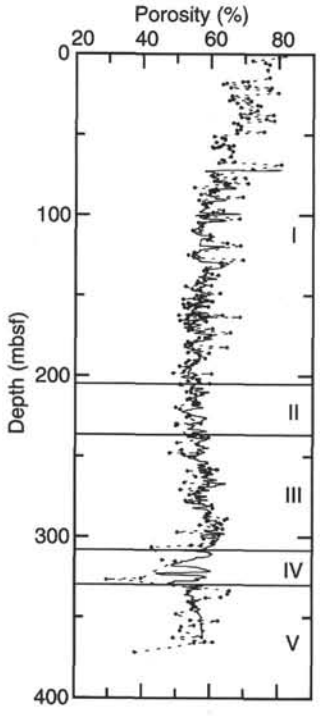

Figure 50. Porosity derived from the medium phasor induction of the dual induction tool compared with porosity measurements on discrete core samples. The input resistivity data and the final porosity log are unsmoothed. Log units are indicated by roman numerals.

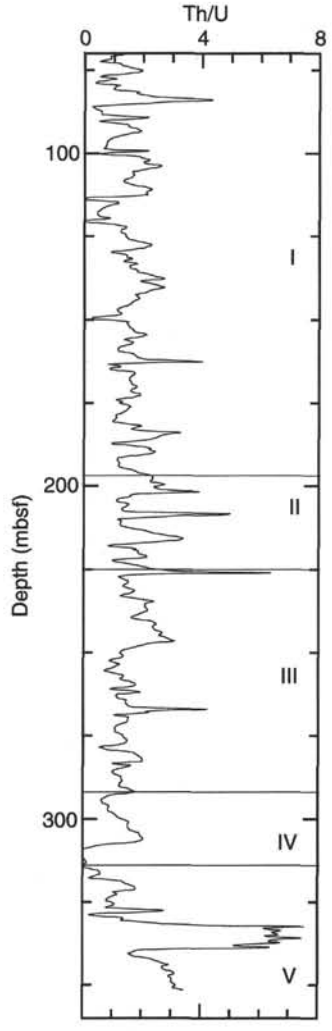

Figure 51. Th/U ratio from the NGT, from the seismic stratigraphic tool string, plotted as a function of depth. Note the spike in the ratio around Core 37X (333.0–342.6 mbsf) where numerous ash layers were recovered. Log units are indicated by roman numerals.

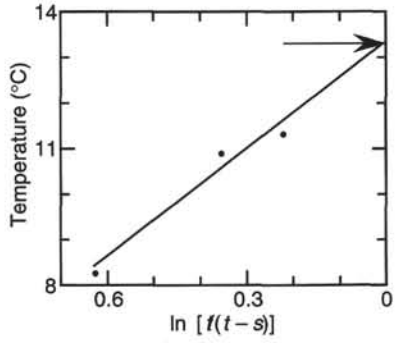

Figure 52. Observed maximum thermometer temperatures plotted against ln $[t/(t-s)]$ for Hole 950A (s = 5 hr). In the argument of the natural logarithm, t is the time since the drill bit first reached the depth in question and s is the duration of the drilling disturbance at that depth. Arrow shows estimated equilibrium temperature, 13.28°C.

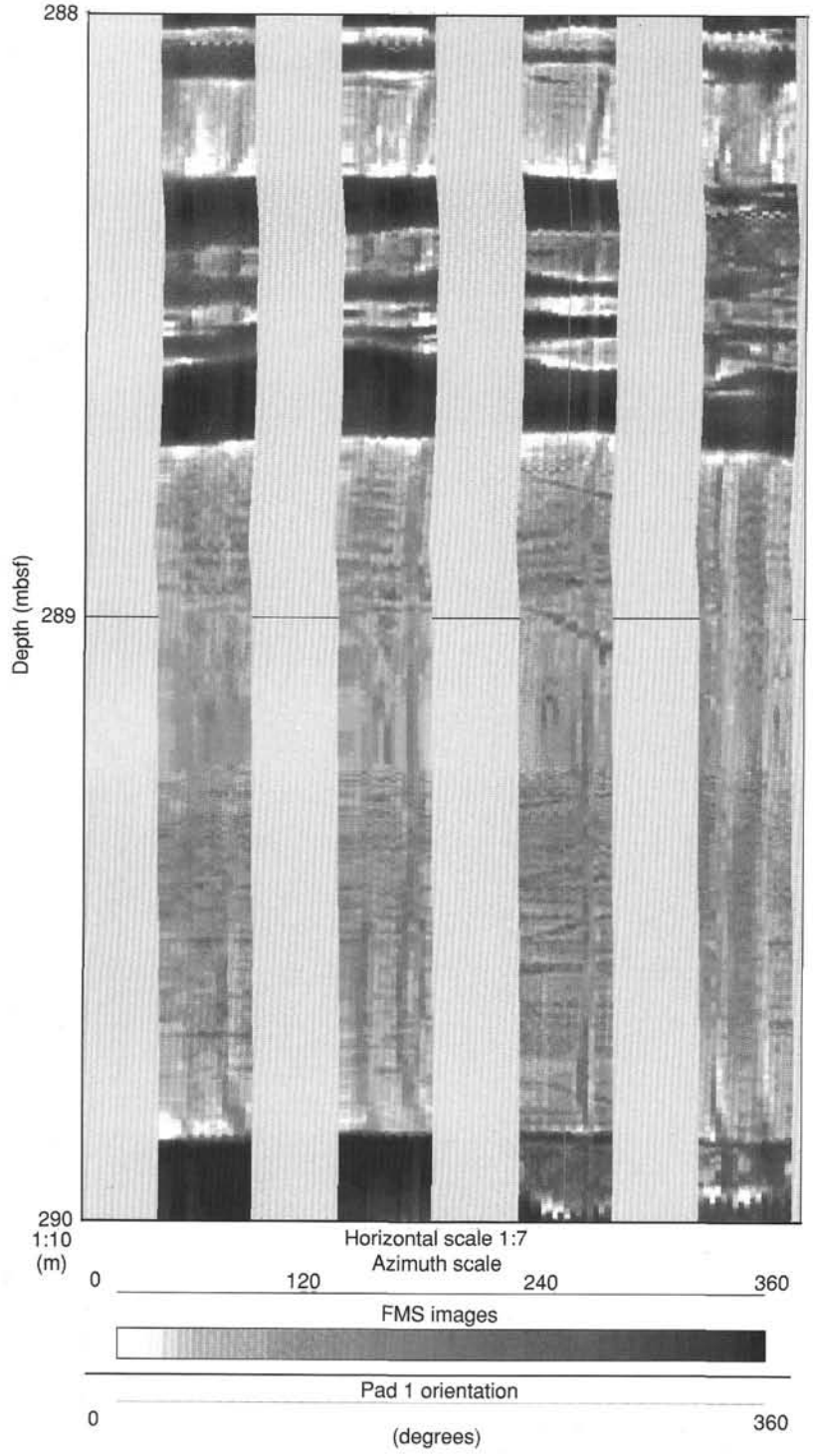

Figure 53. FMS data for the interval 288–290 mbsf. The four vertical tracks represent the oriented microresistivity images from each of the four orthogonal pads of the FMS. The lighter the images the higher the resistivity of the corresponding lithology. The main more resistive bed is a ~1-m-thick mud turbidite of volcanic origin; the minor internal disturbance visible is a result of bioturbation.

Table 11. Datum levels used in calculation of sediment accumulation rate curves.

	Event	Sample		Depth (mbsf)		Pelagic depth (m)		Age (Ma)
		Top	Bottom	Top	Bottom	Top	Bottom	
		157-950A-	157-950A-					
1	FO *E. huxleyi*	2H-7, 20.5	3H-7, 78	18.11	26.98	1.02	2.66	0.26
2	LO *P. lacunosa*	2H-7, 20.5	3H-7, 78	18.11	26.98	1.02	2.66	0.46
3	Brunhes/Matuyama boundary	4H-6, 20–40	—	35.80	—	3.44	—	0.78
4	LO *R. asanoi*	4H-6, 110.5	4H-CC, 12	36.51	37.52	3.64	4.02	0.83
5	Jaramillo top	6H-1, 55–70	—	39.70	—	4.24	—	0.98
6	Jaramillo bottom	6H-6, 80–145	—	42.70	—	4.36	—	1.05
7	FO *R. asanoi*	5H-5, 2	6H-6, 90	43.42	55.00	5.08	6.69	1.06
8	Olduvai top	8H-3, 20	—	69.40	—	9.33	—	1.76
9	FO *G. carribeanica*	8H-6, 109	9H-3, 70	74.49	79.10	10.07	11.74	1.80
10	FO *Gr. truncatulinoides*	9H-1, 77–79	10H-5, 46–48	76.17	89.96	10.73	14.70	1.92
11	LO *D. brouweri*	8H-6, 109	9H-3, 70	74.49	79.10	10.07	11.74	1.95
12	Olduvai bottom	9H-2, 80	—	77.50	—	11.02	—	1.98
13	FO *Gr. inflata*	9H-1, 77–79	10H-5, 46–48	76.17	89.96	10.73	13.23	2.19
14	LO *D. pentradiatus*	9H-6, 12	10H-5, 59	83.02	90.09	12.21	13.36	2.44
15	Gauss/Matuyama boundary	12H-1, 15	—	103.80	—	14.60	—	2.60
16	LO *D. tamalis*	10H-6, 17	11H-5, 96	91.17	101.36	13.60	14.26	2.76
17	Kaena top	14H-2, 140	—	126.00	—	15.12	—	3.04
18	Kaena bottom	14H-6, 60	—	131.00	—	15.47	—	3.11
19	LO *Ss. seminulina*	14H-4, 102–104	15H-5, 131–133	128.42	139.71	15.42	16.05	3.15
20	LO *Gr. margaritae*	15H-5, 131–133	16H-2, 71–73	139.71	144.11	16.05	16.20	3.70
21	LO *R. pseudoumbilica*	15H-5, 130	16H-6, 80	139.70	150.20	16.04	16.54	3.77
22	LO *A. delicatus*	17X-4, 21	18X-2, 133.5	154.58	157.24	16.67	16.71	4.39
23	LO *Gg. nepenthes*	16H-2, 71–73	19X-2, 113–115	144.11	162.93	16.20	16.90	4.63
24	FO *Gr. puncticulata*	19X-2, 113–115	21X-5, 109–111	162.93	185.59	16.90	18.27	4.69
25	FO *Gr. crassaformis*	16H-2, 71–73	19X-2, 113–115	144.11	162.93	16.20	16.90	4.78
26	FO *D. asymmetricus*	18X-2, 133.5	18X-CC, 49	157.24	158.36	16.71	16.75	4.79
27	FO *C. acutus*	20X-CC, 33	21X-CC, 22	179.63	188.23	17.63	18.29	5.34
28	LO *Gr. juanai*	25X-4, 148–150	26X-4, 89–91	223.18	232.19	20.29	20.92	5.40
29	LO *D. quinqueramus*	23X-6, 10	24X-7, 8	205.40	216.58	19.22	19.82	5.56
30	LO *A. amplificus*	23X-6, 10	24X-7, 8	205.40	216.58	19.22	19.82	5.88
31	FO *A. amplificus*	24X-7, 8	25X-6, 97	216.58	225.67	19.82	20.31	6.50
32	FO *Gr. juanai*	31X-3, 111–113	32X-6, 26–27	279.21	292.56	24.29	20.92	8.00
33	FO *D. berggreni*	26X-6, 64.5	27X-4, 70	234.95	241.70	21.27	22.12	8.40
34	LO *D. hamatus*	27X-4, 70	27X-6, 47	241.70	244.47	21.27	22.12	9.40
35	FO *D. hamatus*	28X-3, 36	29X-7, 14	249.46	264.84	22.92	23.91	10.40
36	FO *Gg. nepenthes*	30X-1, 31–33	31X-3, 111–113	265.71	279.21	23.86	24.29	10.80
37	LO *C. floridanus*	28X-3, 36	29X-7, 14	249.46	264.84	22.92	23.91	13.20
38	FO *S. heteromorphus*	34X-2, 50.5	—	306.11	—	25.63	—	18.10
39	LO *D. bisecta*	40X-4, 17	—	366.67	—	33.08	—	23.80
40	FO *S. ciperoensis*	37X-6, 120	—	341.70	—	50.56	—	28.10
41	FO *C. oamaruensis*	39X-6, 145	—	361.25	—	54.87	—	36.90
42	FO *R. umbilica*	40X-CC, 5	—	367.79	—	54.87	—	42.20

Notes: Numbers in left column match numbers on Figures 54–57. The pelagic depths refer to the depth of datum levels in the stacked pelagic sequence.

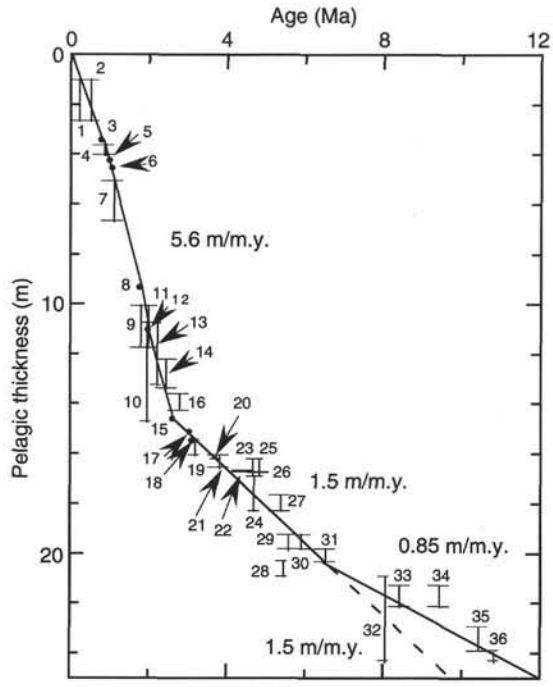

Figure 54. Sediment accumulation rates for the upper part of the pelagic sequence of Hole 950A. Vertical bars represent distance between sample points; filled circles represent paleomagnetic ages. Numbers refer to datum levels given in Table 11. The dashed line represents extrapolation of the curve between 15 and 20 m with a gradient of 1.5 m/m.y.

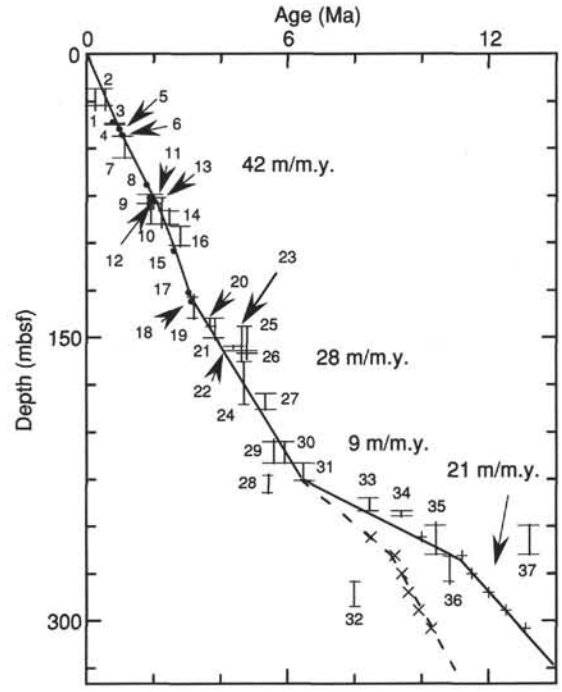

Figure 56. Sediment accumulation rates for the upper part of the total sediment sequence of Hole 950A. Vertical bars represent the distance between sample points. Numbers refer to datum levels given in Table 11. The dashed line represents data derived from the dashed line in Figure 55. Vertical bars represent distance between sample points; filled circle = paleomagnetic age, + = pelagic ages, and × = alternative pelagic ages.

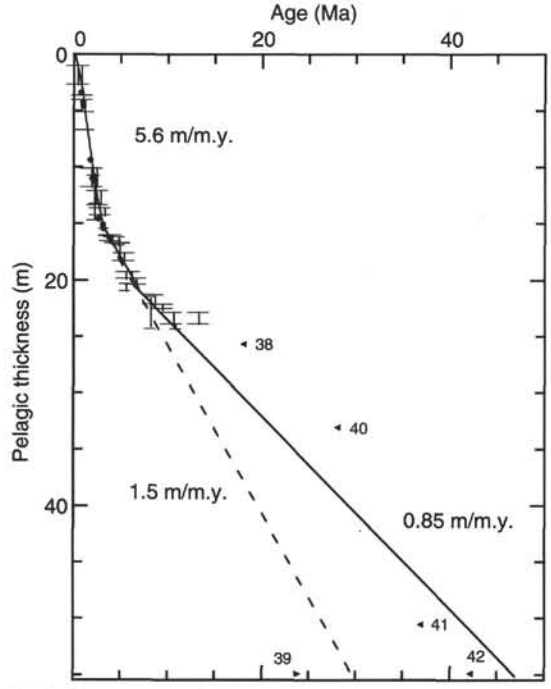

Figure 55. Sediment accumulation rates for the total pelagic sequence of Hole 950A. Vertical bars represent distance between sample points; filled circles represent paleomagnetic ages. Right-pointing symbol = nannofossil minimum age, left-pointing symbol = nannofossil maximum age. The dashed line represents extrapolation of the curve between 15 and 20 m with a gradient of 1.5 m/m.y.

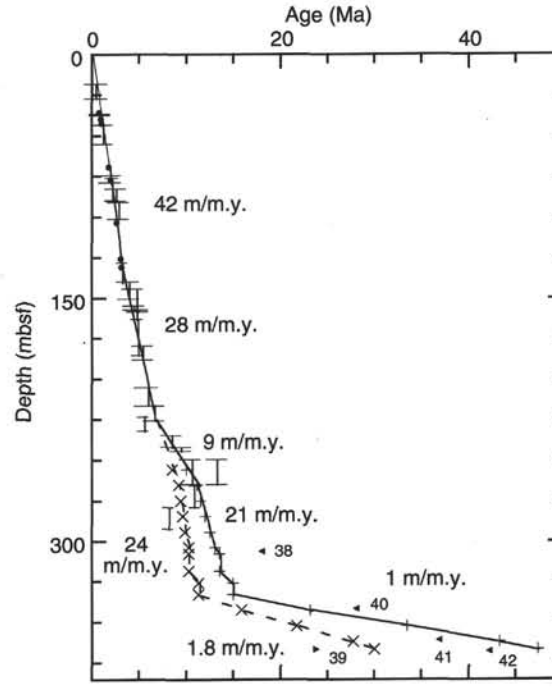

Figure 57. Sediment accumulation rates for the total sediment sequence of Hole 950A. Vertical bars represent distance between sample points. The dashed line represents data derived from the dashed line in Figure 55. Vertical bars represent distance between sample points. Filled circle = paleomagnetic age, + = pelagic ages, × = alternative pelagic ages, right-pointing symbol = minimum age, and left-pointing symbol = maximum age.

SHORE-BASED LOG PROCESSING

HOLE 950A

Bottom felt: 5448.6 mbrf (used for depth shift to seafloor)
Total penetration: 381.3 mbsf
Total core recovered: 339.14 m (88%)

Logging Runs

Logging string 1: DIT/LSS/NGT
Logging string 2: HLDT/CNTG/NGT
Logging string 3: ACT/GST/NGT
Logging string 4: FMS/GPIT/NGT (three passes)

Wireline heave compensator was used to counter ship heave resulting from the mild sea conditions (0.3–1.5 m).

Bottom-hole Assembly

The following bottom-hole assembly depths are as they appear on the logs after differential depth shift (see "Depth shift" section) and depth shift to the seafloor. As such, there might be a discrepancy with the original depths given by the drillers on board. Possible reasons for depth discrepancies are ship heave, use of wireline heave compensator, and drill string and/or wireline stretch.

DIT/LSS/NGT: Bottom-hole assembly at ~69 mbsf.
HLDT/CNTG/NGT: Bottom-hole assembly at ~72 mbsf.
ACT/GST/NGT: Bottom-hole assembly at~68 mbsf.
FMS/GPIT/NGT: Bottom-hole assembly at ~73.4 mbsf.

Processing

Depth shift: All original logs have been interactively depth shifted with reference to NGT from DIT/LSS/NGT main run, and to the seafloor (–5448.6 m). A list of the amount of differential depth shifts applied at this hole is available upon request.

Gamma-ray processing: NGT data have been processed to correct for borehole size and type of drilling fluid.

Acoustic data processing: The four transit time measurements have been edited to eliminate some of the noise and cycle skipping experienced during the recording. Then they have been averaged before calculating compressional velocity.

Geochemical processing: (For detailed explanation of the processing please refer to the "Explanatory Notes" chapter [this volume] or to the geochem.doc file on the enclosed CD-ROM). The elemental yields recorded by the GST tool represent the relative contribution of only some of the rock-forming elements (iron, calcium, chlorine, silica, sulfur, hydrogen, gadolinium, and titanium—the last two computed during geochemical processing) to the total spectrum. Because other rock-forming elements are present in the formation (such as aluminum, potassium, etc.), caution is recommended in using the yields to infer lithologic changes. Instead, ratios (see acronyms.doc on CD-ROM) are more appropriate to determine changes in the macroscopic properties of the formation. A list of oxide factors used in geochemical processing includes the following:

$SiO_2 = 2.139$
$CaCO_3 = 2.497$
$FeO^* = 1.358$
$TiO_2 = 1.668$
$K_2O = 1.205$
$Al_2O_3 = 1.889$

FeO^* = computed using an oxide factor that assumes a 50:50 combination of Fe_2O_3 and FeO factors.

Quality Control

During the processing, quality control of the data is mainly performed by cross-correlation of all logging data. Large (>12 in.) and/or irregular borehole affects most recordings, particularly those that require eccentralization (CNTG, HLDT) and a good contact with the borehole wall.

Hole diameter was recorded by the three-arm mechanical caliper, the hydraulic caliper on the HLDT tool (CALI), and the caliper on the FMS string (C1 and C2).

Data recorded through bottom-hole assembly, such as the gamma ray recorded above 69 mbsf, should be used qualitatively only because of the attenuation on the incoming signal.

FACT = quality control curve in geochemical processing. Accuracy of the estimates is inversely proportional to the magnitude of the curve.

Note: Details of standard shore-based processing procedures are found in the "Explanatory Notes" chapter, this volume. For further information about the logs, please contact:

Cristina Broglia
Phone: 914-365-8343
Fax: 914-365-3182
E-mail: chris@ldeo.columbia.edu

Elizabeth Pratson
Phone: 914-365-8313
Fax: 914-365-3182
E-mail: beth@ldeo.columbia.edu

Hole 950A: Natural Gamma Ray-Resistivity-Sonic Logging Data

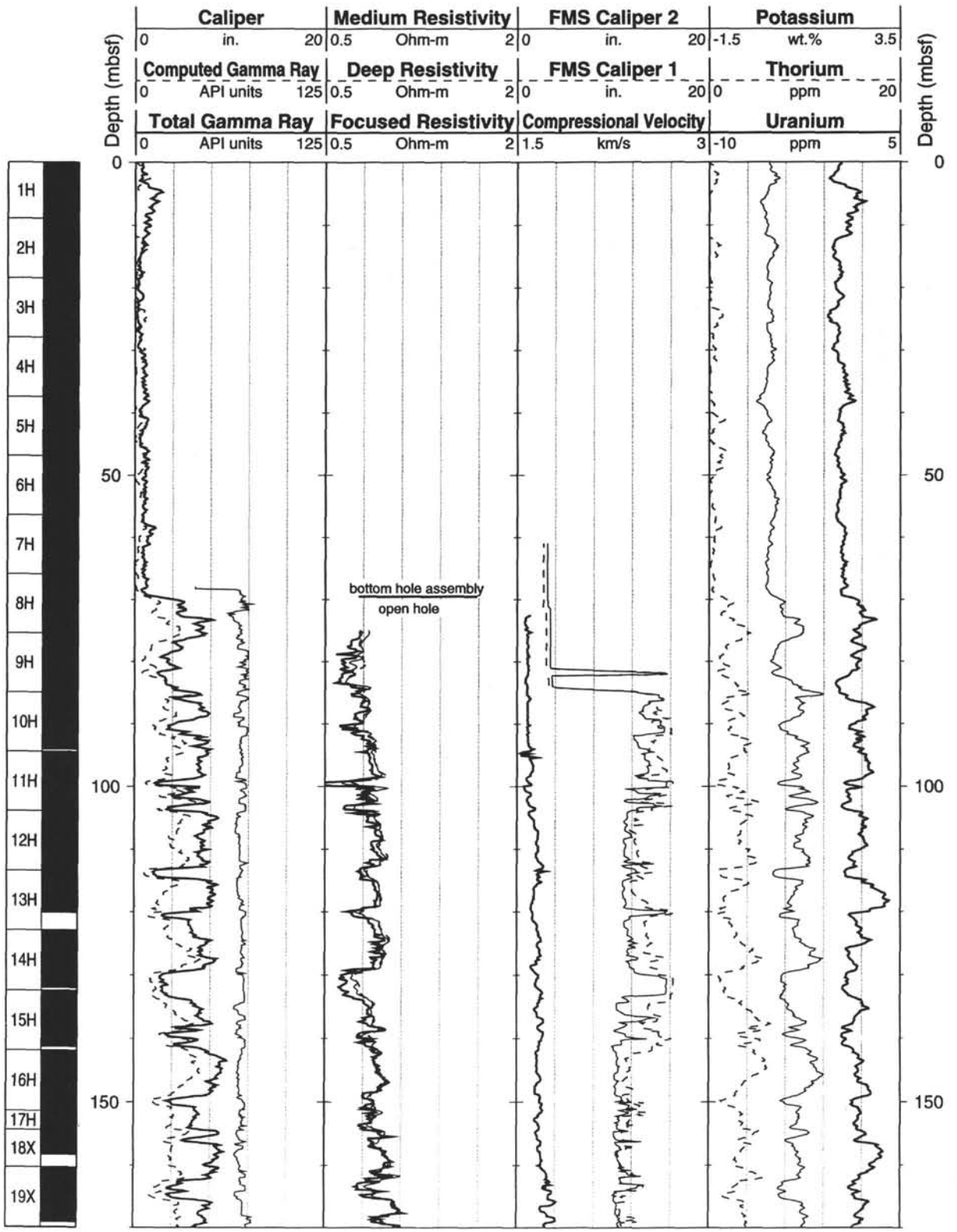

Hole 950A: Natural Gamma Ray-Resistivity-Sonic Logging Data (cont.)

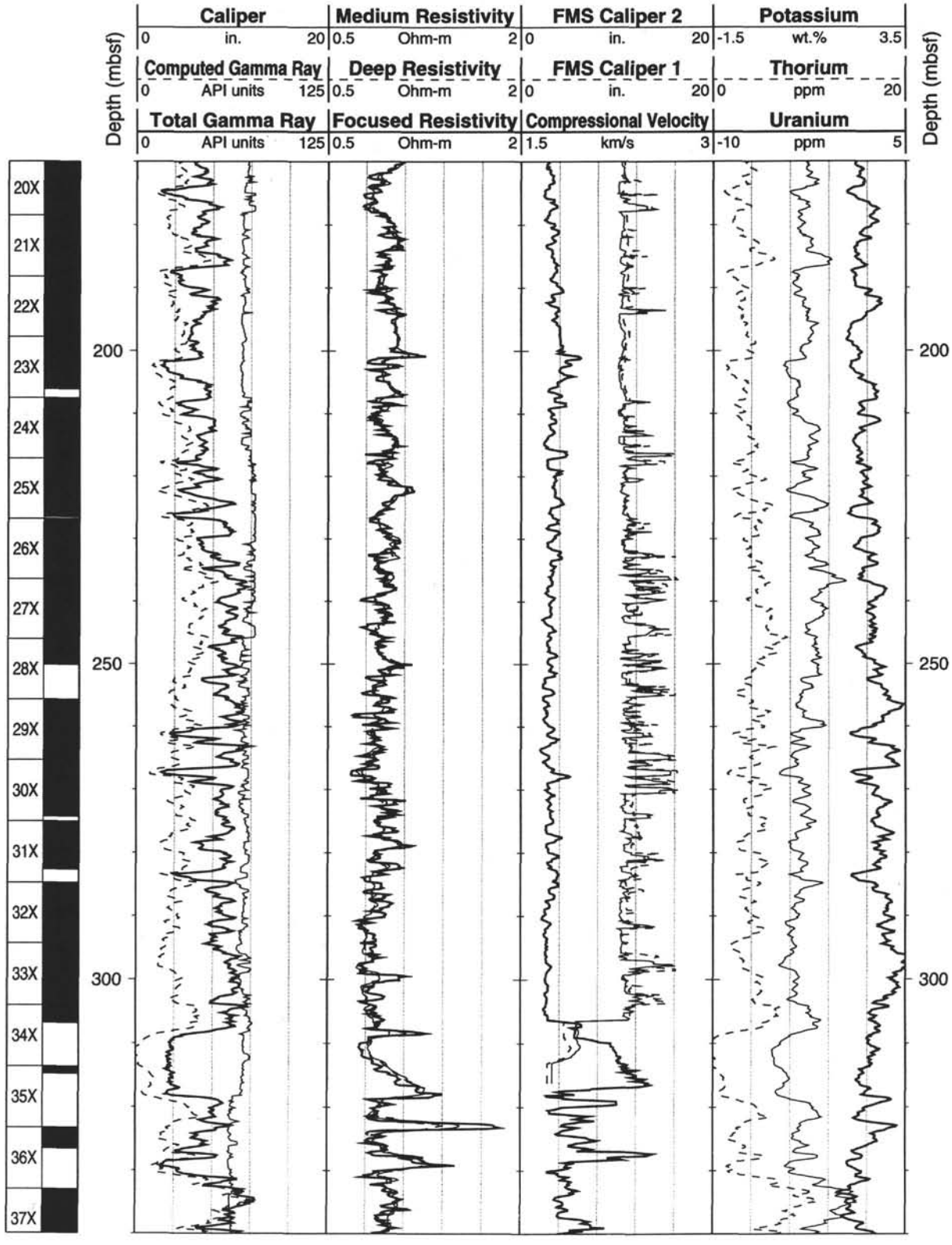

Hole 950A: Natural Gamma Ray-Resistivity-Sonic Logging Data (cont.)

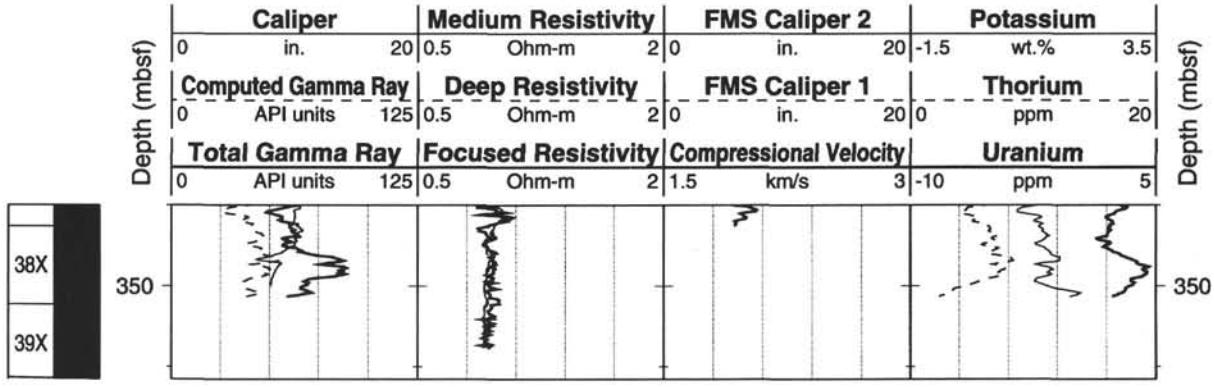

Hole 950A: Natural Gamma Ray-Density-Porosity Logging Data

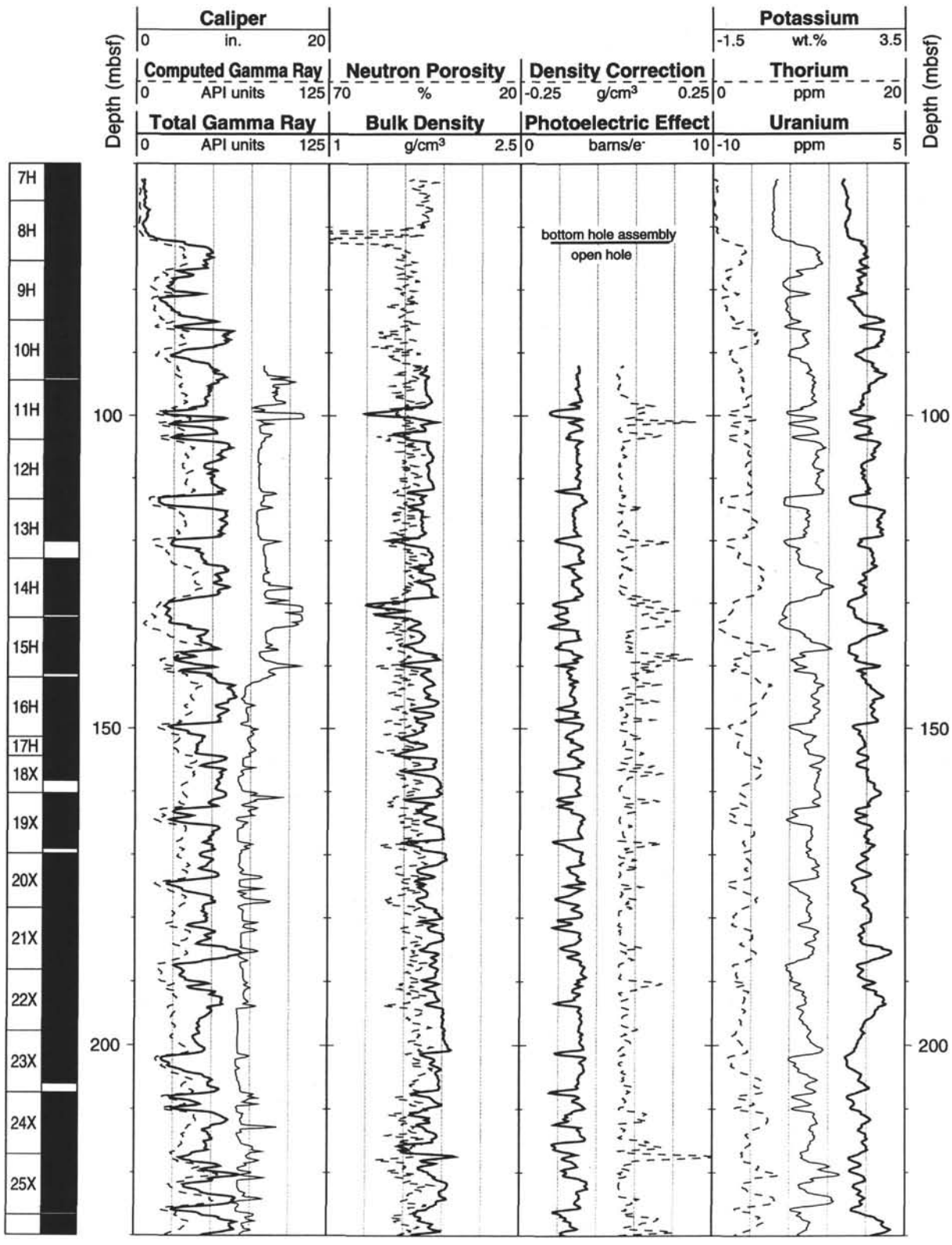

Hole 950A: Natural Gamma Ray-Density-Porosity Logging Data (cont.)

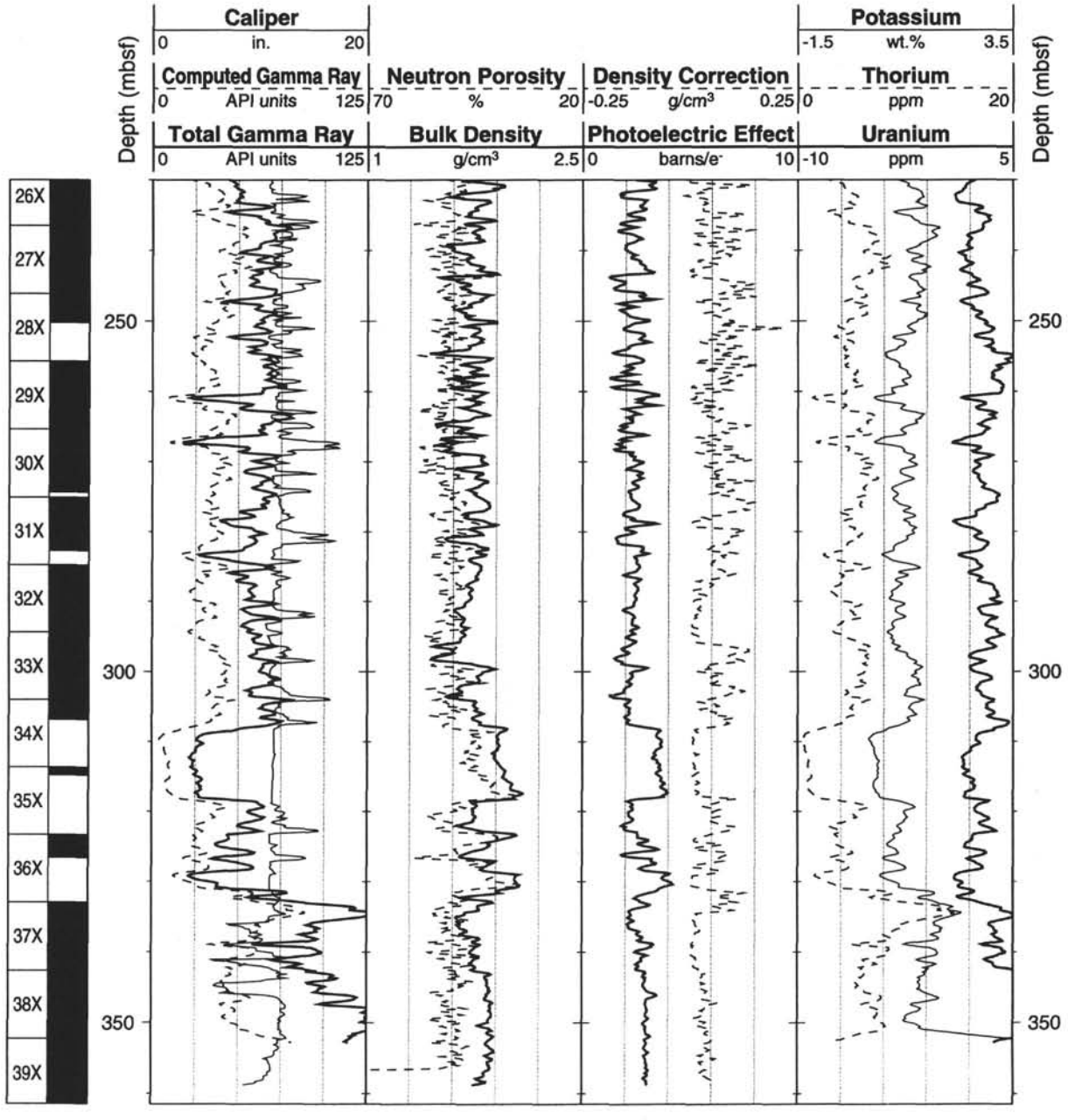

Hole 950A: Natural Gamma Ray Logging Data

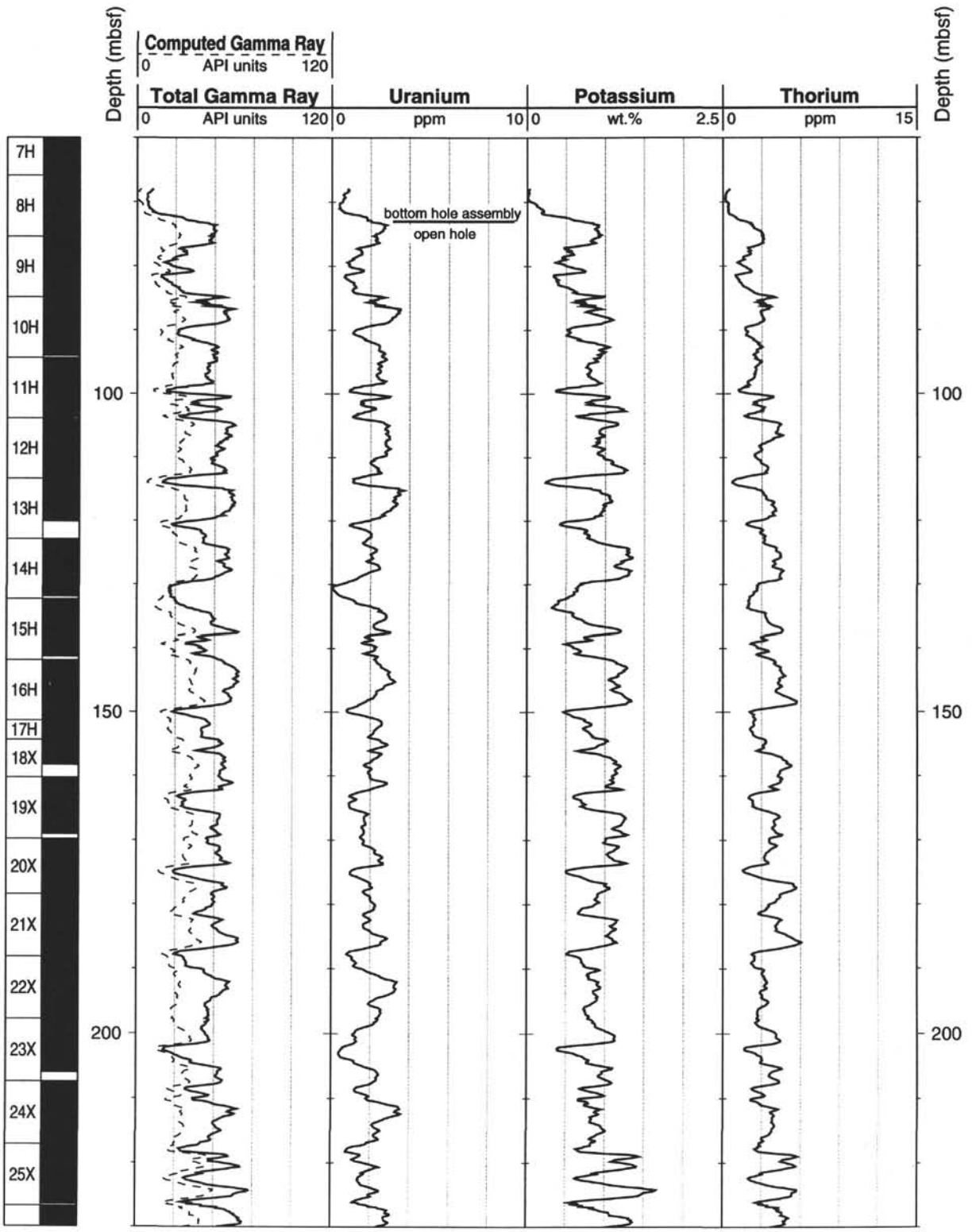

Hole 950A: Natural Gamma Ray Logging Data (cont.)

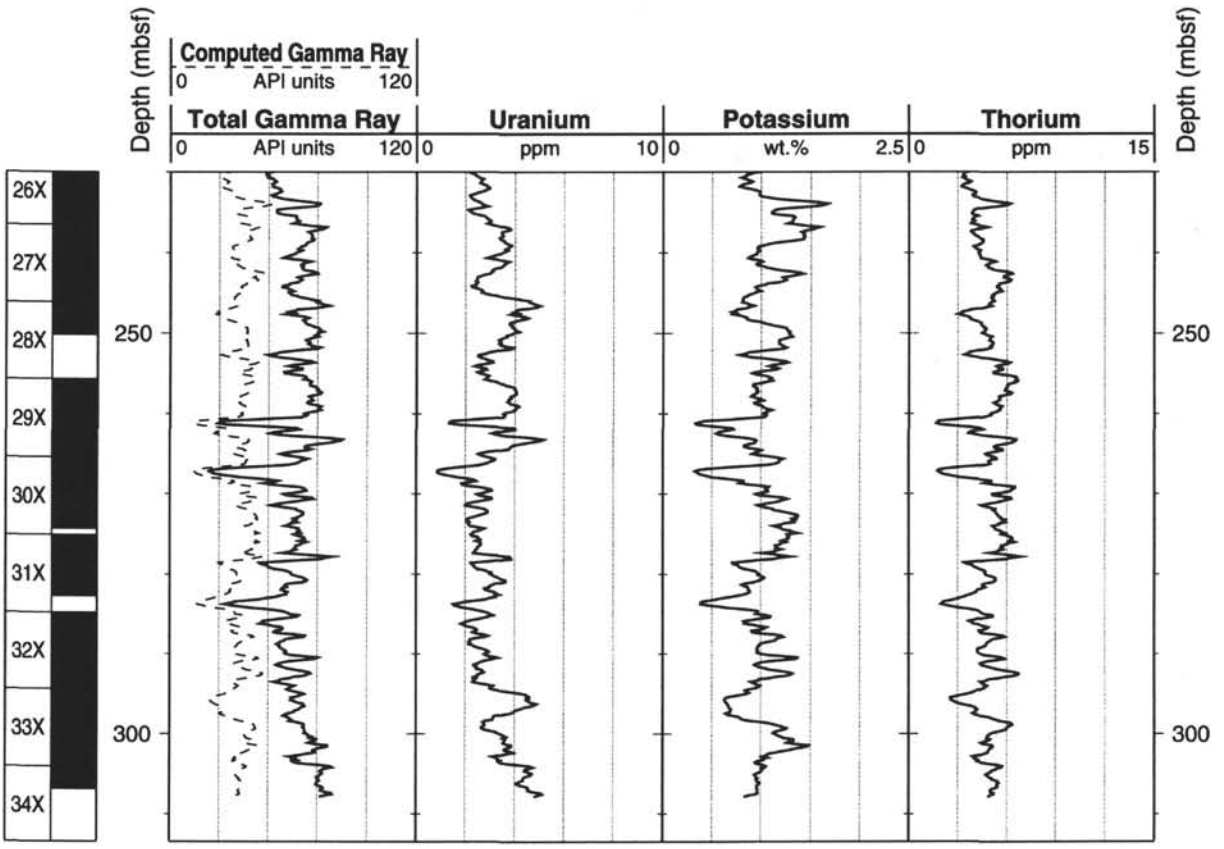

950A: Geochemical Logging Data

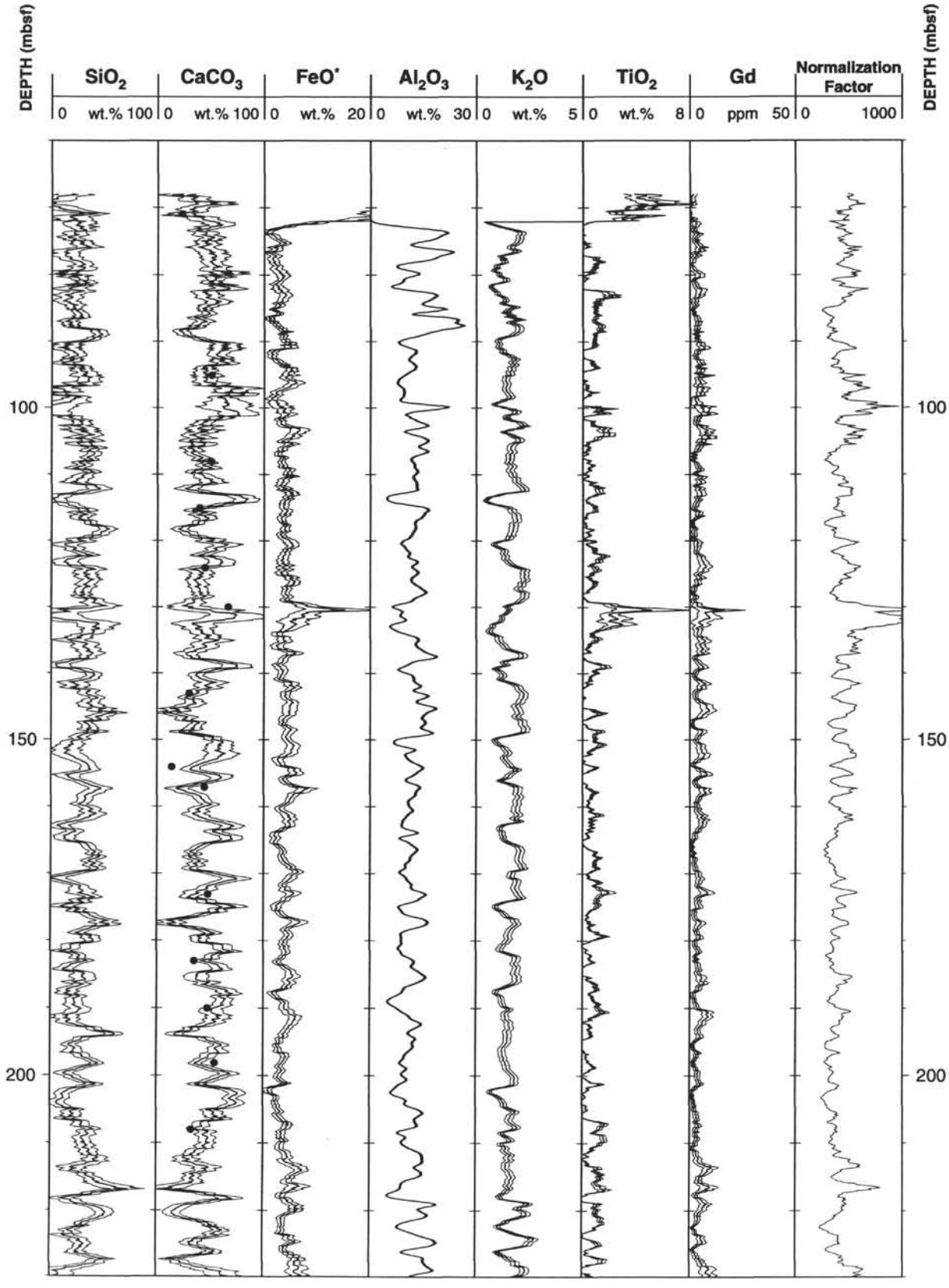

950A: Geochemical Logging Data (cont.)